

UNIVERSITY OF NOVA GORICA
GRADUATE SCHOOL

**MODELLING SPELEOGENESIS IN
TRANSITION FROM PRESSURISED TO
FREE SURFACE FLOW**

DISSERTATION

Matija Perne

Mentors: prof. dr. Franci Gabrovšek
prof. dr. Georg Kaufmann

Nova Gorica, 2012

Zahvala

Hvala vsem, ki ste me podpirali in mi pomagali na poti proti doktoratu, še posebej članom komisije in mentorjema. Hvala mentorju pri usposabljanju za mladega raziskovalca, Franciju Gabrovšku, za vso pomoč in usmerjanje.

Acknowledgements

Many thanks to everyone who assisted me in finishing my PhD programme, especially to the commission members and both mentors. Special thanks go to my mentor and boss when I was working as a young researcher, dr. Franci Gabrovšek, for all the help and advice.

Povzetek

Modeliranje speleogeneze na prehodu iz toka pod tlakom v tok s prosto gladino

V raziskavi smo se osredotočili na razvoj kraških kanalov in mrež kanalov v kasnejših stopnjah, ko je tok vode v njih turbulenten in ima prosto gladino. Do zdaj je z numeričnim modeliranjem niso preučevali, saj je za modeliranje zahtevnejša od zgodnejših stopenj, ko so kraški kanali še povsem zaliti. Da bi podrobneje preučili konceptualne modele te stopnje speleogeneze, smo razvili računske pristope, v okviru katerih lahko opišemo tudi tok s prosto gladino.

Za izračun vodnega toka in delno za izračun adveksijskega transporta smo uporabili odprtokodni programski paket EPA-SWMM. Sklopili smo ga z našimi programi, ki so izračunali hitrosti topljenja in spremembe v presekih kanalov zaradi topljenja. Pri izračunu topljenja smo upoštevali tako kinetiko reakcije na površini kamnine kakor omejeno hitrost transporta topljenca s površine. Modelirali smo razvoj prečnih profilov posameznih kanalov in razvoj mrež okroglih kanalov kot modelov vodonosnikov. Da smo raziskali možne učinke spremenljivega pretoka, smo razvoj preučevanih objektov računali tako ob nespremenljivem dotoku kakor upošteva prehodne pojave ob spremembah dotoka.

Modelirani razvoj prečnih profilov posameznih kanalov se ujema z našimi pričakovanji in s primeri rovov, ki jih poznamo iz narave. Razvoj dvodimenzionalnih mrež kanalov smo uporabili za razlago položnih za vodo prepustnih plasti in za opis navpičnih prereзов vodonosnikov. Večina rezultatov spominja na rezultate predhodnih modelov, ki proste gladine niso obravnavali. Opazili smo nekaj novih mehanizmov, ki odločijo o tem, kateri izmed kanalov rastejo naprej, ko se rast ostalih ustavi. Na navpičnih mrežah smo razvoj vadoznih kanalov in vpliv sprememb v hidravličnem potencialu na speleogenezo obravnavali natančneje, kakor so to zmogli predhodni modeli.

Na osnovi dobljenih rezultatov zaključujemo, da je speleogenezo ob pogojih toka s prosto gladino in ob spremenljivem dotoku s prehodnimi pojavi pri trenu-

tnem stanju tehnike možno modelirati. Modeli ne napovedujejo izrazitega vpliva prehodnih pojavov na speleogenezo. Rezultati modeliranja mrež kraških kanalov večinoma potrjujejo rezultate prejšnjih modelov, ki toka s prosto gladino niso pravilno upoštevali. Podrobno napovedovanje prečnih profilov je novost, saj brez modeliranja proste gladine in njene lege ne bi bilo mogoče. Mnogi izmed rezultatov kažejo na to, da so za speleogenezo pomembni sedimenti, ki jih naši modeli ne obravnavajo.

Ključne besede: kraški vodonosnik, speleogeneza, prosta gladina, numerično modeliranje

Summary

Modelling speleogenesis in transition from pressurised to free surface flow

The focus of this study is the genesis of individual karst conduits and conduit networks during the later stages of their evolution when turbulent flow is fully developed and conduits switch from pressurised to free-surface flow. This stage of cave formation had not been modelled numerically in large part because it is more demanding to simulate than earlier stages when flow is still pressurised. In order to investigate conceptual models of this stage of speleogenesis more advanced numerical techniques were developed.

To calculate water flow and solute transport, an available open-source program named EPA-SWMM was used. It was coupled to our own code which calculated dissolution rates and corresponding geometrical changes of the karst conduits. Both surface reaction and diffusion transport of solute away from the conduit wall were taken into account. The model was applied to calculate both the evolution of the cross section of single conduits and the evolution of conduit networks. To explore the potential effects of variable flow conditions, which have not been considered in previous numerical models of speleogenesis, simulations were run with constant recharge as well as with transient recharge.

The cross-sections of single conduits predicted by the model fit our expectations and the examples known from nature. Simulations of the evolution of two-dimensional networks of conduits were used to represent both low dip aquifers and vertical cross-sections through aquifers. Many of the results were similar to the predictions of earlier models that do not account for free surface flow. However, new mechanisms that determine the subset of conduits that is enlarged the most were found. In vertical networks, evolution of drawdown vadose passages and the influence of changes in hydraulic head on speleogenesis were also investigated more accurately than in earlier models.

It was concluded that the state of the art facilitates modelling of speleogenesis

under free surface flow conditions and transient recharge. No strong influence of transients was observed, and the modelling of conduit networks mostly confirmed results of earlier models neglecting free surface flow. The modelling framework developed here allows much more detailed exploration of the evolution of conduit shapes than with previous models, since the level of the free surface is tracked and full conduit cross-sections are evolved. Many results suggest that sediments, which were not included in our models, also have an important influence on speleogenesis.

Keywords: karst aquifer, speleogenesis, free-surface flow, numerical modeling

Contents

1	Introduction	10
2	Groundwater flow in karst aquifer	13
2.1	Equations	13
2.1.1	Fluid flow in porous medium	14
2.1.2	Laminar flow through a fissure	14
2.1.3	Turbulent flow through a conduit	15
2.2	Exchange between conduits and porous media	16
2.3	Modelling of flow	17
3	Dissolution kinetics in karst aquifers	22
3.1	Dissolution rate law in turbulent flow	22
3.2	Rate coefficients	24
3.3	Evaporites	25
3.4	Carbonates	26
4	Evolution of single conduits	28
4.1	One conduit under constant recharge	28
4.1.1	Numerical example	28
4.2	Conduits under transient recharge and in basic systems	39
4.2.1	Comparison to a single conduit and constant recharge	39
4.2.2	Numerical example	41
5	Evolution of conduit networks	47
5.1	Numerical example	47
5.1.1	Flow	47
5.1.2	Dissolution	48
5.1.3	Advection	49
5.2	Results	50
5.2.1	Graphical representation	50

5.2.2	Network on a low dip plane	50
5.2.3	Networks as vertical cross-sections through aquifers	62
5.2.4	Discussion	68
6	Discussion of the results	71
A	Calculating transport of water from a conduit to the porous matrix by boundary distributed source method	78

List of Symbols

A	Cross-sectional area [m ²]
C	Roughness coefficient [1]
D	Diffusion coefficient [m ² /s]
D_h	Hydraulic diameter [m]
H	Hydraulic head [m]
ΔH	Loss of hydraulic head [m]
L	Fissure length [m]
M	Empirical correction term [1]
N_{Re}	Reynolds number [1]
P	Wetted perimeter [m]
Q	Flow rate [m ³ /s]
R	Hydraulic radius [m]
R_{HP}	Flow resistance [s/m ²]
Sc	Schmidt number [1]
S_f	Friction slope [1]
V	Flow velocity [m/s]
a	Fissure aperture width [m]
b	Fissure width [m]
c	Volume concentration [1]
c_b	Bulk concentration [1]
c_{b0}	Initial bulk concentration [1]
c_{eq}	Equilibrium concentration [1]
c_s	Surface concentration [1]
f	Friction factor [1]
g	Acceleration of gravity [m/s ²]
h	Viscous sublayer thickness [m]
h_L	Local energy loss per unit length [1]

n	Manning roughness coefficient [1]
p	Pressure [Pa]
\mathbf{q}	Flux [m/s]
t	Time [s]
u_τ	Friction velocity [m/s]
v	Dissolution rate [m/s]
v_D	Transport limited dissolution rate [m/s]
v_s	Surface limited dissolution rate [m/s]
\mathbf{w}	Velocity [m/s]
x, y, z	Space coordinate [m]
α	Dissolution rate coefficient [m/s]
α_D	Transport limited dissolution rate coefficient [m/s]
α_s	Surface limited dissolution rate coefficient [m/s]
ϵ	Diffusion boundary layer thickness [m]
μ	Dynamic viscosity [Pa · s]
ν	Kinematic viscosity [m ² /s]
ρ	Density [kg/m ³]
τ_ω	Shear stress [Pa]
φ	Slope angle [1]
∇	$(\frac{\partial}{\partial x}, \frac{\partial}{\partial y}, \frac{\partial}{\partial z})$ [m ⁻¹]

List of parameter values

D	$1.5 \cdot 10^{-9}$ m ² /s for salt, $1 \cdot 10^{-9}$ m ² /s for limestone
c_{eq}	0.166 for salt, 0.0001108 for limestone
g	9.8 m/s ²
n	0.01 or 0.015
α_s	not used (∞) or 1 m/s for salt, $2 \cdot 10^{-7}$ m/s for limestone
μ	10^{-3} Pa · s
ρ	10^3 kg/m ³

Chapter 1

Introduction

Karst is an area where the surface morphology is controlled by the dissolution of rock [12]. Dissolution of rock by groundwater also affects the characteristics and development of the underlying aquifer [13]. The initial discontinuities, such as fractures, faults and bedding planes, are enlarged by dissolution and the local hydraulic conductivities are increased, which can result in larger flow densities and higher dissolution rates [28]. As a result, karst aquifers are characterised by a network of solution conduits, which often drain 99 % or more of the groundwater flow [38]. This makes karst aquifers highly heterogeneous and anisotropic [13]. In general, the locations of the conduits are often difficult to determine, and water can flow in surprising ways. Therefore, suitable characterisation of aquifer properties is important for its efficient protection and management.

Understanding a karst aquifer is in our opinion strongly linked to the comprehension of its development. In practice it is not possible to know the exact locations of all the voids in a given moment. From the field data that are available we can infer more information if we include the time dimension and the processes responsible for development of the voids.

The ideas on karst aquifers and their formation are formalised as conceptual models. A contemporary example is the Four State Model, which postulates that the state of the aquifer is determined by density, penetrability and linkage of fractures and bedding planes, and orientation of hydraulic gradients [13]. The validity of conceptual models is challenged by field observations and process-based numerical models, which have in the last 20 years shown to be an extremely valuable tool for the purpose. Numerical models are based on rate laws and conservation equations [15]. They couple water flow, transport of dissolved species and dissolution of the rock.

Numerical modelling of the development of karst aquifers begins with one-

dimensional models of evolution of a single fracture by Dreybrodt and Palmer [8, 32, 6]. The evolution of a fracture is investigated more thoroughly with advanced models by Hanna [19]. The 1D models are sufficient to investigate the dissolution length scales. The importance of non-linearities in dissolution rate laws and feedback loops can also be investigated through them [10]. At the same time, these models are the basic elements of more complex ones [10].

Evolution of two-dimensional fracture networks is researched by several authors. Models increase in complexity of their structure and boundary conditions starting from works by Groves and Howard [18]. Siemers [37] deals with more complex 2D networks, while Kaufmann & Braun [24, 23] and Liedl [30] introduced so-called double porosity models, where flows through rock matrix and through discrete conduits are coupled. Apart from the processes inherited from single fracture models, 2D models enable one to investigate competition of different conduits and the influence of mixing corrosion [10].

Numerical models of unconfined aquifers, with falling water table, were also developed, of a fracture network by Gabrovšek and Dreybrodt [17] and of double porosity by Kaufmann [22]. The models of unconfined aquifers offer insight into different conceptual models and have also been used to describe regional case examples [26].

Annable and Sudicky [1] and Kaufmann, Romanov and Hiller [27] also developed three-dimensional double porosity models. Both 2D and 3D models have been used to investigate intensified karstification around dam sites [10].

All existing models except for Annable and Sudicky [1] only simulate speleogenesis, formation of karst conduits, under full pipe flow conditions. Later phases of speleogenesis comprising of phreatic-vadose transition and vadose development of conduits in turbulent flow conditions have mostly not been considered. However, a major part of dry accessible caves are former conduits that did experience phreatic vadose transition which could influence their geometries.

Therefore it is a matter of utmost importance in speleogenetic modelling to develop models describing speleogenesis in epiphreatic and vadose settings. The appropriate model needs to account for:

- free water surface and pressurised turbulent flow in individual conduits and conduit networks in arbitrary geometry;
- transient recharge conditions;
- dissolution of rock walls and transport of dissolved species;
- temporal development of conduit geometry.

A model meeting these criteria can be applied to:

- study the profile evolution in single conduits;
- study the conduit network evolution in various settings;
- determine the importance of later stages of speleogenesis on the distribution of conduits in various settings;

We start building up a numerical model on the assumption that dissolution and transport do not significantly influence the flow which can thus be calculated separately. The model is assembled from separate parts; a flow module and a module including dissolution, geometry development and transport. The latter is disassembled further into two parts. One includes the processes happening at the rock surface or near it – dissolution and short-range transport of the dissolved species by diffusion, and it also introduces changes in geometry as a result of dissolution. The other is advection, transport of the dissolved species with the bulk of the flow. The flow part only informs the other two and does not depend on any information from them. Dissolution and advection have to interact with each other only through the bulk concentrations and dissolution rates.

In this thesis, we concentrate on two main topics: evolution of single conduits and evolution of conduit networks. In both topics, the numerical models follow the same strategy. In each cycle of the calculation:

1. the water flow is calculated using SWMM;
2. the dissolution rates are calculated;
3. the new geometry after one timestep of dissolution is calculated;
4. the solute concentrations resulting from the dissolution and the advection by the water flow are calculated;
5. the procedure returns to the step 1 and continues from the new geometry and concentration field

(cf. Fig. 4.2).

Chapter 2

Groundwater flow in karst aquifer

The general equations of fluid flow are valid for the whole karst aquifer but solving them would be highly demanding. Through some approximations, they can be transformed into simplified versions that are more convenient to use. The features of karst aquifers are diverse and support different types of flow, so different features are described by different approximations and equations. Both the general and the more specific equations are introduced in Sec. 2.1.

Water can flow from karst conduits into the pores of the rock or vice versa. In Sec. 2.2, the importance of the exchange of water between conduits and rock matrix for evolution of the conduits is investigated. It turns out that such exchange can be neglected from a certain stage in conduit development on.

To get insight into evolution of conduits, solutions of the equations of flow are needed. Sec. 2.3 deals with the method used to solve these equations in conduits.

2.1 Equations

Fluid flow is in general described by continuity and Navier-Stokes equations [2],

$$\frac{\partial \rho}{\partial t} + \nabla \cdot (\rho \mathbf{w}) = 0 \quad (2.1)$$

and

$$\rho \frac{D\mathbf{w}}{Dt} = \mu \nabla^2 \mathbf{w} - \nabla p + \rho \mathbf{g}, \quad (2.2)$$

valid also in karst aquifers. Here, ρ stands for fluid density, t is time, \mathbf{w} is velocity, μ is dynamic viscosity, p is pressure, \mathbf{g} is acceleration of gravity and operator ∇ stands for $(\frac{\partial}{\partial x}, \frac{\partial}{\partial y}, \frac{\partial}{\partial z})$.

The defining feature of karst aquifers is the solubility of the medium in water. The water that is flowing through the voids in the medium (interstitial pores,

fissures, cave passages, etc.) is enlarging them by dissolution and thus increasing the local hydraulic conductivity. Typically the enlarged conductivities result in larger flow densities and in higher dissolution rates. The heterogeneity of the aquifer with respect to water flow regimes increases due to this positive feedback loop [28]. Because of the strong heterogeneity of the aquifer and an unknown exact shape of the voids in the medium, exact solutions of the governing equations are impossible to obtain. However, in different parts of the aquifer, different approximations and simplifications are valid.

2.1.1 Fluid flow in porous medium

Laminar flow through a porous medium is described by Darcy's law. In the case of homogeneous isotropic medium it is [3]

$$\mathbf{q} = -K\nabla\phi, \quad (2.3)$$

where \mathbf{q} is flux, K is hydraulic conductivity and ϕ the hydraulic head. In anisotropic media, the hydraulic conductivity is a tensor quantity.

2.1.2 Laminar flow through a fissure

Laminar flow through a conduit is described by Hagen-Poiseuille equation. In aquifers, typical conduits transmitting flow in laminar fashion are fissures, their cross-sections are long in one and narrow in the other dimension. The form of the equation for such fissures is [11]

$$\begin{aligned} Q &= \frac{\Delta H}{R_{\text{HP}}} \\ R_{\text{HP}} &= \frac{12\mu}{\rho g} \int_0^L \frac{dx}{a^3(x) b(x) M(x)} \\ M &= 1 - 0,6\frac{a}{b}, \end{aligned} \quad (2.4)$$

where Q is the flow rate, ΔH is the loss of hydraulic head, L the fissure length, a the fissure aperture width, b the fissure width and g acceleration of gravity. R_{HP} is the flow resistance and M stands for an empirical correction term for the geometry.

2.1.3 Turbulent flow through a conduit

Pressurised conduit

For turbulent flow in a conduit, several empirical relations relating friction loss to flow velocity, hydraulic diameter and a friction coefficient are available. One of them is the Darcy-Weisbach formula [7],

$$S_f = \frac{fV^2}{2D_h g}, \quad (2.5)$$

where S_f is friction slope (head loss per unit length), V is flow velocity (equal to the flow rate Q divided by the cross-sectional area A), D_h is hydraulic diameter of the conduit and f is friction factor. For smooth circular pipes an approximate relation for f is Colebrook equation [7]

$$\frac{1}{\sqrt{f}} = 2 \log \left(N_{\text{Re}} \sqrt{f} \right) - 0.8. \quad (2.6)$$

Reynolds number N_{Re} is defined as

$$N_{\text{Re}} = \frac{\rho V D_h}{\mu} \quad (2.7)$$

and is a measure of the ratio of inertial forces to viscous forces.

Apart from the Darcy-Weisbach formula, one can use the Hazen-Williams formula [35],

$$V = C S_f^{0.54} R^{0.63}, \quad (2.8)$$

where C is roughness coefficient and R is hydraulic radius.

The Manning equation [14] reads

$$S_f = \frac{n^2 V^2}{R^{4/3}}, \quad (2.9)$$

where n is Manning roughness coefficient, is typically used for partially filled conduits, while it can also be used for pressurised conduits.

Qualitatively all three formulae are quite similar:

- according to Manning equation, $V \propto S_f^{1/2} R^{2/3}$ [14];
- according to Hazen-Williams formula, $V \propto S_f^{0.54} R^{0.63}$ [35];
- according to Darcy-Weisbach formula, $V \propto S_f^{1/2} R^{1/2} f^{-1/2}$, where f has a logarithmic dependence on S_f and R [7].

Free-surface flow in a conduit

The complete one-dimensional equations of open-channel flow are called Saint Venant equations [5]. They are obtained by integrating Navier-Stokes equation in the other two dimensions. Their form is [34]

$$\frac{\partial A}{\partial t} + \frac{\partial Q}{\partial x} = 0 \quad (2.10)$$

$$\frac{\partial Q}{\partial t} + \frac{\partial Q^2/A}{\partial x} + gA \frac{\partial H}{\partial x} + gAS_f + gAh_L = 0. \quad (2.11)$$

Here, x is distance along the conduit, t is time, A is cross-sectional area, Q is flow rate, H is the hydraulic head of water in the conduit (elevation head plus any possible pressure head) and h_L is the local energy loss per unit length of conduit. Both equations assume that there are no lateral inflows and that water is incompressible. Eq. 2.10 is the continuity equation. Eq. 2.11 is the momentum equation for x dimension, which means that water velocity in directions other than x is not taken into account. Water pressure is assumed to be hydrostatic so that H depends only on x [5]. For a known cross-sectional geometry, the area A is a known function of flow depth which in turn can be obtained from the head H . Thus the dependent variables in these equations are flow rate Q and head H , which are functions of distance x and time t .

The friction slope S_f can be obtained from the Manning equation.

2.2 Exchange between conduits and porous media

While most of the flow in karst aquifers occurs through conduits, the porous matrix is supposedly important for water storage [38]. In the transient flow regime, this storage influences speleogenesis, while the magnitude of this influence is not self-evident. For this reason, exchange of water between a conduit and porous medium has been investigated by us thoroughly. A novel numerical method has been used and interesting results have been obtained, the results are published in a peer reviewed journal and the article can be found in the Appendix A.

For mature limestones, \tilde{K} would be around 10^{-6} m/s and Φ would be a few percent. The dimensionless examples from the article correspond to our models for l_0 around 1 m. At these parameters, the dimensionless time t would equal 1 at $\tilde{t} \approx 10^7$ s. Looking at the results for V it means that time constant for water

exchange τ would be around 10^9 s. The exchanged volume at such timescales would be $V\Phi_0^2$ for every meter of the conduit or around 1000 m^3 for examples in Sec. 4.1 so the exchange flow would be around $10^{-6} \text{ m}^3/\text{s}$, negligible compared to the flow along the conduit.

As the exchange is negligible compared to the flow along the conduit, it is neglected in the models.

2.3 Modelling of flow

The flow in later stages of speleogenesis is passing mostly through conduits so the modelling of the flow has to account for turbulent flow along them. It has to deal with both pressurised and free surface flow. Calculating the flow through a network of conduits under these assumptions is a major task. However, it is of interest also in fields different from modelling speleogenesis, so software for such calculations is available. To avoid duplicating work we decided to use one of such programs, EPA Storm Water Management Model – version 5.0 (EPA-SWMM). It is a free, open source [35] and well documented program intended for calculating drainage systems.

In our modelling, EPA-SWMM is used to solve Saint Venant equations, Eq. 2.10 and 2.11, while the friction slope S_f is obtained from Manning equation, Eq. 2.9 [34]. From the momentum equation, Eq. 2.11, the inertial terms, the first two terms, are dropped unless noted otherwise [35]. Saint Venant equations are also used for pressurised conduits. It is done using a Preissmann slot, that is with a narrow wedge of additional flow area added to the top of any pressurised conduit in order to artificially keep a free surface [35] as shown in Fig. 2.1. For calculating friction losses, Manning equation is used for partially filled as well as pressurised conduits.

EPA-SWMM conceptualizes a drainage system as a series of water and material flows between several major environmental compartments: the Atmosphere compartment, the Land Surface compartment, the Groundwater compartment and the Transport compartment [35]. In the presented models, only the Transport compartment, meant to represent a sewer network, is used. It is presented schematically in Fig. 2.2. The components of the Transport compartment are modelled with Node and Link objects [35].

Of the Node objects, Junctions and Outfalls are used. Junctions are best depicted as manholes to which Links are connected. The parameters describing them that are interesting in our case are invert elevation, maximum depth and

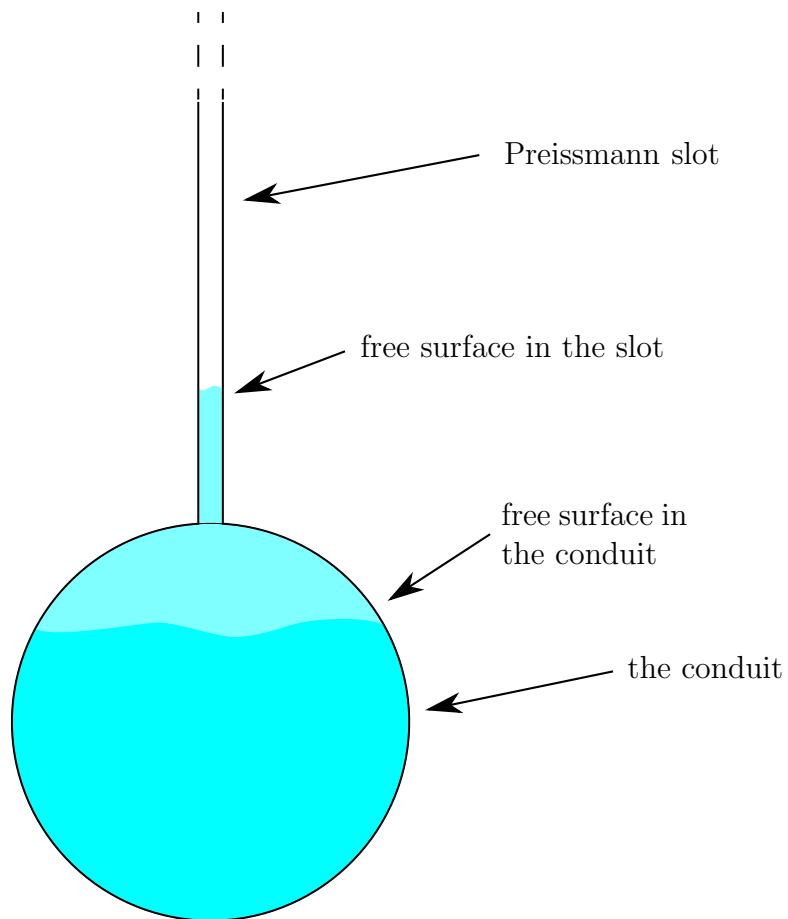


Figure 2.1: The concept of the Preissmann slot. A cross-section of a circular conduit with an additional narrow slot at the top is shown. When the conduit is not pressurised the slot has no influence, while when it is pressurised, the liquid can rise in the slot and keep a free surface so Saint Venant equations can still be used.

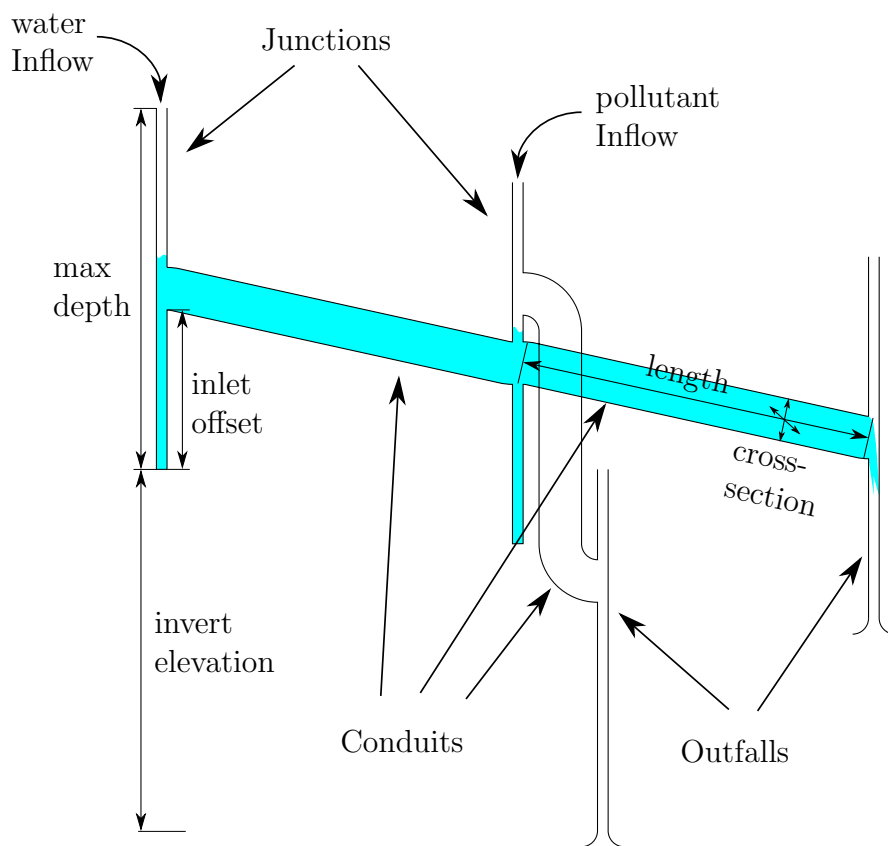


Figure 2.2: The elements of EPA-SWMM that are used in this work.

initial depth. If the head at a Junction would exceed the sum of invert elevation and maximum depth, excess water is lost from the system as if flowing out of the manhole. In modelling speleogenesis, the feature is used to limit the heads in the conduits the way they are limited by the presence of the surface. Outfall nodes define the final downstream boundaries of the system [35]. Their invert elevations set the outflow boundary conditions.

The Link objects used in the presented simulations are Conduits. They represent pipes connecting different Node objects. The main parameters determining them are their length and inlet and outlet offsets - elevations of their lower edge above the invert of relevant Node. The offsets are important because there cannot be any flow from a Junction into adjoining Conduit if its lower edge is above the water table, regardless of the hydraulic head at the other end of the conduit (Fig. 2.3). Great flexibility is also offered in determining Conduits' cross-section geometries. In the presented examples, circular and custom cross-sections are used. Circular cross-section is described by its diameter, while for custom cross-section a Shape Curve object and full height parameter are used to describe it. Shape Curve is described by a list of widths at given depths, where both are normalised with respect to full depth [35]. In our models, widths at 200 equidistant depths were used for each Shape Curve.

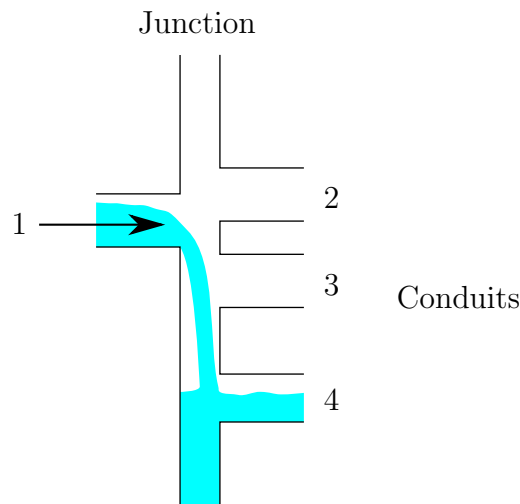


Figure 2.3: Influence of inlet offset on discharge in a SWMM Conduit. A side view of a general SWMM Junction with some adjoining Conduits is shown. As the water level in the Junction is below the Conduits 2 and 3, they do not drain any water from it regardless of the elevation and hydraulic head at the other ends of these conduits.

Of other non-visual objects, in the simulations Inflows are important. They supply water or pollutants to chosen Junctions. Water Inflows are used for

recharge while pollutant Inflows enable calculating advection.

For data exchange between EPA-SWMM and our code, files are used. After an EPA-SWMM run, EPA-SWMM Input and Output files are opened by our code. On their basis, dissolution is calculated, the resulting changes are introduced into Input file and EPA-SWMM is called again to start a new cycle. The EPA-SWMM calculations in the new cycle start from the state in the end of the previous cycle which is saved into EPA-SWMM Hotstart file that is not touched by our code. To produce the final results, archived Input and Output files from every cycle are used.

Chapter 3

Dissolution kinetics in karst aquifers

The chapter addresses the factors influencing rates of dissolution and acting near the rock surface. One of them is chemical kinetics of dissolution which determines mass transport from solid to liquid phase as a function of water chemistry at the surface. The other one is transport of products of dissolution away from the surface and of any reactants toward it. On small scale it is facilitated through molecular diffusion even in turbulent flows.

Depending on lithology and flow conditions, the influence of either one of these steps can be so strong that the other one can be neglected, that is, taken to occur instantaneously. It is also possible that both processes impose similar limits on dissolution rates and both have to be taken into account. In our models, all three possibilities are encountered.

Both theoretical reasoning and most of experimental data show that dissolution kinetics follows a linear law, dissolution rate ought to be proportional to undersaturation of the bulk of the solution. Close to saturation, measured dissolution rates depart from linear law and the effect is important in early stages of speleogenesis [11]. In this work, only linear kinetics is modelled.

3.1 Dissolution rate law in turbulent flow

In the case of linear kinetics, dissolution rate is proportional to the undersaturation,

$$v = \alpha (c_{\text{eq}} - c_{\text{b}}), \quad (3.1)$$

where v is dissolution rate, c_{eq} is equilibrium volume concentration, c_{b} is concentration in the solution far away from the rock surface, and α is a proportionality coefficient. To calculate dissolution in turbulent flow, a diffusion boundary layer model is applied. The flow is presumed to consist of two parts, the bulk and the diffusion boundary layer [9]. The bulk is the central part, it is well mixed and the concentration of the solute in it is uniform and equals bulk concentration c_{b} . Along the walls there is the diffusion boundary layer in which the only mechanism transporting the dissolved ions is diffusion (Fig. 3.1).

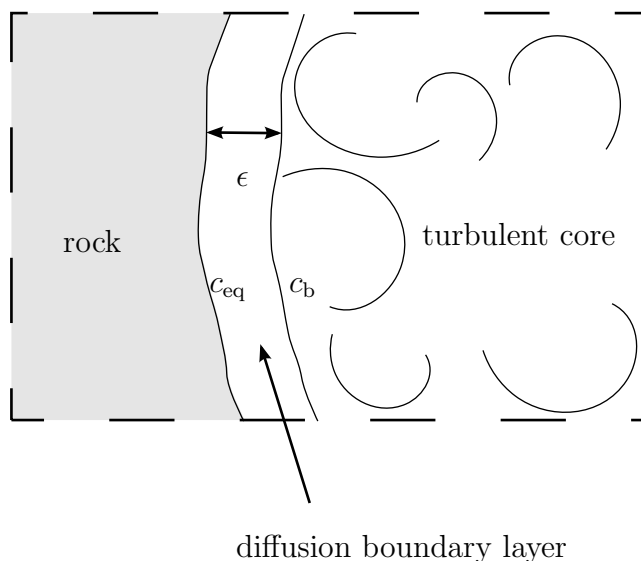


Figure 3.1: The film model adapted from [9]. c_{eq} denotes concentration of ions at the rock surface and c_{b} concentration in the bulk of the solution. ϵ denotes the thickness of the diffusion boundary layer.

Dissolution rates are controlled by the reaction at the rock surface, which in the case of linear kinetics is described as $v_{\text{s}} = \alpha_{\text{s}}(c_{\text{eq}} - c_{\text{s}})$, and transport rates through the diffusion boundary layer $v_{\text{D}} = \alpha_{\text{D}}(c_{\text{s}} - c_{\text{b}})$. c_{s} is concentration of the solute at the mineral surface. Both α_{s} and α_{D} are rate coefficients. After steady-state concentration profiles establish themselves, no storage of solvent is going on in the boundary layer so both expressions can be equated and c_{s} is obtained. By introducing it into either expression, one gets mixed surface-transport rate coefficient in Eq. 3.1:

$$\alpha = \frac{\alpha_{\text{s}}\alpha_{\text{D}}}{\alpha_{\text{s}} + \alpha_{\text{D}}}. \quad (3.2)$$

In the case of some evaporites we expect that $\alpha_{\text{s}} \gg \alpha_{\text{D}}$, so $\alpha \approx \alpha_{\text{D}}$, while in the case of carbonates the opposite limit, $\alpha \approx \alpha_{\text{s}}$, is possible. Note that this model quite adequately describes dissolution in evaporites, while in the case of

carbonates the situation is more complex due to chemical reactions involving CO₂ that are happening inside the aqueous phase [9, 25].

3.2 Rate coefficients

The surface rate coefficient α_s at a particular temperature is a constant. For limestone it is around $2 \cdot 10^{-7}$ m/s as derived from parameters given in [11].

For calculating the transport rate coefficient α_D , the diffusion boundary layer model is used. It assumes a diffusion boundary layer of thickness ϵ at the rock surface where the only mechanism perpetuating mass transfer is molecular diffusion. In the bulk, the region outside of this layer, eddy diffusivity is so high that the concentration of all species is considered to be uniform (see Fig. 3.1) [9]. Thus $\alpha_D = D/\epsilon$, where D is diffusion coefficient.

The thickness of the diffusion boundary layer ϵ is proportional to the thickness of viscous sublayer h : [9]

$$\epsilon = h \cdot Sc^{-1/3}, \quad Sc = \frac{\nu}{D}, \quad (3.3)$$

where Sc is Schmidt number and ν is kinematic viscosity. Kinematic viscosity is defined as $\nu = \mu/\rho$, where μ is dynamic viscosity and ρ is density.

The thickness of pure viscous sublayer over a flat wall is [36]

$$h = 5 \frac{\nu}{u_\tau}, \quad (3.4)$$

where h stands for the thickness of viscous sublayer, ν stands for kinematic viscosity and u_τ is friction velocity,

$$u_\tau = \sqrt{\frac{\tau_\omega}{\rho}}. \quad (3.5)$$

τ_ω is shear stress and ρ is density. The shear stress can be expressed from friction slope S_f

$$\tau_\omega = \rho g S_f \frac{A}{P} = \rho g S_f R. \quad (3.6)$$

P is wetted perimeter and the cross-sectional area A is the product of hydraulic radius R and the wetted perimeter P [14]. From Eq. 3.4, 3.5 and 3.6 it follows

$$h = 5 \frac{\mu}{\rho \sqrt{g S_f R}}, \quad (3.7)$$

where μ is dynamic viscosity.

When h is known, ϵ is calculated according to Eq. 3.3 and α_D is determined. A method for calculating h from the results of EPA-SWMM water flow calculations is thus needed.

The factor $\sqrt{S_f R}$ entering Eq. 3.7 can be expressed from Manning equation (Eq. 2.9) as

$$\sqrt{S_f R} = \frac{Qn}{AR^{1/6}}. \quad (3.8)$$

If the shape of the conduit is held constant, the hydraulic radius R scales with \sqrt{A} . For ordinary geometries, $R \approx \frac{1}{3}\sqrt{A}$. As the numerical factor is of small importance, this relation is used in Eq. 3.8 and by introducing it into Eq. 3.7 one gets:

$$h = 4.16 \frac{\mu}{\rho\sqrt{g}} \frac{A^{13/12}}{Qn}. \quad (3.9)$$

If h is expressed with V instead of A , the equation becomes

$$h = \frac{4.16\mu}{\rho n\sqrt{g}} \frac{Q^{1/12}}{V^{13/12}} \quad (3.10)$$

and according to Eq. 3.3

$$\epsilon = \frac{4.16Sc^{-1/3}\mu}{\rho n\sqrt{g}} \frac{Q^{1/12}}{V^{13/12}}. \quad (3.11)$$

For water, μ is approximately 10^{-3} Ns/m² and $\rho = 10^3$ kg/m³ [29]. The acceleration of gravity g is approximately 9.8 m/s² [29]. Diffusion coefficient of table salt is strongly dependent on temperature and is around 10^{-9} m²/s for the relevant temperatures [33]. Manning roughness coefficient n for smooth pipes is around 0.01 [35]. These values are used, from them it follows $Sc^{-1/3} = 0.1$.

The typical obtained values for ϵ are on the order of 10^{-5} m. For $Q = 10$ m³/s and $V = 0.1$ m/s, $\epsilon = 1.95 \cdot 10^{-4}$ m, and for $Q = 0.1$ m³/s and $V = 10$ m/s, $\epsilon = 9.05 \cdot 10^{-7}$ m.

3.3 Evaporites

The reaction of dissolution at the surface of table salt is fast so $\alpha_s \gg \alpha_D$ and approximately [21]

$$v = \alpha_D(c_{eq} - c_b) = \frac{D}{\epsilon}(c_{eq} - c_b). \quad (3.12)$$

In the case of gypsum, the dissolution reaction is slower so the dissolution rate may be controlled both by dissolution itself and diffusion [21]. As the salt case is the limiting case, it is investigated more into details by either using Eq. 3.12 or using a high value of 1 m/s for α_s in Eq. 3.2 so that it is possible to use the same computer code as for calculating the mixed dissolution cases.

3.4 Carbonates

The dissolution rates of calcite are determined by three rate-controlling processes [25]:

1. the kinetics of dissolution at the mineral surface;
2. mass transport by diffusion of the dissolved material away from the surface and of the reactants toward it;
3. conversion of CO_2 into H^+ and HCO_3^- .

In the literature, there are some doubts in determining which step is the rate-limiting one under which conditions [4, 9]. The dependence of surface reaction rate on the water chemistry is also not fully understood. The relation most commonly used is PWP equation [25] which is empirical fit of many measurement points valid in a very broad range of dissolved species concentrations. Unfortunately, the equation is in disagreement with dissolution mechanism as it contains only one backward term [25]. The precipitation of calcite consists of three different processes and there should be one term describing each one of them. As the emphasis of the work is on the influence of hydraulic conditions, we are looking for the simplest sufficient dissolution model so calculations of the reactions in the dissolved phase are beyond the scope. What we have is:

1. the surface reaction rate that is not well understood;
2. the diffusion that is the same as in the case of evaporites;
3. the reactions in the dissolved phase that are beyond the scope.

In the modelling, the step 1 is approximated by a linear dissolution law. As it is the opposite limit to the salt cases, in some of the models the kinetics of dissolution at the mineral surface is taken to be the rate limiting step, so $v = \alpha_s(c_{\text{eq}} - c_b)$. In particular cases, even c_b is neglected so that dissolution rate is constant. A more realistic model taking both surface reaction rate and diffusion

into account is also used. In it, α_D is calculated just as in the case of evaporites and is combined with α_s according to Eq. 3.2, while α_s is a free parameter of the model. In these cases, the dissolution rate coefficients from [11] are used.

Chapter 4

Evolution of single conduits

4.1 One conduit under constant recharge

In the following cases, evolution of a 30 m long conduit is modelled. Initially it has constant circular cross-section with 4 cm diameter. Along the first 15 m, it uniformly rises for 0.84 m, then it descends again to the initial level. It is modelled as a series of 2 m long horizontal sections, each represented by an EPA-SWMM Conduit object with custom cross-section connecting consecutive Junctions (Fig. 4.1). In every cycle of the program flow, water levels and flows are calculated, dissolution is calculated, and conduit profile is modified according to dissolution (Fig. 4.2).

Advection and dissolution are calculated under steady-state flow assumption. After each change of the cross-sections, the flow at constant recharge is calculated for a long enough time to stabilise. Steady-state dissolution rates and solute concentrations are then calculated. From the dissolution rates, the cross-sections at the end of the timestep are calculated.

4.1.1 Numerical example

Numerical implementation

Build 5.0.015 of EPA-SWMM is used. The procedures for dissolution and advection are written in C++ language and compiled with g++ 4.6.1 compiler. The OS used is Ubuntu 11.10 with Linux kernel 3.0.0.12-generic, 2.0 GiB of RAM and Intel®Core™2 Duo CPU E8400 with 3.00 GHz clock cycle. A calculation of a typical example with 1 000 cycles similar to Example 1 takes approximately 5 min.

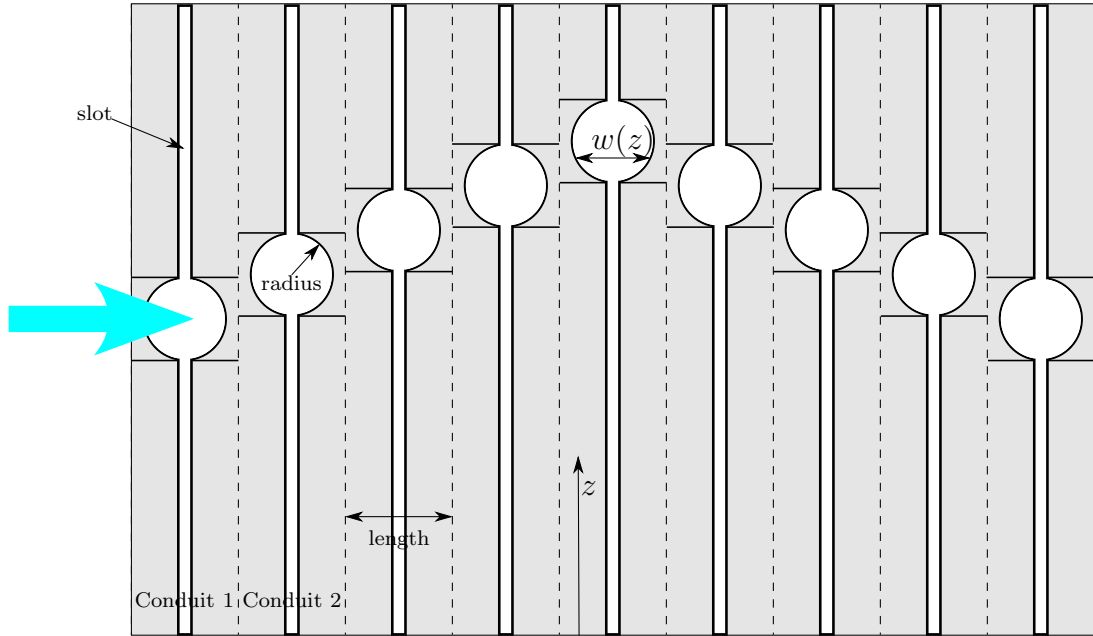


Figure 4.1: Initial profile of the conduit with its cross-sections. The conduit is assembled as a series of Conduit objects connected at Junctions. Soluble rock is grey, dashed lines delimit particular Conduits, they represent Junctions. Their cross-sections are the white shapes with black border. Radius of the conduit is 4 cm and the length of each Conduit is 2 m. Note that the figure should not be interpreted as if depicting a single big cross-section.

Flow

The shape of an EPA-SWMM Conduit object is defined by a series of widths $w(z)$, where the coordinate z passes from its bottom to the top. The horizontal coordinate axis perpendicular to the conduit is labelled x while the one along the conduit is y . EPA-SWMM demands a small positive width at every elevation inside a Conduit. Thus every Conduit is at the beginning of the simulation taken to be 2 m high and very narrow (0.2 mm wide) everywhere except at the position of the initial conduit (Fig. 4.1). This conduit is positioned only in the top half of the Conduits, its ends are centred at $z = 1$ m where z is measured from the bottom of the Conduits. Thus some space is left for entrenchment. Resolution of the defined shape in z direction is 1 cm. The maximum hydraulic head at all the Junctions is taken to be 5 m (that is, water overflows if it reaches $z = 5$ m).

The narrow part of the Conduit cross-section is similar to Preissmann slot. As Preissmann slot is automatically added by EPA-SWMM to the top of every pressurised Conduit and its influence on calculated flow is acceptable, the artificial narrow part should be acceptable too.

The initial condition for water flow and levels is the same for all the presented

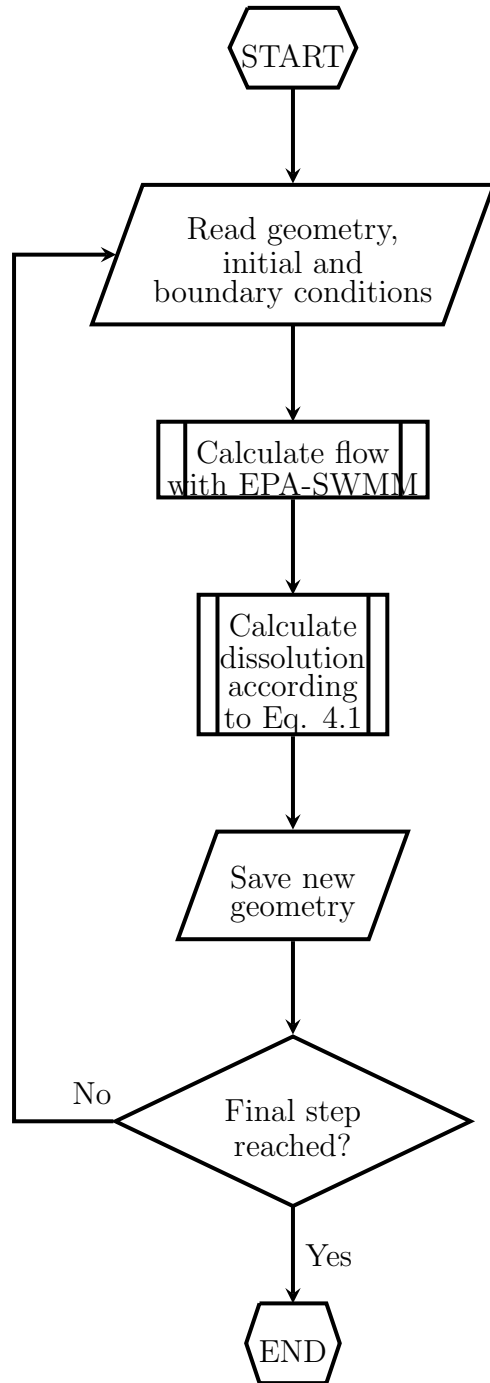


Figure 4.2: Flowchart of the solution procedure.

cases. It is determined with EPA-SWMM starting from dry conduits and running the simulation for 1 month with constant inflow of 1 l/s.

Dissolution

In the narrow part of a Conduit, no dissolution is allowed, as shown in Fig. 4.3.

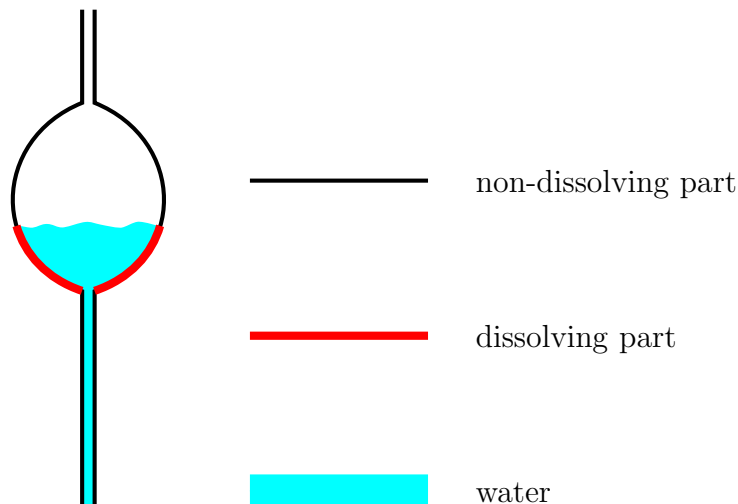


Figure 4.3: Dissolution is active in parts of the Conduit object that are both wet and representing the real conduit.

Eq. 3.11 does not account for any local differences in the viscous sublayer thickness inside a given cross-section. These differences do exist: around a rock protruding into the center of the passage the viscous sublayer is thinner than inside a narrow crack in the wall. Shear velocities on different parts of the cross-section are different, and so are the resulting shear stresses and viscous sublayer thicknesses. Some empirical methods for calculating velocity fields do exist in the literature [31]. They are neither easy to implement nor fast to compute. Furthermore, they are meant for calculation of discharges, where in contrast with our case the situation near the walls is of least importance. Therefore, a new procedure for calculating ϵ is proposed.

A point in a corner of the cross-section is less influenced by the bulk of the flow as a point at a flat wall. For points in corners where two flat walls meet, the viscous sublayer thickness is estimated to be inversely proportional to the angle of the corner. For a point on a generally shaped wall, a generalisation of the method is used: the angle is measured through the chosen point and two auxiliary points on the wall in its vicinity, one on each side of it. The distance from the central point to the auxiliary points has to be chosen and an obvious choice is the thickness of the diffusion boundary layer ϵ . It is solved for iteratively

over 5 iterations. As a first approximation, ϵ from Eq. 3.11 is used. The angle is determined, ϵ is divided by the ratio of this angle to straight angle, the angle for the new ϵ is determined and so on. There is no guarantee that the procedure converges or that the solution is unique. Nevertheless it is estimated that the solution is approximately correct most of the time. In this way, $\epsilon(z)$ is obtained as illustrated in Fig. 4.4. As can be seen in Fig. 4.5, any protrusions from other walls entering the circle of radius ϵ around the point are subtracted from the angle too. For a point at a flat wall, the procedure gives the same result as Eq. 3.3.

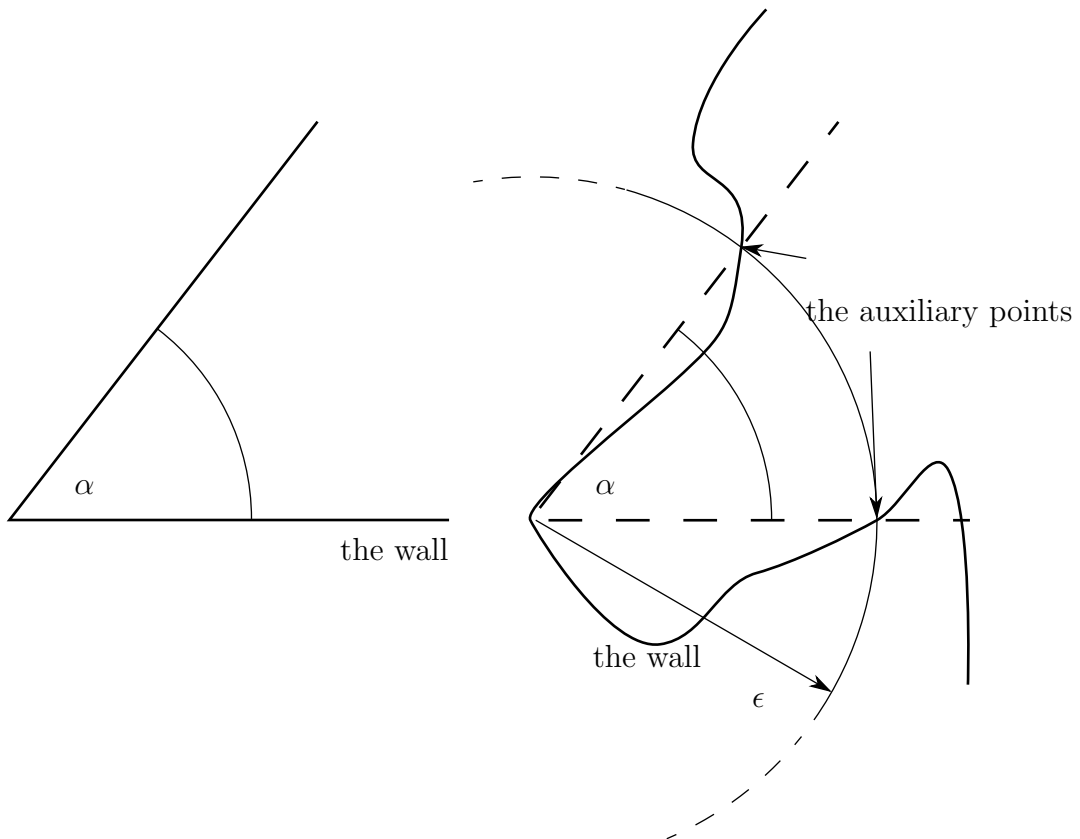


Figure 4.4: Determining the viscous sublayer thickness. The left example is for a point in a corner, the right one is the generalisation for an arbitrary shape of the wall.

The z -dependent dissolution rate $v(z)$ is calculated according to a z -dependent form of Eq. 3.12:

$$v(z) = \frac{D}{\epsilon(z)} (c_{\text{eq}} - c_{\text{b}}). \quad (4.1)$$

The bulk concentration c_{b} is increasing along the flow so its average for the Conduit should be used. However, the model assumes a constant cross-section and uniform conditions for each Conduit, so the change in bulk concentration along a single Conduit object has to be small. Therefore, the concentration at

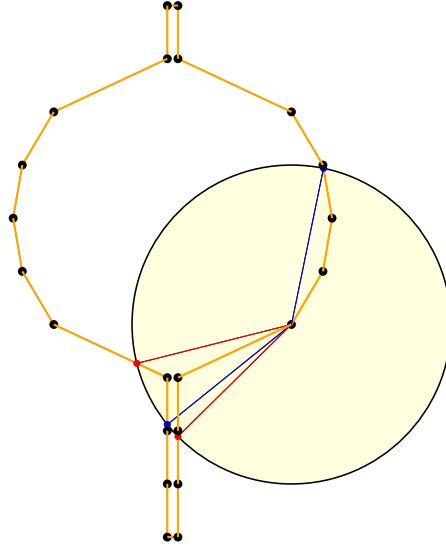


Figure 4.5: Demonstration of the algorithm for estimating ϵ . The sketch has been drawn by the implementation of the algorithm as a test. The circumference of the Conduit is represented by the orange line, the black dots at the junctions of straight line segments are the points defining it. ϵ for the point in the middle of the big bright yellow disk with black edge is being estimated. The radius of the circle equals initial guess for ϵ . The blue and the red points are the auxiliary points, the estimated influence of the bulk flow is proportional to the sum of the angles between blue and red radii.

one of the ends can be used as c_b . The concentration at the downstream Junction is chosen because it would represent the average concentration well in the other limiting case, when water flow is so small that in the Conduit equilibrium is approached, too. The calculation is also always stable this way.

c_b is calculated as

$$c_b = c_{b0} + \frac{\iint v(z) dA}{Q}, \quad (4.2)$$

where c_{b0} is the bulk concentration at the upstream end and integration is over all the exposed rock face. As the section is presumed to be translationally symmetric in y direction, one integration can be substituted for multiplication and only integration along the wetted perimeter remains:

$$\iint v(z) dA = \Delta y \int v(z) \frac{dl}{dz} dz, \quad (4.3)$$

where Δy is the length of the conduit section, denoted as “length” in Fig. 4.1. The ratio between element of circumference and element of coordinate dl/dz equals

$1/\sin \varphi$ where φ is the slope of the wall measured from horizontal. Thus

$$\iint v(z) dA = \Delta y \int v(z) \frac{dl}{dz} dz = \Delta y \int v(z) \frac{1}{\sin \varphi(z)} dz. \quad (4.4)$$

The slope $\varphi(z)$ is calculated from the cross-section. It should be noted that not the whole cross-section is enlarged, only the parts that are both under water and not in the narrow part at the same time. The widening is proportional to $1/\sin \varphi$:

$$\frac{\partial w(z)}{\partial t} = v(z) \cdot \frac{1}{\sin \varphi(z)}. \quad (4.5)$$

A point from the narrow part enters the conduit when two conditions are fulfilled. Its nearest and next nearest neighbours on one side have to be in the conduit. At the same time, the point and the two neighbours have to form a concave part of the wall, that is, a straight line connecting the end points lies in the conduit and not inside the rock (Fig. 4.6).

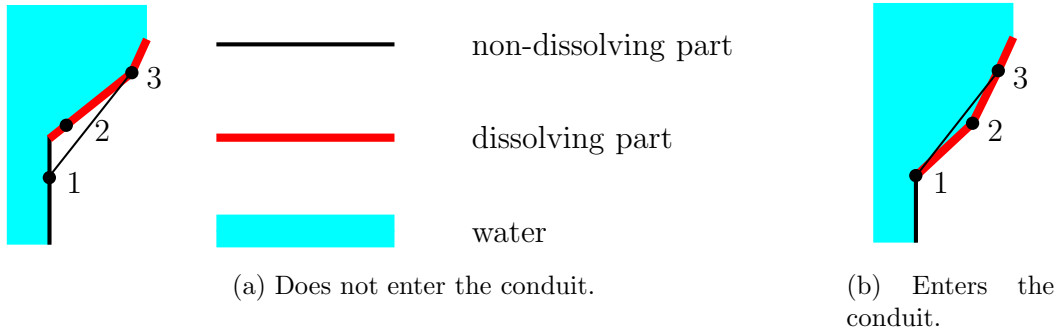


Figure 4.6: The points 2 and 3 form part of the conduit wall while 1 is in the narrow part. In the case (a), 1 remains in the narrow part as the line from 1 to 3 is in the rock. In the case (b), the line from 1 to 3 is in the conduit and 1 joins the part that is being dissolved.

Advection

In a single conduit, advection is calculated in a straightforward way. The calculation of dissolution starts at the upstream part of the conduit and proceeds in the downstream direction. Along the flow, the bulk concentration of dissolved species is increased according to the local dissolution rate and flow. The underlying assumption is that during the time the solution needs to pass through the system, the dissolution rate at each point does not change significantly, so the timescales can be separated.

In practical implementation it means that in the following Conduit, the resulting downstream concentration c_b of the previous Conduit is used as c_{b0} .

The plots

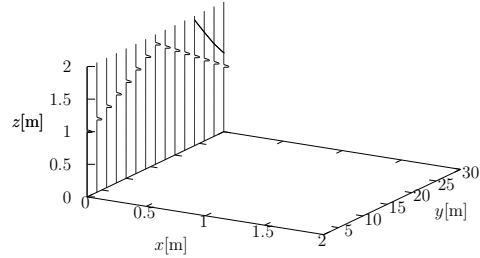
To visualise the results, cross-sections of Conduits at a particular instant are drawn. They are shown on 3D graphs. Particular cross-sections are drawn as width of the Conduit as a function of depth, where depth is shown on z axis and width in x direction. Consecutive Conduits are drawn at increasing values of y . In this way, the cross-sections give impression of an outline of the conduit in space. On this outline it can easily be seen how the evolution of the conduit is progressing, how the conduit is being incised or widened. In the case of free surface flow, the water level in the conduit is shown as a (blue) surface inside the outlined conduit.

Results

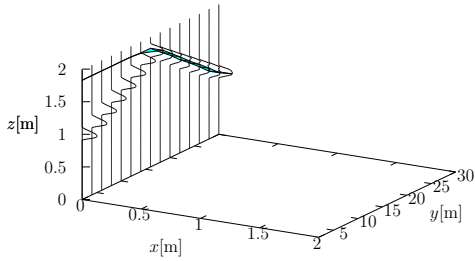
Example 1 Dissolution of salt under constant recharge of 1 l/s is modelled, c_{b0} in the first Conduit is 0. In every cycle 90 s of dissolution are simulated. The flow is left to stabilise for a longer time, for 1 h, after each change in geometry so that an approximation of a steady-state solution for flow is reached. This can be done because dissolution and advection are calculated separately from the flow. Steady-state solution for the flow is needed because concentrations are calculated under steady-state assumption. The result is saved every 10 cycles, that is every 15 min of dissolution. The simulation runs for 800 cycles = 20 h. Some of the results are in Fig. 4.7.

Example 2 Everything is identical to Example 1 except the bulk is taken to be completely unsaturated, $c_b = 0$, in all the Conduits. From Fig. 4.8 it can be seen that the results are very similar to the results for Example 1. It tells us that the examples in this part of parameter space are not influenced much by advection. The length scale needed for c_b to change significantly is much longer than the modelled system. If a longer conduit was modelled or the flow rate was smaller, the results that included modelling of advection would be significantly different from the ones where $c_b = 0$ is presumed.

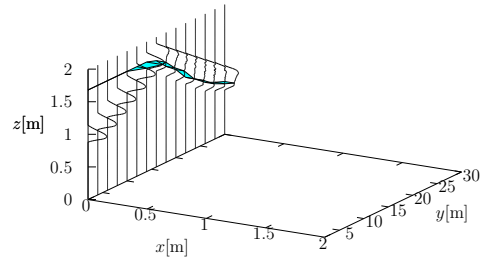
Example 3 Example 2 is further simplified to correspond to the model of limestone where the surface rate is the only step limiting the dissolution. The kinetics of surface reaction is taken to be the rate limiting step and $\alpha = \alpha_s$ is presumed.



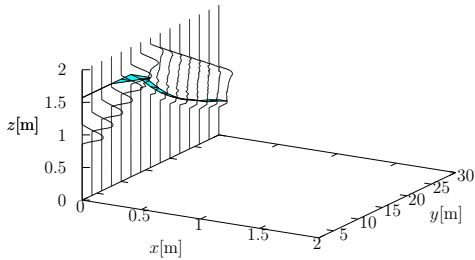
(a) At the very beginning of the simulation.



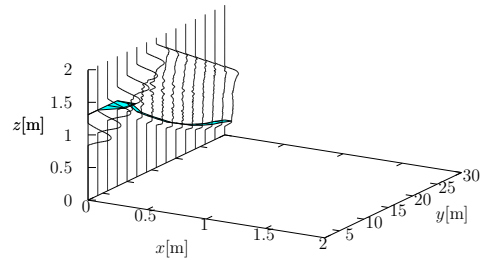
(b) After 200 steps (5 h) of dissolution.



(c) After 400 steps (10 h) of dissolution.

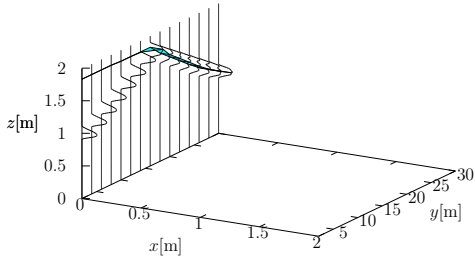


(d) After 600 steps (15 h) of dissolution.

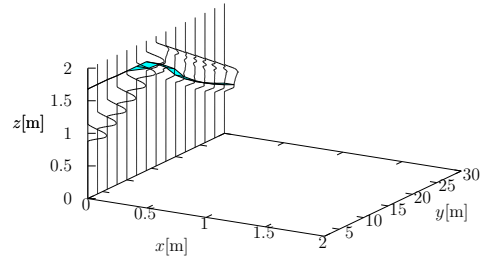


(e) After 800 steps (20 h) of dissolution.

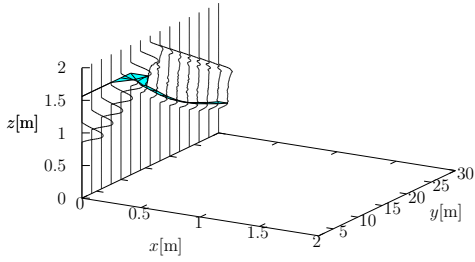
Figure 4.7: The conduit shape and the water level at various stages of the simulation of speleogenesis in salt. For every cross-section, passage width as a function of elevation is drawn. Water surface is drawn in every Conduit that is not pressurised.



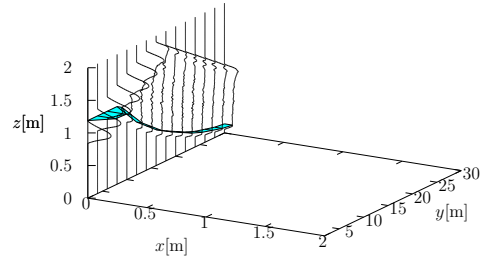
(a) After 200 steps (5 h) of dissolution.



(b) After 400 steps (10 h) of dissolution.



(c) After 600 steps (15 h) of dissolution.



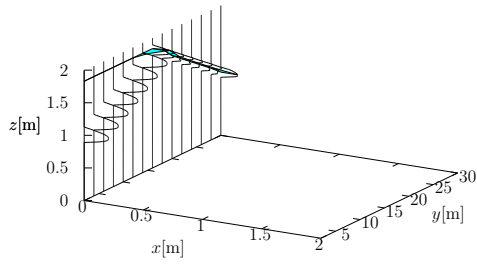
(d) After 800 steps (20 h) of dissolution.

Figure 4.8: The conduit shape and the water level at various stages of the simulation of speleogenesis in salt with $c_b = 0$.

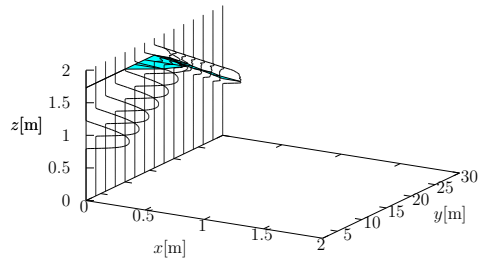
As $\alpha \ll \alpha_D$, advection has even less influence than in the case of salt. Thus neither the thickness of diffusion boundary layer nor advection is calculated, instead of it the rate of dissolution is taken to be constant and equal to 0.0004 m per simulation step everywhere in the part of the Conduit that is being dissolved. The dissolution rate constant is not determined so the timestep duration is not known. If the constant was chosen the duration of each step would be fixed by it. The results are presented in Fig. 4.9.

Example 4 A straight conduit under constant recharge conditions develops into a channel that is entrenching downwards. The width of the channel bottom is going to stabilise in time: if it grows too wide, the flow near the shore will slow down and lower the local dissolution rate, while if it is too narrow, the flow and the dissolution rates will be slowest near the center of the bottom and the bottom will widen.

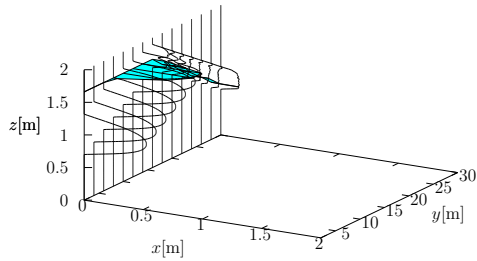
The influence of the amount of recharge on the stabilised width of the resulting channel is investigated. The method from Example 1 is used, the initial condition is the same flooded conduit. 7 runs with recharges ranging from 0.1 l/s to 100 l/s are calculated, every run continues for 15 000 cycles of 90 s of dissolu-



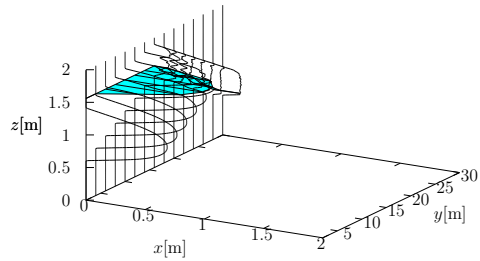
(a) After 200 steps of dissolution.



(b) After 400 steps of dissolution.



(c) After 600 steps of dissolution.



(d) After 800 steps of dissolution.

Figure 4.9: The conduit shape and the water level at various stages of the simulation of speleogenesis in limestone.

tion. Afterwards, the width of the 8th Conduit at $z = 1$ m $w_{8,1}$ is taken. After such a long run, the final width has already been reached and the measurement site is dry.

The results are presented in Tab. 4.1. It can be seen that there are significant differences between different examples. However, the width does not depend only on the flow rate but also on the slopes and boundary conditions and is not uniform in z dimension so we do not look for any trends.

Discussion

Examples 1 and 2 give very similar results. The only difference between them is increasing c_b as a result of dissolution and advection versus approximation $c_b = 0$. This means that on the scale investigated here advected solute does not have much influence. Both results are also similar to the examples that can be seen in nature, in salt as well as in limestone.

In contrast, the results obtained for limestone in Example 3 differ considerably both from Examples 1 and 2 and from the situation observed in nature. Entrenchment is relatively slow while in the flooded parts the cross-sectional areas

Q [l/s]	$w_{8,1}$ [m]	remark
0.1	0.050	EPA-SWMM instability at low flow
0.3	0.029	
1	0.029	
3	0.047	
10	0.087	
30	0.113	might be influenced by the domain boundaries
100	0.214	might be influenced by the domain boundaries

Table 4.1: Dependence of channel width on recharge. At the lowest recharge, EPA-SWMM is unable to route the flow properly. The results for the two highest recharges seem to be influenced by the boundaries of the computational domain, that is, if the domain was extended, the result would probably be different. The other results are meaningful for the initial geometry considered.

are increasing steadily. The flow is thus getting slower, diffusion boundary layer is increasing and the model is evolving toward the setting where the presumption of surface-limited dissolution is no longer valid. It proves that in modelling limestone a bit more sophisticated model taking both surface reaction and diffusion into account is needed. Sediment deposition, which is an interesting question by itself and is neglected in this work, would also start to influence the evolution in such conditions. The obtained results for limestone are thus highly suspicious, the results for salt much less so.

Example 4 shows that the models can be used to predict the width of an entrenched channel.

4.2 Conduits under transient recharge and in basic systems

4.2.1 Comparison to a single conduit and constant recharge

Transient flow may influence speleogenesis [20] but the effect has not been investigated thoroughly. What has been done is modelling changes in recharge on timescales that are longer than timescales of changes in aquifer characteristics [11] as a series of different steady states. It does not cause any additional computational overhead but is useful for investigating the effects of long-term climate changes. On the other hand, under free surface flow condition it is important to model transient behaviour on shorter timescales, such as changes caused by droughts and rainshowers, as they influence the water table and the states are

not steady due to water storage.

In the early stages of speleogenesis, under fully flooded conditions and when the water velocities are still low enough for the flows to be laminar, the flow equations are linear [11] and differences in recharge do not have any qualitative influence on water flow. Multiplying the inflows by some factor multiplies the flows in all the conduits by the same factor. The only possibility for the recharge to influence the final outcome and not only the timescale of speleogenesis is through the dissolution length scales that do change with changing flow rate [6].

In the later stages but still under fully flooded conditions, flow becomes turbulent, the equations are no longer linear and the amount of recharge can influence the ratios of flows in different conduits. There are then more possibilities for recharge to influence speleogenesis. However, modelling results mostly show that the dominant conduits that get enlarged in the later stages are already determined in the early stages of speleogenesis [32]. This influence of transients in recharge is thus presumably too late to affect the outcome.

In unconfined aquifers, another variable influenced by recharge and influencing speleogenesis is the position of the water table. The algorithms for finding the water table in the existing karst aquifer models are built on the assumption of steady-state flow [11]. Either full pipe flow or no flow is assumed in all the conduits [11], except in laminar models [1], so the behaviour near the water table is not resolved well.

In our investigations of free surface flow and its influence on passage cross-sections it is necessary to model transient behaviour because the cross-sections might be shaped by oscillations in the water table in an important amount.

As long as only a single conduit is modelled, the diversity of possible outcomes is strongly limited. The volume of water passing through each segment of the conduit is the same, the concentration of the solute can only increase in the downstream direction, and influence of conduit evolution on water flow is limited. Modelling a basic system with more parallel conduits is thus an important generalisation and worth exploring. The computing time needed to calculate such an example with two conduits is of the same order of magnitude as for a single conduit so it is not necessary to leave out any details. To conclude, the advances in this section compared to 4.1 are two parallel conduits and variable rate of inflow.

4.2.2 Numerical example

Flow

The method from 4.1.1 is used.

Dissolution

Dissolution is calculated according to Eq. 4.1, any reaction at the surface is presumed to be instantaneous. The average bulk concentration has to be obtained in a different way than in Sec. 4.1 since the concentration in the downstream Junction is not useful because the water there might be mixed with water from another Conduit. Thus only the upstream concentration in the solution entering the Conduit might be used. The upstream concentration does not always represent a good approximation for the average bulk concentration so a better estimate is calculated from it. The change in concentration along the Conduit is calculated by integration, the total amount of dissolution is calculated from the change in concentration and the change in cross-section follows from it.

By definition of volume concentration c , its gradient in the direction of flow y is:

$$\frac{dc}{dy} = \frac{\int v(z) dl}{Q}. \quad (4.6)$$

Taking into account the expression for dissolution of table salt, Eq. 3.12, Eq. 4.6 becomes

$$\frac{dc}{dy} = \frac{(c_{\text{eq}} - c)}{Q} \int \alpha_{\text{D}}(z) dl. \quad (4.7)$$

The integral $\int \alpha_{\text{D}}(z) dl$, where $\alpha_{\text{D}}(z) = D/\epsilon(z)$, can be numerically evaluated and we label it $\int \alpha_{\text{D}}(z) dl = \alpha'P$. From Eq. 4.7 we get

$$\frac{dc}{(c_{\text{eq}} - c)} = \frac{\alpha'P}{Q} dy. \quad (4.8)$$

Integrating along the Conduit, we get

$$\log(c_{\text{eq}} - c) \Big|_{c_{\text{b0}}}^{c_{\text{b}}} = -\alpha' \frac{A}{Q}. \quad (4.9)$$

Here, c_{b0} stands for bulk concentration at the upstream end of the Conduit and c_{b} is the concentration at the lower end. Their difference Δc is

$$\Delta c = c_{\text{b}} - c_{\text{b0}} = \left(1 - e^{-\alpha' \frac{A}{Q}}\right) \cdot (c_{\text{eq}} - c_{\text{b0}}). \quad (4.10)$$

The total volume flow of rock from the conduit walls is thus known:

$$\iint v dA = Q \Delta c. \quad (4.11)$$

Enlargement $\partial w(z)/\partial t$ is calculated the same way as in Sec. 4.1 and normalised to the calculated total volume flow of rock.

Advection

Advection has to be calculated in a different way than in Sec. 4.1 because the flow no longer follows a single branch and the assumption of steady-state chemistry is also no longer valid. The pollutant routing code of EPA-SWMM is used. It treats the pollutants as conservative tracers influenced only by advection so it can be coupled to dissolution. The dissolved salt is added as an Inflow at the Junction downstream from the Conduit where it dissolves.

Results

In the presented cases, evolution of a 26 m long system of two parallel conduits is modelled. It is modelled as a series of 2 m long horizontal sections, each represented by an EPA-SWMM Conduit object with custom cross-section connecting consecutive Junctions. From the upstream end, for the first 4 m there is only one conduit. Initially it is circular with diameter 0.5 m and center 1 m above the lower edge of the simulated volume. From there on, for 18 m there are 2 parallel conduits. At first, the diameter of the upper one is 0.4 m. From initial level with center 1 m above the lower edge, it rises uniformly for 0.5 m in its first half and in the second half falls back to the same level. The other conduit is horizontal, its diameter is 0.1 m and its center is again 1 m above the lower edge. They join together at their ends and continue as one 4 m long conduit of 0.5 m diameter. The setting can be seen in profile view in Fig. 4.10.

Just like in the case of a single conduit in Sec. 4.1, the Conduit objects are 2 m high, their widths are given at 1 cm distances in elevation and they are 0.2 mm except in the conduits. The head at the Junctions is limited to 5 m again. All the cases are calculated for salt.

Example 1 To get the initial condition, the model is run for 5 000 cycles of 50 s at recharge 100 l/s without applying dissolution to the shapes of the conduits. In every cycle, flow and advection are calculated and dissolved material is added to respective Inputs but is not removed from the conduit walls. From such a

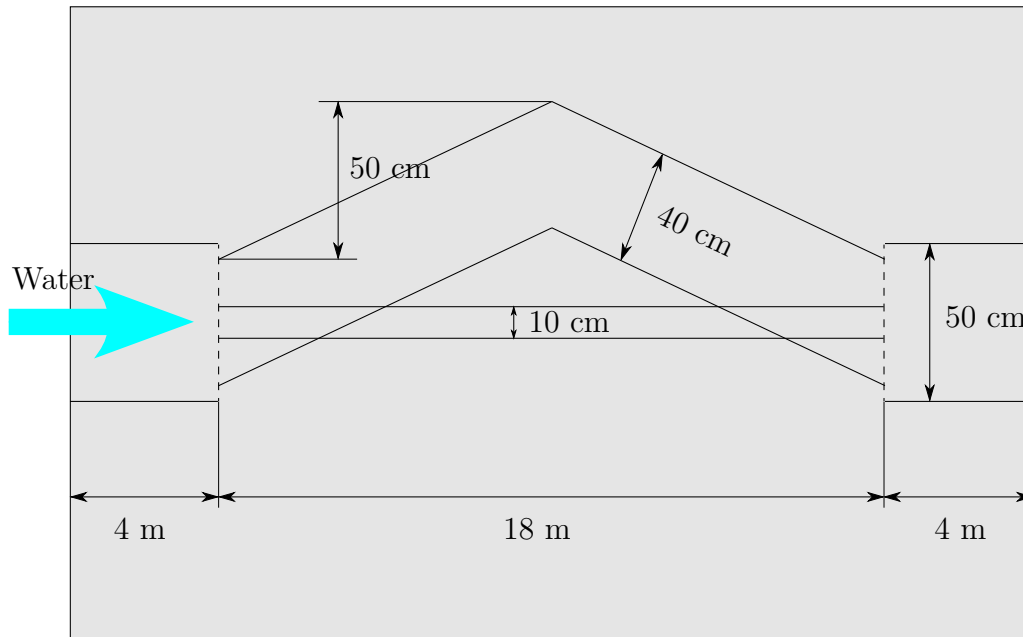


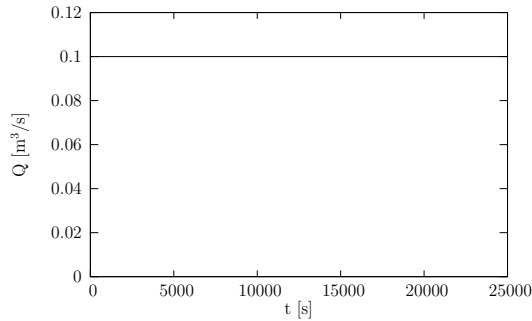
Figure 4.10: The system in profile view. All 4 conduits are shown.

stabilised situation, influence of dissolution is calculated for 500 cycles of 50 s at the same constant recharge. The model run is long enough that one of the parallel conduits dries up. Some of the results are presented in Fig. 4.11. The way of presenting the results is basically the same as in Sec. 4.1, only in the part where there are two parallel conduits one of them is translated in x direction to avoid overlap.

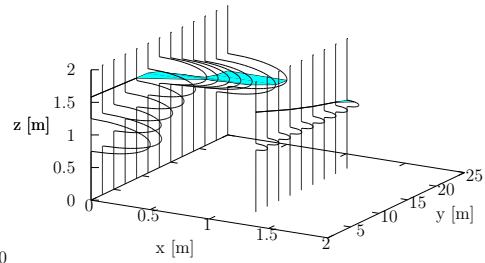
It can be seen that initially both parallel conduits are growing while the dissolution rates are highest in the wetted part of the descending conduit segment, there ϵ is the smallest. The conduit is both incising and widening. Later on, the lower conduit is enlarged enough to discharge ever bigger fraction of the flow. At the end of the simulation, all the water is flowing through the lower conduit so the upper conduit is not evolving and also has no influence on evolution of the rest of the system.

Example 2 The run starts from the same initial condition as Example 1 and also runs for 500 steps of 50 seconds. The difference is in recharge: for 10 cycles, 100 l/s of water is supplied, and for next 90 cycles only 10 l/s, and then 100 l/s again. The results are presented in Fig. 4.12.

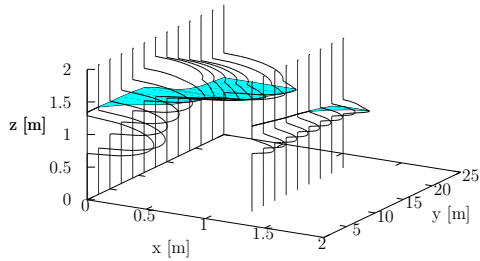
During most of the simulation, the upper conduit is discharging part of the flow only at times of bigger recharge, while the whole low flow is transmitted through the lower conduit. In the end, the lower conduit is evolved enough that it transmits all the water also in periods of high recharge. The influence and



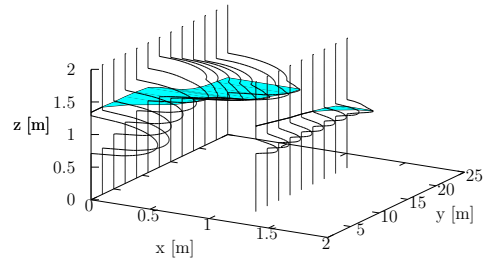
(a) Time dependence of recharge.



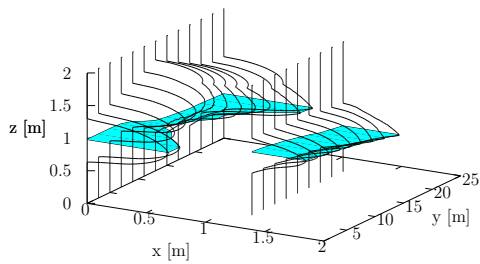
(b) At the beginning of the simulation.



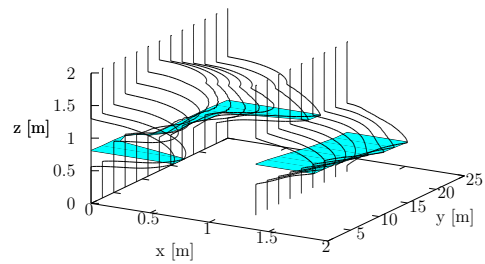
(c) After 100 cycles (5 000 seconds) of the simulation.



(d) After 200 cycles (10 000 seconds) of the simulation.



(e) After 300 cycles (15 000 seconds) of the simulation.



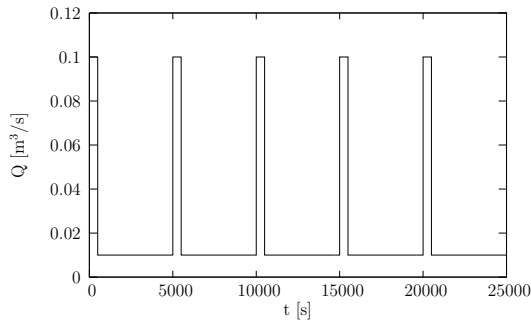
(f) After 400 cycles (20 000 seconds) of the simulation.

Figure 4.11: The conduit shape and the water level at various stages of the simulation of speleogenesis in the system of two parallel conduits at constant recharge. For every cross-section, passage width as a function of elevation is drawn. In the part where there are two parallel conduits, the cross-sections for one of them are offset in x direction.

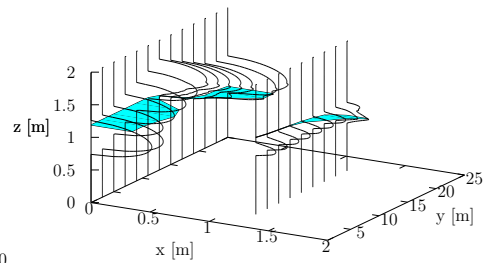
evolution of the upper conduit end by this stage. Evolution of the system is similar to the one in Example 1.

Discussion

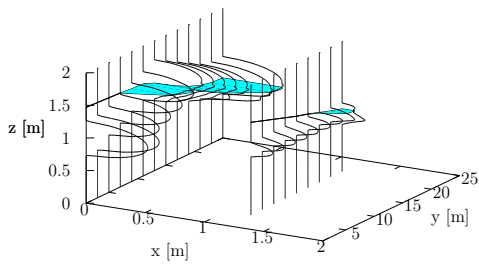
Comparing the cases with pulsed recharge to the cases where recharge is constant, not much difference can be seen. In the shown pulsed case, the lower part of the wall of the upper conduit is more rugged, which is the only noticeable difference between the two examples. When comparing cross-sections and longitudinal profiles, we never found a result of variable recharge that would be very different from the results of constant recharge. For any pulsed recharge model run we checked, there is a constant recharge model leading to a similar outcome.



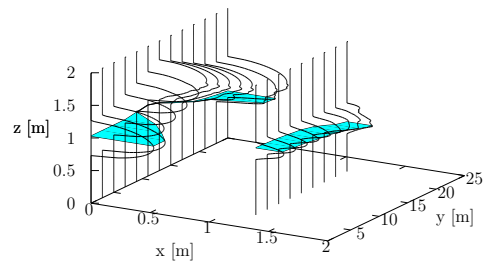
(a) Time dependence of recharge.



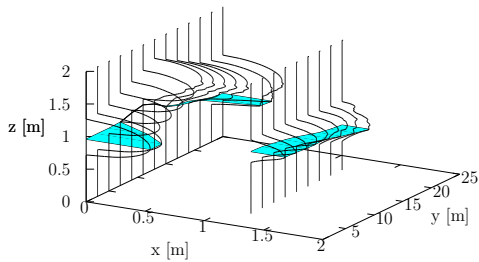
(b) After 100 cycles (5 000 seconds) of the simulation when recharge is low.



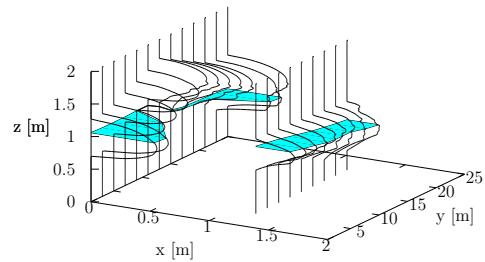
(c) After 110 cycles (5 500 seconds) of the simulation when recharge is high.



(d) After 200 cycles (10 000 seconds) of the simulation when recharge is low.



(e) After 300 cycles (15 000 seconds) of the simulation when recharge is low.



(f) After 410 cycles (20 500 seconds) of the simulation when recharge is high.

Figure 4.12: The conduit shape and the water level at various stages of the simulation of speleogenesis in the system of two parallel conduits at variable recharge.

Chapter 5

Evolution of conduit networks

Apart from detailed analyses of shorter segments of conduits, the method of modelling is applied to a larger network of conduits. We study various geometries under various boundary conditions and different cross-sections of the model domain. For example, with models representing an almost vertical plane, vertical development of vadose systems is studied. With low dip (nearly horizontal) models, the evolution of branchwork cave systems is checked out. Models of different levels of complexity are used, starting from simple ones.

The topology of the modelled system is a square grid of nodes connected with circular conduits. The conduits are circular because profile evolution of individual conduits is not investigated, the emphasis is on the whole network. All the boundary conditions can be varied. On every node, the elevation of each connected conduit ending is prescribed separately. The maximum head and eventual additional water recharge are also set. All these parameters can be varied during the model run. The flexibility suffices to model a lot of interesting cases.

Since many examples are calculated, they are enumerated. The numbers used do not have any special meaning.

5.1 Numerical example

5.1.1 Flow

The nodes of the network are represented as EPA-SWMM Junction objects. We mostly simulate a 11×11 nodal grid, resulting in 121 nodes and 220 conduits. Their invert elevations are set according to the needs of the particular model run. The maximum depths at Junctions are taken to be big enough to prevent water

spillage from the system except when needed otherwise.

Conduits are modelled as EPA-SWMM Conduit objects that connect Junction objects representing nodes. They are circular, their Inlets and Outlets are initially set high above Junction inverts to make space for eventual downcutting. In most cases their initial diameter is taken to be at least 0.005 m. Otherwise, the flows through them tend to be rounded off to 0 so no dissolution is going on and the results are inconsistent.

EPA-SWMM demands that the system has some explicitly defined water outfall. For this purpose, EPA-SWMM Outfall objects are used. They have Inverts at elevation 0 and are connected to the Junctions where free outflow is needed with additional Conduits. These conduits have Inlet and Outlet offsets 0 and are typically 100 m long because the length cannot be smaller than the altitude difference. However, they never present a significant obstacle to the flow as their diameter is 5 m.

The initial conditions for the water levels for particular model runs are calculated by EPA-SWMM. The flow routing is run for 1 day with steady-state boundary conditions and the result is used as the initial condition for modelling the evolution. The flow simulation begins with water depth near maximum depth at every Junction so that all the Conduits are flooded and approach to steady state is fast. The initial condition obtained in this way is thus close to the steady state.

Each Junction has both water and salt Inflow. Water Inflows are prescribed for every cycle of the model (and are 0 for most Junctions in all the presented cases). In the steady state cases, the water inflows used for calculating initial conditions are equal to the inflows in the model. All the salt inflows are set to 0 in calculating the initial condition so water is initially completely unsaturated.

5.1.2 Dissolution

Eq. 4.11 is valid and useful also in these cases. For A in Eq. 4.10 the wetted part of the Conduit is used, calculated from diameter and water depth. For diffusion boundary layer thickness, the ϵ for flat wall from Eq. 3.11 is used. In this way, α_D is independent of z , integration in Eq. 4.7 can be turned into multiplication and α' in Eq. 4.10 becomes α_D . It is further substituted with α from Eq. 3.2 so that both limestone and salt cases can be calculated with the same code. For salt, the value of α_s is taken to be 1 m/s so that $\alpha \approx \alpha_D$. For limestone, the values used are $\alpha_s = 2 \cdot 10^{-7}$ m/s, $c_{eq} = 0.0001108$ and $D = 10^{-9}$ m²/s. All the examples are for salt except if noted otherwise.

As the Conduits are circular, the diameters are increased in accordance to increase in their volumes. Their inlet and outlet offsets are also changed. In phreatic conditions, they are lowered as to keep the centre at constant position. Under vadose conditions they are lowered so that the rate of lowering of the bottom of a conduit equals the dissolution rate in the conduit (Fig. 5.1). In this way, the lowest part of the conduit is positioned properly. This choice was made because the elevation of the lowest part determines if the water will flow through the conduit or not (Fig. 2.3) and the lowest part is also the most frequently wetted one.

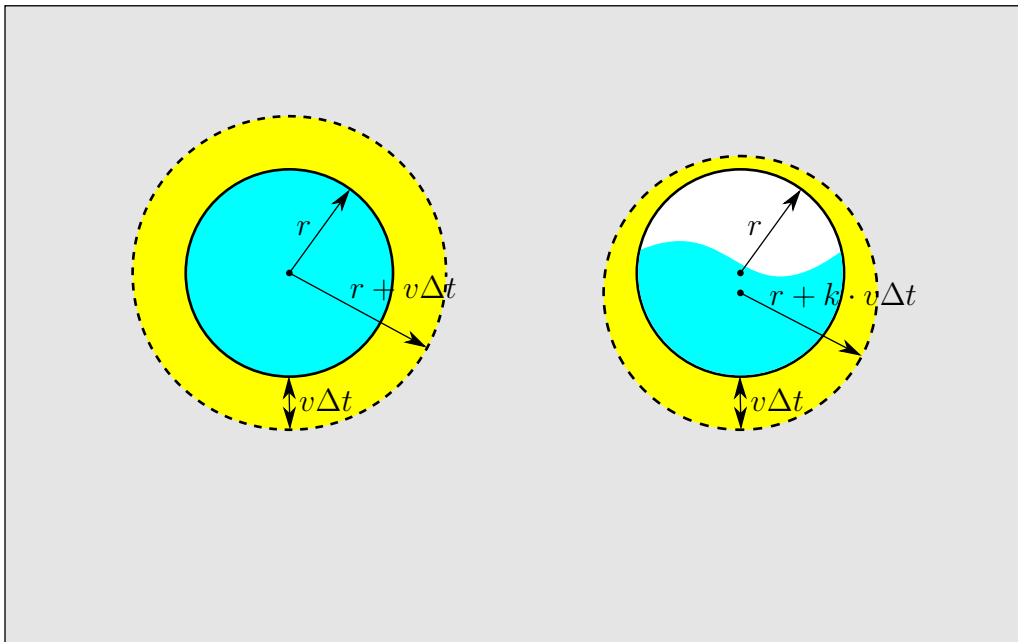


Figure 5.1: Enlargement of circular conduit cross-sections. In a timestep Δt , pressurised conduits enlarge for $v\Delta t$ in all directions, keeping the center of the conduit fixed. In conduits with free water surface, the bottom lowers for $v\Delta t$ and the conduit radius increases for $k \cdot v\Delta t$, where k is the fraction of the conduit wall that is under water.

5.1.3 Advection

The method from Sec. 4.2 is used.

5.2 Results

5.2.1 Graphical representation

The results are drawn in the plane of the grids. When describing the graphs, relative positions of their parts are named by cardinal directions to avoid any confusion with the coordinates in the model itself. The part of the grid that is drawn on the left side of the graph is named west, the part that is drawn at the top is north, the lower part is south and the right part is east. For each presented stage, there are two graphs. On both, each line segment represents a Conduit and at every line junction there is a Junction.

The left graph shows the water flow. The width of each line is proportional to the flow through the corresponding conduit (and a small constant is added so that the dry conduits are also visible). In the strongly coloured parts the flow is pressurised, while partially filled conduits are painted in paler shades (the lower the water level, the paler the shade). The conduits through which the water flows in south or east direction are painted black (or grey) while the flow in the opposite direction is marked with red.

The emphasis of the right graph is on the conduit sizes. The width of each line is proportional to the diameter of the corresponding conduit, while the colour marks the growth rate. Deep blue colour means no growth, while warmer colours (through green and yellow up to orange and red) represent bigger growth rates.

The circles drawn around some junctions represent water inflows. The diameter of the circle is proportional to recharge.

In the first figure of an example, the boundary conditions are marked with a frame around the left graph. Black line means no flow into or out of the network, which is the default situation. Grey line means seepage face, free outflow. When a corner junction is adjoined by both black and grey lines, free outflow is implemented for it.

The legend of the symbols is presented in Tab. 5.1.

5.2.2 Network on a low dip plane

Uniform network, irregular inflows (example 21-35)

The modelled grid is square and all the conduits are 10 m long. It descends 1 m per node in east direction, while there is no slope in the north-south direction. The north, south and west faces are impermeable, while on east side the outflow is free. The free outflow is realised by connecting each Junction on the eastern face











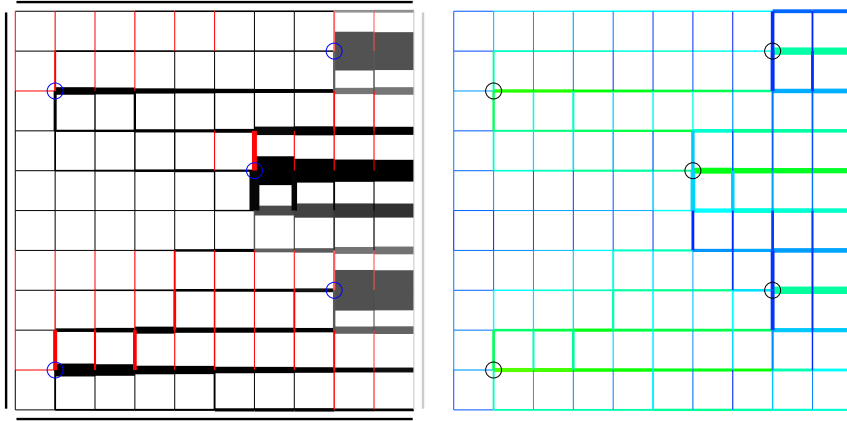
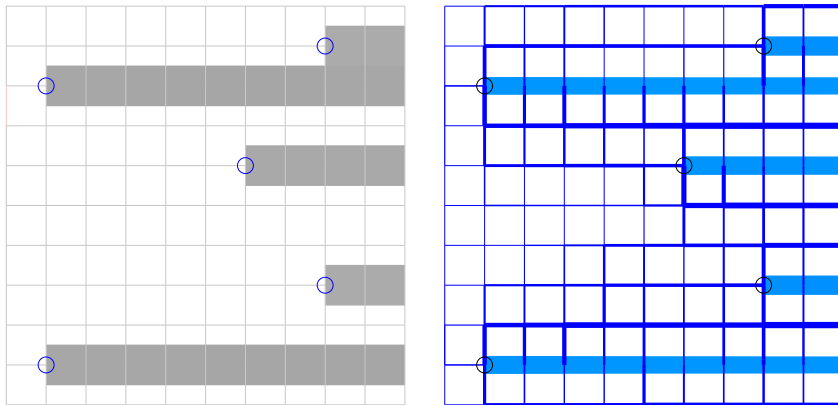
Flow (left) graphs	
	pressurised flow from west to east, the width is proportional to the flow rate
	pressurised flow from east to west
	pressurised flow from north to south
	free surface flow from south to north, the colour is paler for less full conduits
	inflow, the diameter is proportional to the flow rate
	watertight edge, no flow boundary condition, used as a part of the frame
	edge with a free outflow, water can leave the network freely
Conduit (right) graphs	
	N-S oriented conduit, line width is proportional to conduit width
	W-E oriented conduit, warmer colours mean higher enlargement rates and this conduit is not being enlarged at all
	N-S oriented conduit being enlarged swiftly

Table 5.1: The symbols used in the graphs of the networks. Different examples use different scales for the flow rates, inflow rates, conduit widths, and conduit growth rates, because the differences between examples are too big and do not allow the use of common scales.



(a) After 10 cycles = 3 000 s.



(b) After 50 cycles = 15 000 s.

Figure 5.2: Uniform network with irregular inflows (example 21-35). On the left graph, wider line means more flow, paler line means less full conduit and red line means flow in north or west direction. On the right graph, wider line means wider conduit and warmer colour means higher rate of widening. The frame of the top left graph shows boundary conditions: black line means no flow while grey line means seepage face, free outflow. Circles denote recharge points. The diameter of each one is proportional to the recharge rate.

to an Outfall object by a 100 m long Conduit of 5 m diameter. The lower edges of these Conduits are at the inverts of the Junctions, while the other Conduits are initially positioned 100 m above the inverts. Initial diameter of all the Conduits in the network is 0.005 m. Maximum water depth at the Junctions is 120 m except for 5 of the Junctions where it is 111 m. At these 5 Junctions there are the only water inflows into the system and they are limited to 1 000 l/s each. The initial conditions are obtained by running the flow for 1 day. The model is run for 50 steps of 300 s, together 15 000 s.

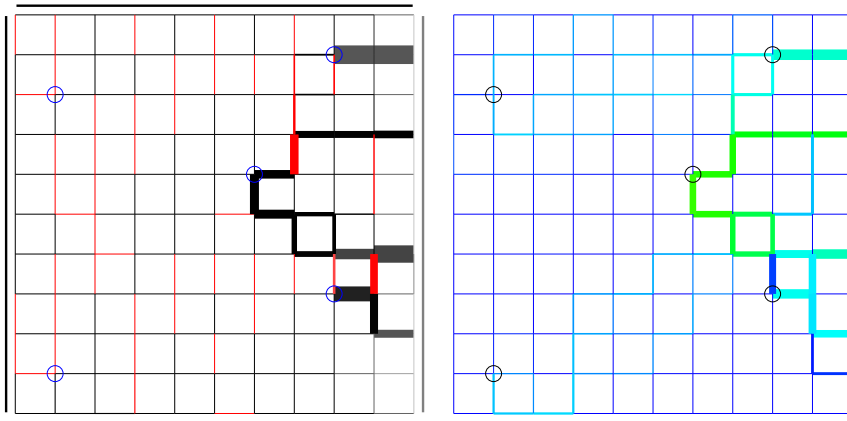
In nature, a situation vaguely corresponding to such a grid would be a sloping buried layer of soluble rock reaching the surface at the lower edge. There are five sinkholes above it which represent the only points for water to enter the aquifer.

The results are presented in Fig. 5.2. It can be seen that after 15 000 s of evolution all the water is flowing directly in the east direction from the inflow to the edge, there are no confluences. It comes as no surprise: at any time around majority of the junctions (maybe at every junction but a formal proof has not been sought), the hydraulic gradient away from the junction is largest in the conduit toward east. Initially all the conduits are of a same size so the outflow into the eastern conduit is higher than into the others. The conduit toward east thus grows fastest and its bottom is lowering fastest. Eventually the water level at the junction falls below the lower edges of the other conduits and the eastward one remains the only one draining it.

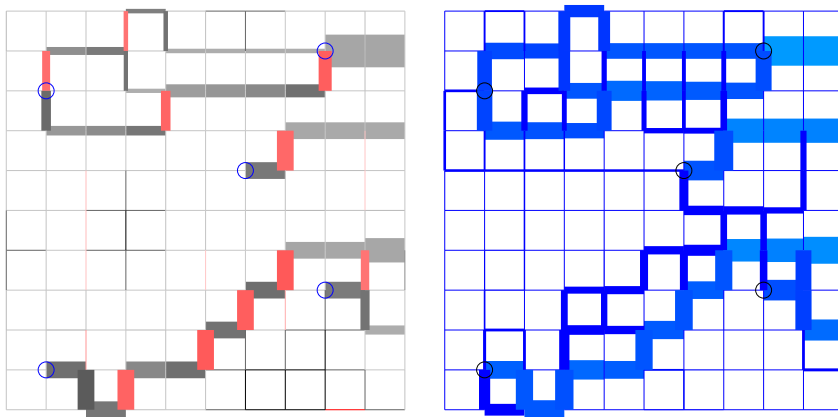
Non-uniform network, irregular inflows, small (example 21-137)

Everything is the same as in example 21-35 except for the diameters of the conduits. The diameters are random and uniformly distributed between 0.000 1 m and 0.01 m. In the results in Fig. 5.3 it can be seen that the irregularity in the initial diameters enables formation of a more complex conduit network than in the case of a uniform network (example 21-35). The resulting flow network tends to form a branchwork and the conduit network is a maze.

In this example, the flow as a function of time is also investigated. In the EPA-SWMM Report file in the Flow Routing Continuity section, the information on External Outflow can be found. The value represents all the water that has been conducted through the conduit network during the 300 s of simulation. The average flow rate during each cycle is obtained from it and the result is presented in Fig. 5.4. Initially the outflow is small because the small conduits do not allow much water to pass at the maximum head gradient allowed by the topography. Later on, the inflow from each recharge point is increasing in an exponential-like



(a) After 10 cycles = 3 000 s.



(b) After 50 cycles = 15 000 s.

Figure 5.3: Non-uniform network with irregular inflows (example 21-137). The explanation of the graphs is the same as in Fig. 5.2. It can be seen that the evolved conduit network (right graph) resembles a maze while the flow (left graph) is limited to a branchwork-like pattern.

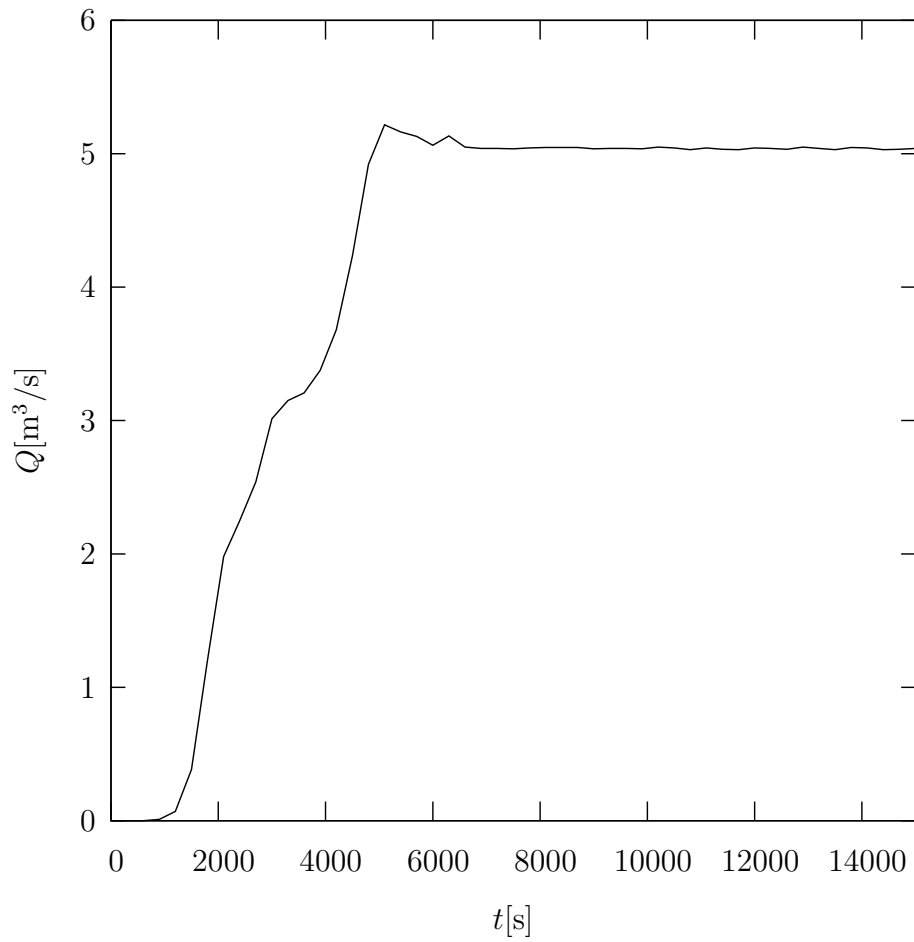
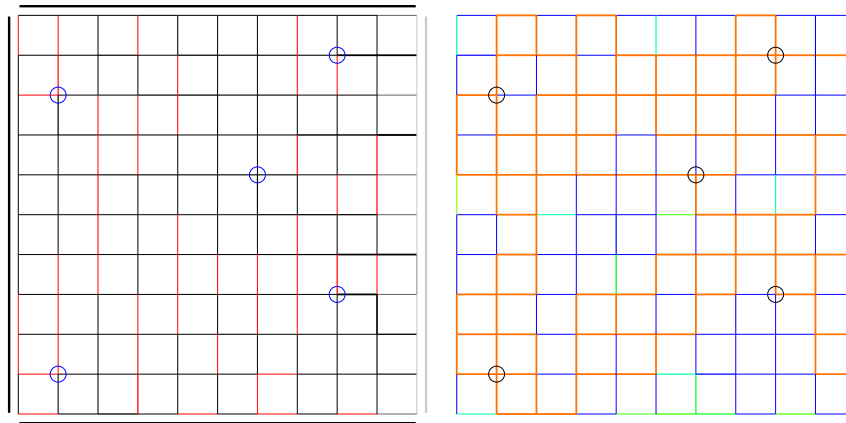


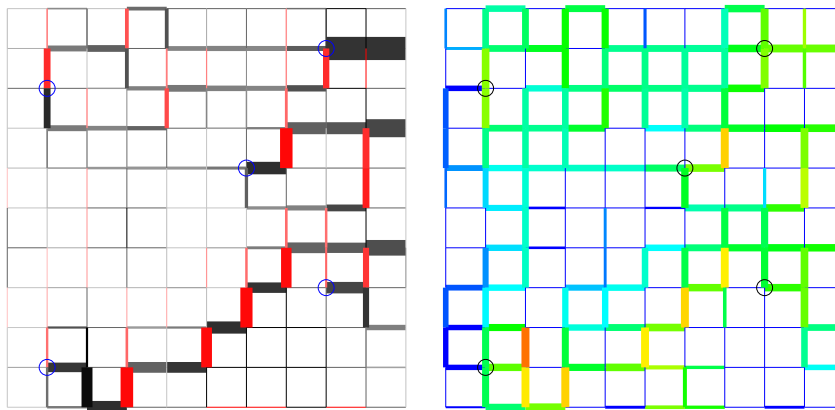
Figure 5.4: Outflow as a function of time in the case of a non-uniform network with irregular inflows (example 21-137). Initially it is small, then it grows irregularly because different recharge points reach their limits at different times. In the end it stabilizes around the total inflow of $5 \text{ m}^3/\text{s}$.

manner until the limit at $1 \text{ m}^3/\text{s}$ is reached and the increase stops. As the inflows reach their limits at different times, the outflow increase has “kinks” that appear at multiples of $1 \text{ m}^3/\text{s}$, the limit of a single recharge point. When all the inflow is drained through the conduit network, the outflow has a slight overshoot due to the stored water and then it stabilizes around the total inflow of $5 \text{ m}^3/\text{s}$.

Non-uniform network, irregular inflows, limestone (example 21-237)



(a) After 10 cycles = $3 \cdot 10^9 \text{ s} = 95 \text{ a}$.



(b) After 50 cycles = $1.5 \cdot 10^{10} \text{ s} = 475 \text{ a}$.

Figure 5.5: Non-uniform network with irregular inflows in limestone (example 21-237). The explanation of the graphs is the same as in Fig. 5.2. It can be seen that the evolved conduit network (right graph) is a more complex maze than in the salt case (Fig. 5.3) while the flow (left graph) is almost as limited to a branchwork-like pattern.

Everything is the same as in example 21-137 except for the dissolution kinetics and the timesteps. When calculating dissolution, α_s , c_{eq} , and D for limestone from

5.1.2 are used. As these parameters result in a much slower dissolution than in the case of salt, the modelled time has to be increased substantially.

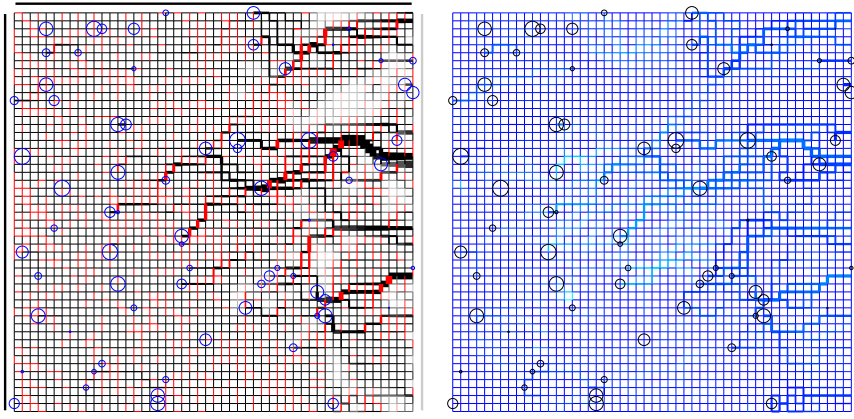
Lengthening the modelled time through increasing the number of timesteps would result in too long calculation times to be practical. If the timesteps were increased instead, it would not improve the situation. The reason is that the most time-consuming part of the calculation of each timestep is flow and pollutant routing with EPA-SWMM and computational time needed is proportional to the duration of the model timestep.

For this reason, routing and dissolution timesteps are decoupled. In each cycle, 300 s of routing is calculated, just like in the salt example (21-137). Dissolution in the same time is calculated. As the dissolution rates are small, the network does not change much in the time of one cycle. The dissolution rates in the next cycle are therefore almost the same and are not calculated again, the dissolution rates from the previous cycle are used instead. In this way, 10^6 cycles are lumped together before new dissolution rates are calculated. In the code it is accomplished with multiplying the effects of dissolution on widening of the conduits in a 300 s timestep by 10^6 and applying them to the network. In this way, effective dissolution timestep of $3 \cdot 10^8$ s is obtained without increase in calculation times.

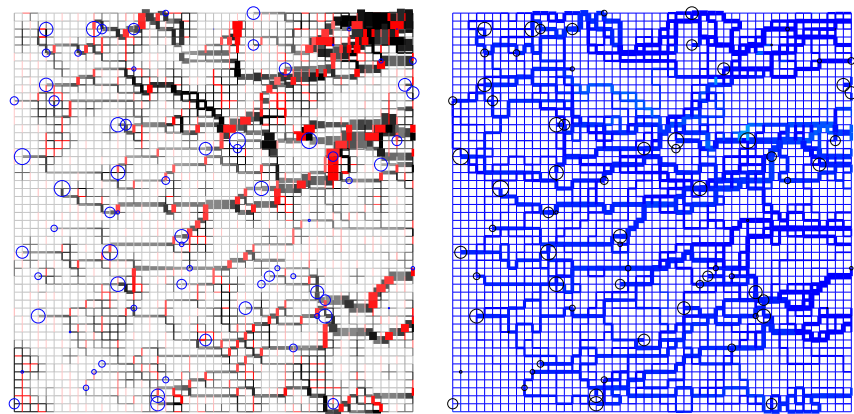
In the results in Fig. 5.5 it can be seen that initially the dissolution rates are similar in all the conduits that do have any flow. This is a consequence of dissolution rates being limited mainly by the surface reaction and slow: since $\alpha_D \gg \alpha_s$, $\alpha \approx \alpha_s$, and $c \ll c_{eq}$ for most conduits. Correspondence of this result to the situation in nature is questionable although it should be noted that the initial conduit size is relatively big and that the flow is already turbulent. In the later stages, enlargement of the conduits slows down when they are no longer fully flooded.

Non-uniform network, irregular inflows (example 21-52)

The modelled grid is square with 51×51 junctions and all the conduits are 10 m long. It descends 1 m per node in east direction, while there is no slope in the north-south direction. The north, south and west faces are impermeable, while on east side the outflow is free. The free outflow is realised by connecting each Junction on the eastern face to an Outfall object by a 100 m long Conduit of 5 m diameter. The lower edges of all Conduits are initially positioned 100 m above the inverts. Initial diameter of each of the Conduits in the network is a random number distributed uniformly between 0.000 1 m and 0.01 m. Maximum



(a) After 16 cycles = 4800 s.



(b) After 44 cycles = 13200 s.

Figure 5.6: Non-uniform network with irregular inflows on a larger scale (example 21-52). The explanation of the graphs is the same as in Fig. 5.2. Again, the evolved conduit network resembles a maze and the flow forms a branchwork-like pattern.

water depth at the Junctions is 220 m except for the Junctions with water inflows where it is 151 m. This ensures that no water can leave the system at Junctions that have no recharge and do not represent outflow nodes. For every Junction the probability of having an inflow is 0.025. Every inflow is a random number distributed uniformly between 0 and 1 000 l/s. The initial conditions are obtained by running the flow for 1 day. The model is run for 50 steps of 300 s, together 15 000 s. For calculating the water flow, full Saint Venant equations are solved as there are some flow instabilities. If the inertial terms were dropped, the obtained solution would in this case not be a good approximation of the correct solution, and the calculation would even take more time.

The results are presented in Fig. 5.6.

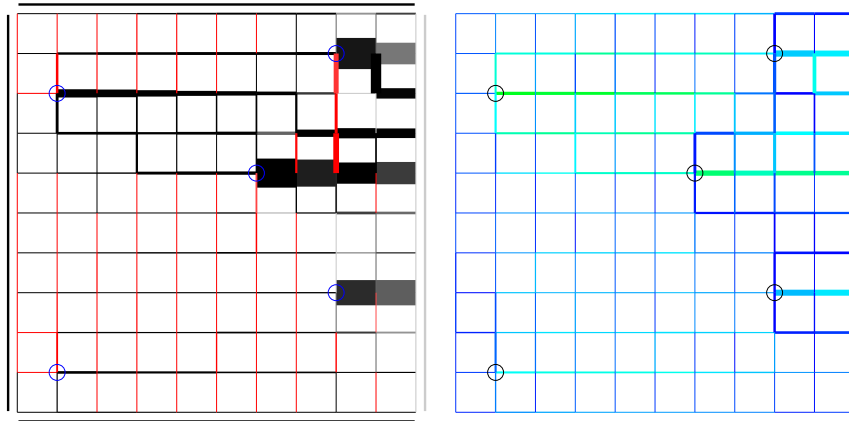
Uniform network, irregular inflows, conduits at different elevations (example 21-133)

The only difference between this example and example 21-35 is that in 21-133 the conduits' elevations are randomly scattered. Initial Inlet Offset and Outlet Offset of a chosen conduit take a random value between 99 and 101.

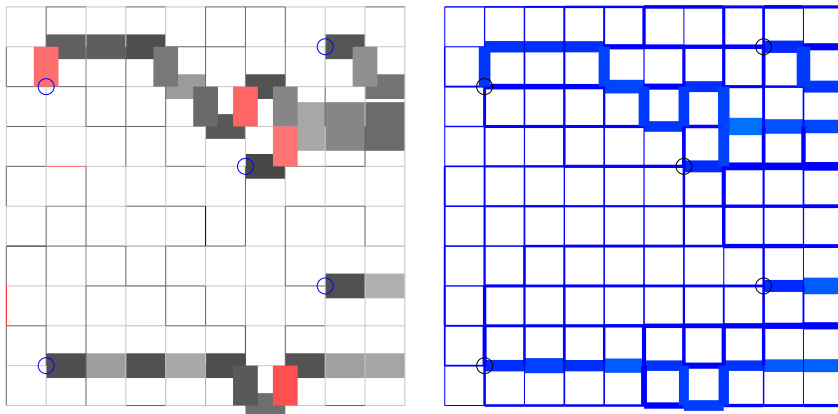
The results are presented in Fig. 5.7. While the initial development under phreatic conditions resembles the evolution of example 21-35, later on the situation changes and some branchwork formation does happen. The scattering in elevation of the conduits is sufficient to break the symmetry and enable non-trivial evolution.

Non-uniform network, irregular inflows, tilted sideways (example 21-337)

Everything is the same as in example 21-137 except that the network is also tilted sideways. It descends 0.3 m per node in south direction. The purpose of the calculation was to check if aligning the slope with the direction of the conduits adversely affects our examples, which are already artificial enough given that the grids are perpendicular. The expected and desired result would be that the outcome is quantitatively different from the results of the example 21-137 to show that the model does respond to small changes in the slope direction. At the same time, we would like both results to be qualitatively similar as a proof that the set of the examples with the grid and the slope parallel is not too limited in behaviour compared to more general cases. The resulting conduits and flow routes, presented in Fig. 5.8, confirm our expectations.

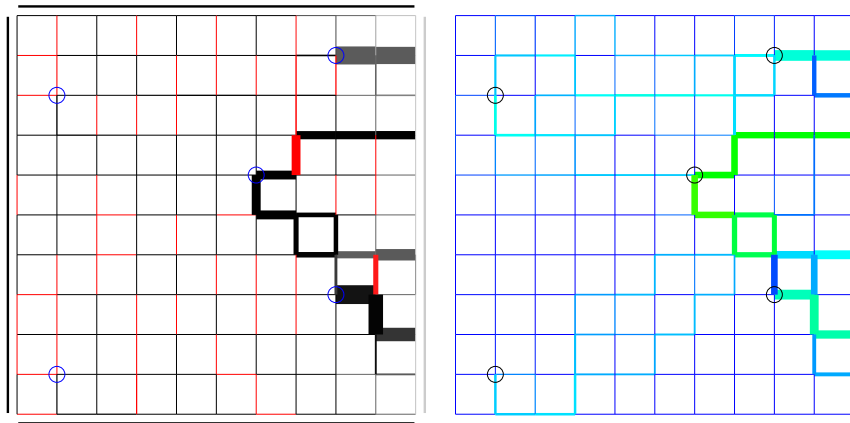


(a) After 8 cycles = 2400 s.

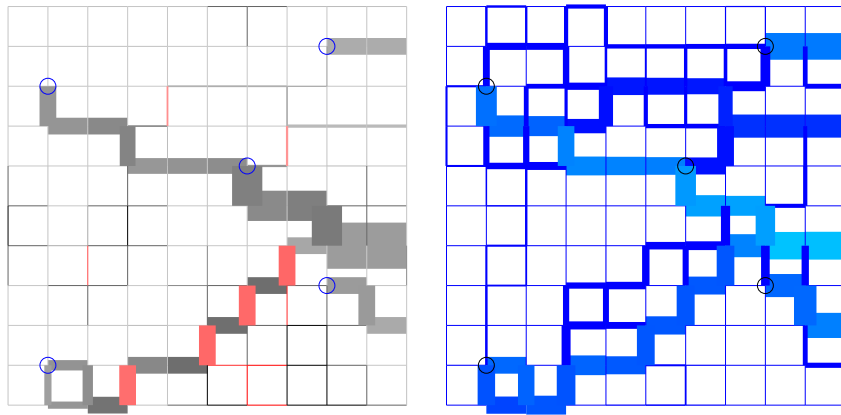


(b) After 50 cycles = 15000 s.

Figure 5.7: Uniform network with irregular inflows and conduits at different elevations (example 21-133). The explanation of the graphs is the same as in Fig. 5.2. Initially the results resemble the ones for uniform network with irregular inflows and conduits not scattered in elevation, while later on some concentration of the flow does happen.



(a) After 10 cycles = 3 000 s.



(b) After 50 cycles = 15 000 s.

Figure 5.8: Non-uniform network with irregular inflows tilted also to the side (example 21-337). The explanation of the graphs is the same as in Fig. 5.2.

Non-uniform network, irregular inflows, pulsed recharge (example 21-437)

Everything is the same as in example 21-137 except for the recharge. Instead of constant recharge of 1 000 l/s in every inflow, the recharge is 3 000 l/s in one cycle and then 500 l/s for the next 4 cycles. The average recharge is thus kept the same. The initial condition is calculated with inflows of 500 l/s for 1 day, 3 000 l/s inflows are introduced in the first cycle of dissolution.

The results in Fig. 5.9 are somewhat different from the constant recharge results. At the same time, both results are similar, the differences are modest. This indicates that modelling of network evolution at transient recharge conditions is possible with the tools we have developed.

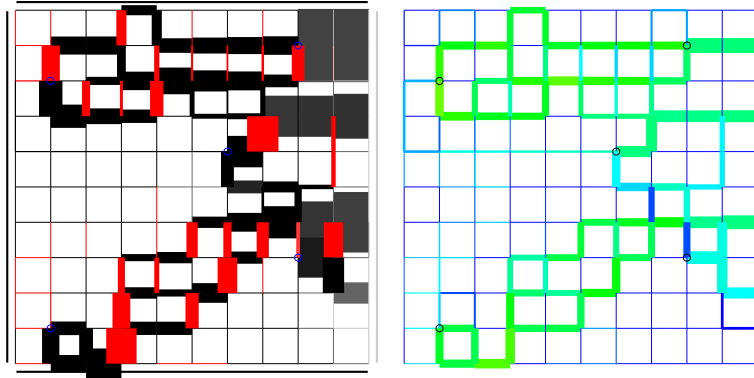
5.2.3 Networks as vertical cross-sections through aquifers

Uniform network, uniform inflow (example 21-15)

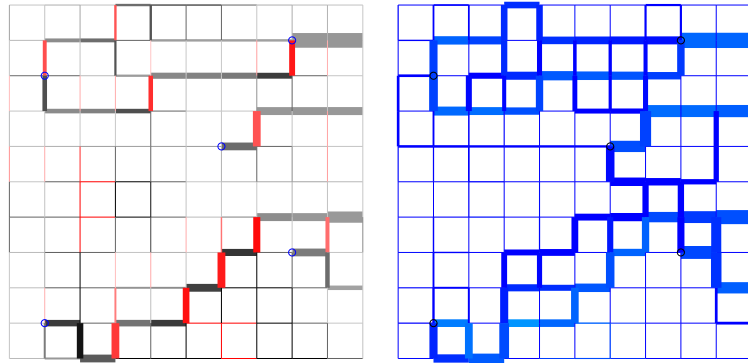
In the modelled grid, every conduit is 10 m long. It descends 1 m per node in east direction, while with every step south it descends 9.9 m. The cross-section can thus be thought of as a vertical or nearly vertical one. The invert of the Junction at the southeastern corner is at elevation 0. The maximum water depth at every Junction is prescribed so that the maximum head is 220 m. The north, south and west faces are impermeable, while on east side the outflow is free. The free outflow is realised by connecting each Junction on the eastern face to an Outfall object by a 100 m long Conduit of 5 m diameter. The lower edges of these Conduits are at the inverts of the Junctions, while the other north-south Conduits are initially positioned 99 m above the inverts and east-west conduits 100 m above the inverts. The difference in elevation of the Conduits is meant to make sure that water preferentially flows in the direction of the bigger gradient, that is toward south (see Fig. 2.3). Only if the sub-vertical south-leading Conduit is full and the water level at the Junction rises above it, water can start flowing into sub-horizontal conduits.

Initial diameter of all the Conduits in the network is 0.0005 m. At every node along the northern face there is a water inflow limited to 5 l/s. The initial conditions are obtained by running the flow for 1 day. The model is run for 50 steps of 300 s, together 15 000 s.

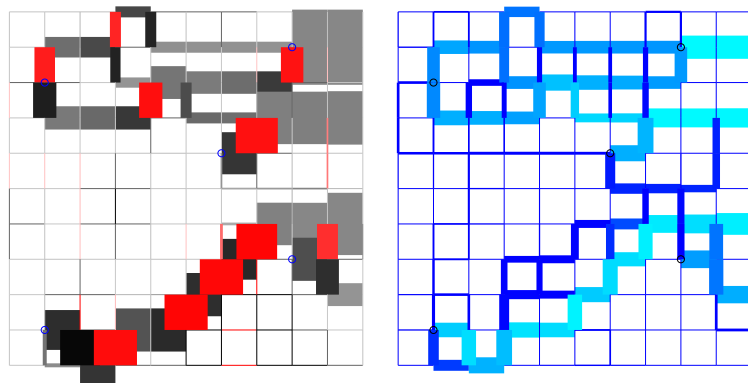
The inspiration for modelling such a network from nature is a vertical cross-section through a massif. There are conduits that are nearly vertical and others that are nearly horizontal, one side and the bottom are impermeable, one side is



(a) After 21 cycles = 6 300 s (at high recharge).

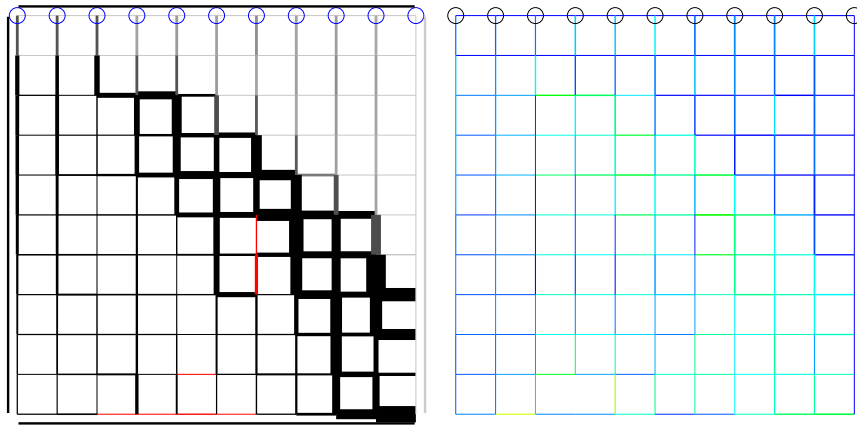


(b) After 22 cycles = 6 600 s (at low recharge).

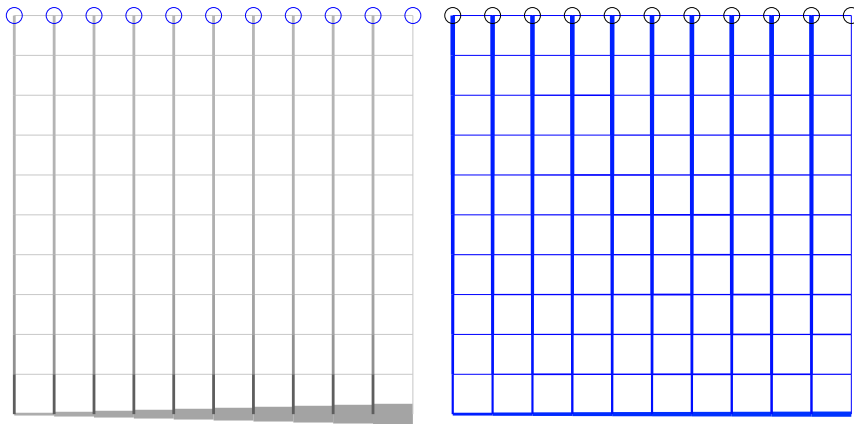


(c) After 46 cycles = 13 800 s (at high recharge).

Figure 5.9: Non-uniform network with irregular pulsed inflows (example 21-437). The explanation of the graphs is the same as in Fig. 5.2.



(a) After 5 cycles = 1500 s.



(b) After 50 cycles = 15000 s.

Figure 5.10: Vertical uniform network with uniform inflow (example 21-15). The explanation of the graphs is the same as in Fig. 5.2.

open and on the top there is precipitation.

The results are presented in Fig. 5.10. The water level starts falling from the open face into the massif, in the vadose zone the water flow is vertical and in the end there is a water table cave at the southern edge and water reaching it in vertical direction.

Drop of the water table in unconfined aquifers has also been modelled by Dreybrodt et al. [11]. Similar results have been achieved.

Non-uniform network with one large conduit, point inflow (example 21-8)

The diameters of most of the conduits are determined in a statistical way but not independently for each conduit. We try to model stronger and weaker discontinuities so that the diameter of each conduit is influenced by the line it lies in. In order to achieve this, the conduits forming a straight line are grouped together. The diameter of each of the conduits is a sum of group contribution and eventual individual contribution. The group contribution is the same for each conduit in a given group. It is a random number between 0 and 0.005 m. Every group has 0.5 probability that its conduits also get individual contribution. In this case, it is calculated individually for each conduit of the group and is a random number between 0 and 0.01 m.

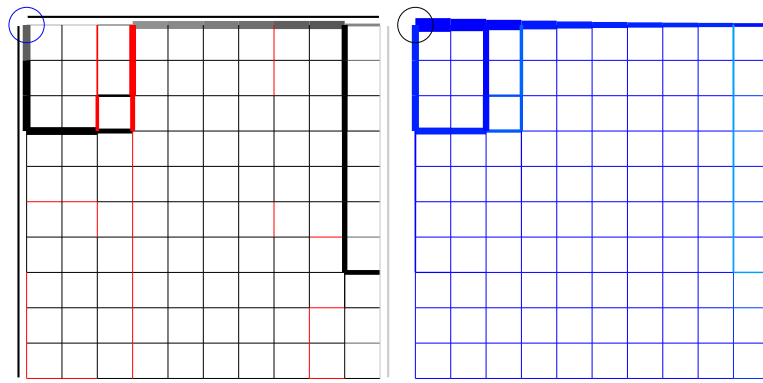
Initial diameter of the topmost horizontal conduit is 0.1 m. At the north-western junction there is an inflow limited to 100 l/s. The initial conditions are obtained by running the flow for 1 day. The model is run for 1500 steps of 300 s, together 450 000 s.

The model is meant to reproduce evolution of drawdown vadose passages. At first a water table cave forms at the northern side of the network and percolation toward south is small. When the southern conduits are enlarged, the water table is drawn down and the northern conduits stay dry. The process repeats itself. The results are presented in Fig. 5.11.

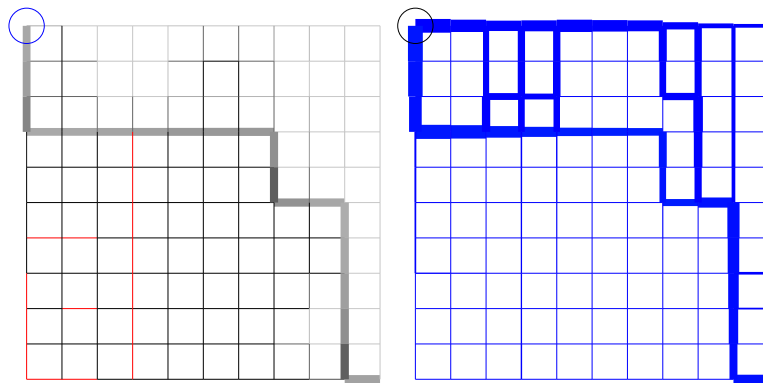
The setting in this example is similar to the one in Figure 5.5 and some others in Dreybrodt et al. [11]. In both models, development of big conduits causes the conduits above them to lose their recharge.

Non-uniform network with two large conduits and two point inflows (example 21-25)

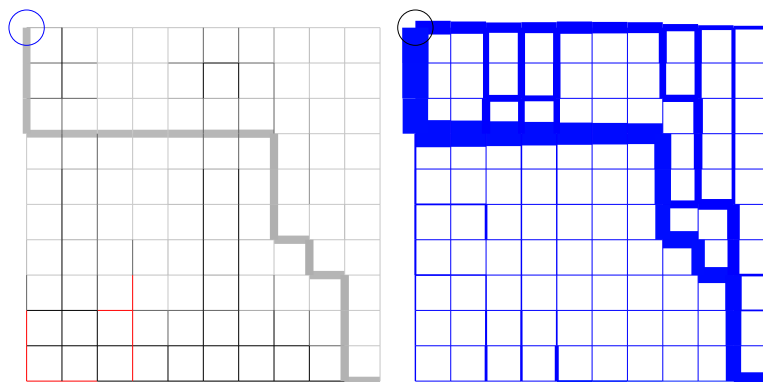
Just in the example 21-8, the initial diameter of the conduit along the northern edge is 0.1 m and at the north-western junction there is an inflow limited to



(a) After 450 cycles = 135 000 s.

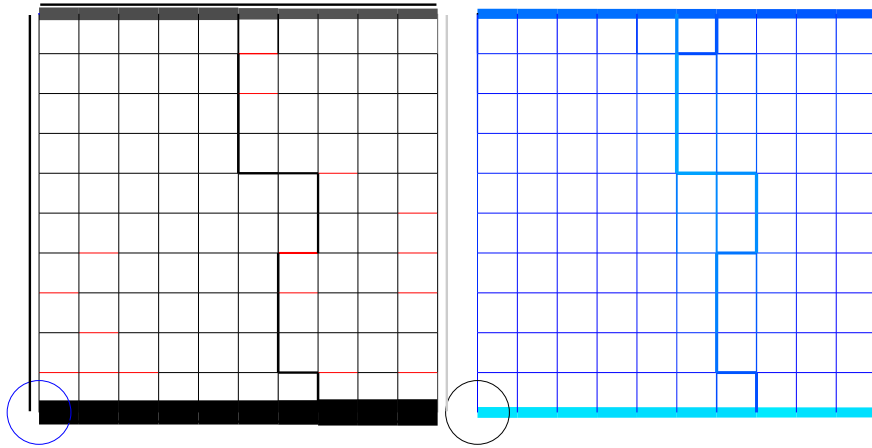


(b) After 750 cycles = 225 000 s.

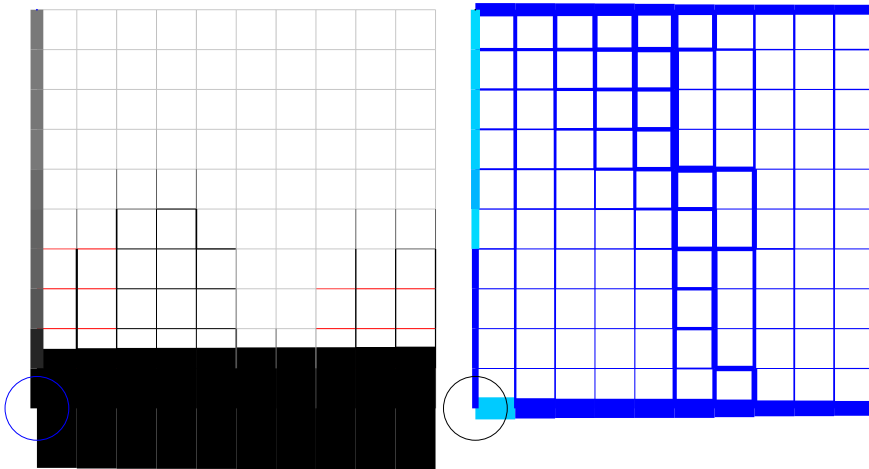


(c) After 1500 cycles = 450 000 s.

Figure 5.11: Vertical non-uniform network with one large conduit (example 21-8). The explanation of the graphs is the same as in Fig. 5.2. The diameter of the biggest conduit in (c) is 2.56 m.



(a) After 8 cycles = 960 s.



(b) After 20 cycles = 2400 s.

Figure 5.12: Vertical non-uniform network with two large conduits and two point inflows (example 21-25). The explanation of the graphs is the same as in Fig. 5.2. As the inflow limit at the north-western junction is two orders of magnitude smaller than the south-western one, the same is true for the circle labelling it, which is thus small.

100 l/s. There is also a conduit of 0.1 m diameter along the southern edge and an inflow at the south-western junction meant to be unlimited and implemented as an inflow limited to 10 000 l/s. The other conduits have initial diameter of 0.005 m, except for one of the possible connections between northern and southern conduit whose initial diameter is 0.02 m. The initial conditions are obtained by running the flow for 1 day. The model is run for 50 steps of 120 s, together 6 000 s.

The results are presented in Fig. 5.12. The northern conduit is being enlarged until the water escapes into the southern conduit, firstly through the initially bigger connection and then further upstream. The southern conduit is pressurised and growing continuously.

Network of linked wells (example 21-30)

In this example, there are three wells of initial diameter 0.2 m extending from the northern to the southern edge. There are 5 conduits of initial diameter 0.005 m extending from the western to the eastern edge connecting the wells between them and to the outlets. The other conduits are of negligible diameter 10^{-5} m. The recharge is through three inflows of 100 l/s each at the northern end of each well. The model is run for 50 steps of 60 s, together 3 000 s.

The results are presented in Fig. 5.13. At first, the eastern well which is closest to the outflow boundary develops fastest as the head gradients away from it are large. As a result of the enlargement of the downstream conduits, the heads in the well fall and it turns into a vadose shaft. From there on, it represents an outfall boundary for the conduits leading from the central well. The same story hence repeats with the central and later on with the western well.

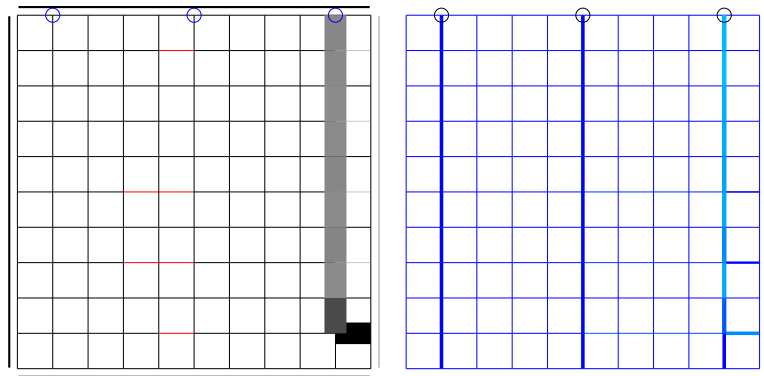
It has been recognized that deep caves tend to occur near the edges of karst plateaux [16]. Possibly the high hydraulic gradients in such areas that in the model favour the evolution of the shaft nearest to the edge also give rise to them.

5.2.4 Discussion

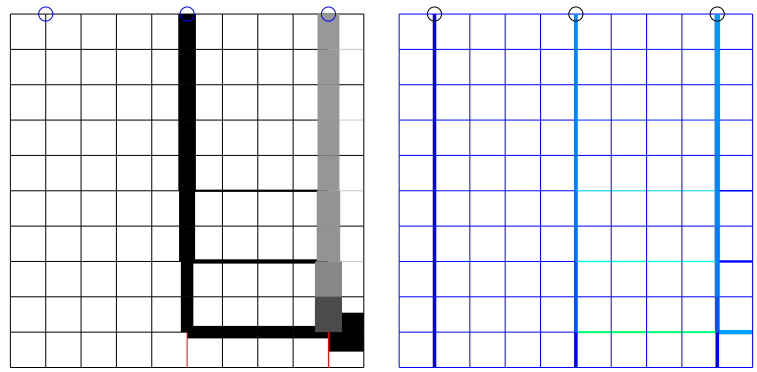
The trivial results for the uniform networks make one think that randomness of the initial situation may be an important factor in speleogenesis.

In the case of a low dip network, the expected result would typically be a branchwork or a maze cave. Most of the results obtained are hybrids, maze caves with branchwork flow patterns. It indicates that conduit networks may evolve from a maze to a branchwork stage, at least when limited to a single layer.

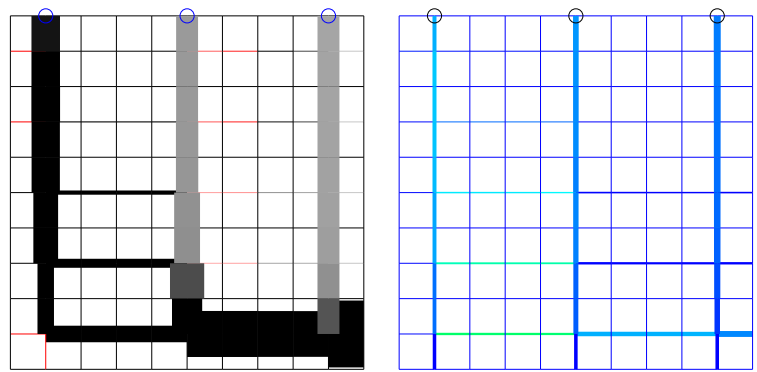
The vertical non-uniform networks are meant to reproduce vertical develop-



(a) After 8 cycles = 480 s.



(b) After 15 cycles = 900 s.



(c) After 27 cycles = 1 620 s.

Figure 5.13: Vertical network of linked wells (example 21-30). The explanation of the graphs is the same as in Fig. 5.2.

ment and formation of drawdown vadose passages. As far as we can tell their evolution is modelled successfully.

Chapter 6

Discussion of the results

The presented examples show that currently available basic knowledge, computer hardware and software allow us to model speleogenesis under free surface turbulent flow conditions. Both evolution of conduit networks in karst aquifers and evolution of shapes of particular conduits can be investigated with the models developed. In addition to steady-state recharge conditions, transient flow can be modelled.

The results we have obtained are similar to what one would expect, they mostly do not oppose the conceptual ideas on speleogenesis we already had before. This absence of surprising findings was to be expected because we have begun working on a new field. We have looked at only a small part of the available parameter space. The general agreement between the results and the expectations also strengthens our opinion that the model is generally good. If these first results were too spectacular, it would with a high probability indicate a mistake in the model.

An open question in speleogenesis that we did touch is, at which stage is it determined which conduits will be enlarged further and which ones will stay small and be abandoned. There are many initial fractures but only a few of them develop into big conduits and cave passages. Is the choice “made” already in the phreatic phase or can it be changed later in the vadose phase? Some of the examples illustrate this subject. The example 21-35, Fig. 5.2, is the control case. The inflow locations are the only thing that can influence which of the conduits are enlarged, everything else is uniform. The examples 21-137 and 21-133 are both similar to 21-35 but with a crucial difference. 21-137 is heterogeneous from the beginning. Water is choosing its way based on conduit diameters and conductivities and a relatively complex conduit network results. In 21-133 the symmetry is broken at the onset of free surface flow conditions so all the difference between

21-133 and 21-35 arises after the phreatic-vadose transition. The difference is quite obvious while the network developed in 21-133 is not nearly as complex as the one in 21-137. It looks like both phreatic and vadose phase can be important.

In most of the networks representing a shallow plane, the flow ends up being concentrated in a pattern resembling a branchwork. If the model run was extended, only the branchwork of the conduits would be being enlarged and sooner or later we would say that the shape of the resulting cave is strongly determined by the free surface phase. However, it should be noted that only one plane is modelled. In a 3D setting, the flow would sooner or later shift to a lower plane and cease developing the cave, which cannot happen in our models. In principle there are no obstacles toward building a model of a 3D network with the tools presented. We have not attempted it because there are plenty of questions waiting to be answered that do not demand it. At the same time, the post-processing and presentation of 3D results would have presented a challenge to us.

Another way to go on from these models is including the effects of sediment transport, sediment deposition and abrasion by the sediments. It would sure make evolution of conduits and networks more interesting. Inflowing sediment would for example obviously heavily influence the outcome of example 3 in Sec. 4.1.

The karst community is mostly interested in limestone caves while the results presented are mostly valid for salt due to the complexity of limestone dissolution. Building a suitable model of limestone dissolution on the level of chemical kinetics and including it into the speleogenesis model would be of interest too.

The source codes, input files and results are supplied on a CD. The main reason for including the CD are animations that present a chosen case and its development much better than the few graphs that can be put on paper.

Bibliography

- [1] William K. Annable and Edward A. Sudicky. “Simulation of karst genesis: hydrodynamic and geochemical rock-water interactions in partially-filled conduits”. In: *Bulletin d’Hydrogeologie* 16 (1998), pp. 211–221.
- [2] J. Banaszek et al. *Advanced Numerical Techniques in Energy Transfer*. Gliwice: Silesian University of Technology, Institute of Thermal Technology, 2004.
- [3] J. Bear and A. Verruijt. *Modeling Groundwater Flow and Pollution*. Dordrecht: D. Reidel Publishing Company, 1994.
- [4] Matt D. Covington et al. “Process length scales and longitudinal damping in karst conduits”. In: *Journal of Geophysical Research* 117 (1 2012).
- [5] S. Lawrence Dingman. *Physical Hydrology*. New York: Macmillan Publishing Company, 1993.
- [6] Wolfgang Dreybrodt. “Principles of early development of karst conduits under natural and man-made conditions revealed by mathematical analysis of numerical models”. In: *Water Resources Research* 32.9 (1996), pp. 2923–2935.
- [7] Wolfgang Dreybrodt. *Processes in karst systems: physics, chemistry, and geology*. Springer series in physical environment. Springer, 1988.
- [8] Wolfgang Dreybrodt. “The kinetics of calcite dissolution and its consequences to karst evolution from the initial to the mature state”. In: *NSS Bulletin* 49 (1987), pp. 31–49.
- [9] Wolfgang Dreybrodt and Dieter Buhmann. “A mass transfer model for dissolution and precipitation of calcite from solutions in turbulent motion”. In: *Chemical Geology* 90 (1991), 107–122.
- [10] Wolfgang Dreybrodt and Franci Gabrovšek. “Speleogenesis: computer models.” In: *Encyclopedia of caves and karst science*. Ed. by John Gunn. New York, London: Fitzroy Dearborn, 2004, pp. 677–681.

- [11] Wolfgang Dreybrodt et al. *Processes of speleogenesis: a modeling approach*. Carsologica Series. Založba ZRC, 2005.
- [12] Malcolm S. Field. *A lexicon of cave and karst terminology with special reference to environmental karst hydrology*. Washington, D.C. 20460: National Center for Environmental Assessment–Washington Office, Office of Research and Development, U.S. Environmental Protection Agency, 2002.
- [13] Derek C. Ford and Paul W. Williams. *Karst hydrogeology and geomorphology*. John Wiley & Sons, 2007.
- [14] Andrew Fowler. *Mathematical Geoscience (Interdisciplinary Applied Mathematics)*. 1st Edition. Springer, 2011.
- [15] Franci Gabrovšek. “Dynamics and patterns of karst aquifer evolution: a modelling perspective”. In: *Carbonate Geochemistry: Reactions and Processes in Aquifers and Reservoirs*. Ed. by Annette Summers Engel et al. Vol. 16. Special Publication. Billings, Montana: Karst Waters Institute, 2011, pp. 23–26.
- [16] Franci Gabrovšek. “Two of the world’s deepest shafts on Kaninski podi plateau in western Julian Alps, Slovenia”. In: *Proceedings of the 12th International Congress of Speleology*. Ed. by Pierre-Yves Jeannin. Basel: Swiss Speleological Society (SSS/SGH): Speleo Projects, 1997, pp. 23–24.
- [17] Franci Gabrovšek and Wolfgang Dreybrodt. “A model of the early evolution of karst aquifers in limestone in the dimensions of length and depth”. In: *Journal of Hydrology* 204 (2001), pp. 206–224.
- [18] Christopher G. Groves and Alan D. Howard. “Early development of karst systems. 1. Preferential flow path enlargement under laminar-flow.” In: *Water Resources Research* 30.10 (1994), pp. 2837–2846.
- [19] R. Blair Hanna and Harihar Rajaram. “Influence of aperture variability on dissolutional growth of fissures in karst formations”. In: *Water Resources Research* 34.11 (1998), pp. 2843–2853.
- [20] Ph. Häuselmann, P. Y. Jeannin, and M. Monbaron. “Role of epiphreatic flow and soutirages in conduit morphogenesis: the Bärenschacht example (BE, Switzerland)”. In: *Zeitschrift für Geomorphologie, NF* 47.2 (Jan. 2003), 171190.

- [21] A. A. Jeschke, K. Vosbeck, and Wolfgang Dreybrodt. “Surface controlled dissolution rates of gypsum in aqueous solutions exhibit nonlinear dissolution kinetics”. In: *Geochimica et Cosmochimica Acta* 65.1 (2001), pp. 27–34.
- [22] Georg Kaufmann. “Karst aquifer evolution in a changing water-table environment”. In: *Water Resources Research* 38.6 (2002).
- [23] Georg Kaufmann and Jean Braun. “Karst aquifer evolution in fractured, porous rocks”. In: *Water Resources Research* 36.6 (2000), pp. 1381–1391.
- [24] Georg Kaufmann and Jean Braun. “Karst aquifer evolution in fractured rocks”. In: *Water Resources Research* 35.11 (1999), pp. 3223–3238.
- [25] Georg Kaufmann and Wolfgang Dreybrodt. “Calcite dissolution kinetics in the system $\text{CaCO}_3\text{--H}_2\text{O--CO}_2$ at high undersaturation”. In: *Geochimica et Cosmochimica Acta* 71 (2007), 1398–1410.
- [26] Georg Kaufmann, Douchko Romanov, and Wolfgang Dreybrodt. “Modeling of karst aquifers”. In: *Encyclopedia of caves. 2nd ed.* Ed. by William Blaine White and David C. Culver. Amsterdam: Academic Press, 2012, pp. 508–512.
- [27] Georg Kaufmann, Douchko Romanov, and Thomas Hiller. “Modeling three-dimensional karst aquifer evolution using different matrix-flow contributions”. In: *Journal of Hydrology* 388 (2010), pp. 241–250.
- [28] Attila Kovács. *Geometry and hydraulic parameters of karst aquifers: a hydrodynamic modeling approach*. Neuchâtel: Université de Neuchâtel, 2003.
- [29] N. I. Koškin and M. G. Širkevič. *Priročnik elementarne fizike*. Ljubljana: Tehniška založba Slovenije, 1986.
- [30] Rudolf Liedl et al. “Simulation of the development of karst aquifers using a coupled continuum pipe flow model”. In: *Water Resources Research* 39.3 (2003), pp. 1057–1067.
- [31] Mahmoud F. Maghrebi and Majid Rahimpour. “A simple model for estimation of dimensionless isovel contours in open channels”. In: *Flow Measurement and Instrumentation* 16 (2005), 347 – 352.
- [32] Arthur N. Palmer. “Origin and morphology of limestone caves”. In: *Geological Society of America Bulletin* 103 (1991), pp. 1–21.
- [33] Rodrigo Riquelme et al. “Interferometric measurement of a diffusion coefficient: comparison of two methods and uncertainty analysis”. In: *Journal of Physics D: Applied Physics* 40.9 (2007), pp. 2769–2776.

- [34] Lewis A. Rossman. *Storm Water Management Model Quality Assurance Report: Dynamic Wave Flow Routing*. Cincinnati, OH 45268: National Risk Management Research Laboratory, Office of Research and Development, U.S. Environmental Protection Agency, 2006.
- [35] Lewis A. Rossman. *Storm Water Management Model User's Manual Version 5.0*. Cincinnati, OH 45268: National Risk Management Research Laboratory, Office of Research and Development, U.S. Environmental Protection Agency, 2009.
- [36] H. Schlichting and K. Gersten. *Boundary-layer theory*. Physics and astronomy. Springer, 2000.
- [37] Jörg Siemers and Wolfgang Dreybrodt. “Early development of karst aquifers on percolation networks of fractures in limestone”. In: *Water Resources Research* 34.3 (1998), pp. 409–419.
- [38] Stephen R. H. Worthington. “A comprehensive strategy for understanding flow in carbonate aquifers”. In: *Karst Modelling*. Ed. by Arthur N. Palmer, Margaret V. Palmer, and Ira D. Sasowsky. Vol. 5. Special Publication. Charlottesville, Virginia: Karst Waters Institute, 1999, pp. 30–37.

Appendix A

Calculating transport of water
from a conduit to the porous
matrix by boundary distributed
source method



Contents lists available at SciVerse ScienceDirect

Engineering Analysis with Boundary Elements

journal homepage: www.elsevier.com/locate/enganabound

Calculating transport of water from a conduit to the porous matrix by boundary distributed source method

Matija Perne^{a,b,*}, Božidar Šarler^c, Franci Gabrovšek^a

^a Karst Research Institute ZRC SAZU, Titov trg 2, SI-6230 Postojna, Slovenia

^b Department of Systems and Control, Jožef Stefan Institute, Jamova 39, SI-1000 Ljubljana, Slovenia

^c Laboratory for Multiphase Processes, University of Nova Gorica, Vipavska 13, SI-5000 Nova Gorica, Slovenia

ARTICLE INFO

Article history:
Received 9 January 2012
Accepted 4 June 2012
Available online 5 July 2012

Keywords:
Karst aquifer
Darcy flow
Stefan problem
Moving and free boundary problems
Method of fundamental solutions
Boundary distributed source method

ABSTRACT

This study presents the development of a suitable numerical method for porous media flow with free and moving boundary (Stefan) problems arising in systems with wetted and unwetted regions of porous media. A non-singular version of the method of fundamental solutions (MFS), termed the boundary distributed source method (BDS), is applied. Darcy flow and homogenous isotropic porous media is assumed. The solution is represented in terms of the fundamental solution of the Laplace equation in two-dimensional Cartesian coordinates. The desingularisation is achieved through boundary distributed sources of the fundamental solution and indirect calculation of the derivatives of the fundamental solution. Respectively, the artificial boundary, characteristic for the classical, singular MFS is not present. The novel BDS is compared with the MFS and the analytical solutions for several numerical examples with excellent agreement. A sensitivity study of the solution, regarding the discretization and the free parameters is performed. The main contributions of the study are the application of the BDS to free and moving boundary problems and the comparison of BDS with MFS for these types of problems. The developed model can be applied to various geohydrological problems.

© 2012 Elsevier Ltd. All rights reserved.

1. Introduction

The exchange of flow and solutes between the conduits and the surrounding matrix plays an important role in many engineering and geohydrological problems [1]. A related example are karst aquifers, where the conduits are usually embedded into a fractured-porous medium. There, the storage and the transport of potential pollutants through the aquifer depends on the exchange processes between the potentially polluted conduits and the matrix [2,3]. It is therefore of importance to understand the dynamics of these exchange processes and to consider them in realistic models of karst aquifer.

The analytical solutions of such models can be obtained only for very limited, geometrically simple, linear 2D cases [4,5].

Different coupled continuum pipe-flow models have been used in the past to numerically model flow and solute transport in karst aquifers. These models rely on a finite difference method (FDM) [6,7] or finite element method (FEM) [8,9] discretisation scheme. They have successfully captured the dynamics of flow and transport in coupled conduit–matrix systems. In the case of unconfined aquifers one has to consider the presence of a water

table, a moving (transient character) boundary or free (steady character) boundary between the saturated and the unsaturated zone.

In cases when the mesh based methods, such as the FDM or FEM, are used for solving the above mentioned problems, various mesh refinement schemes are invoked to numerically account for a suitable determination of the position of the unfixed boundary. The principal bottleneck in these types of numerical methods is the time consuming re-meshing of the evolving water table and wetted/unwetted domains which limits such methods to problems with quite trivial geometrical patterns [10].

In order to build effective models for such situations, computationally new and efficient, meshfree modelling concepts [11–14] have to be considered.

Meshfree methods have proven to be very efficient in treating complex moving boundaries [15]. This work presents the use of such methods for a computational model of a conduit embedded in a matrix. It is focused on studying the exchange between a conduit and unconfined matrix due to a sudden change of pressure in the conduit. The method of fundamental solutions (MFS) and its non-singular version, termed the boundary distributed source (BDS) method proposed by Liu [16], are used to model a related moving boundary problem. Our objectives are demonstrating the use of BDS in problems related to groundwater flow, achieving advantages over classical numerical methods, and studying sensitivity of BDS to model parameters.

* Corresponding author at: Karst Research Institute ZRC SAZU, Titov trg 2, SI-6230 Postojna, Slovenia. Tel.: +386 41 242 333.

E-mail addresses: matija.perne@zrc-sazu.si (M. Perne), bozidar.sarler@ung.si (B. Šarler), gabrovsek@zrc-sazu.si (F. Gabrovšek).

MFS is a numerical technique that falls in the class of methods generally called boundary methods. The other well known representative of these methods is the boundary element method (BEM). Both methods are best applicable in situations where a fundamental solution to the partial differential equation under consideration is known. In such cases, the dimensionality of the discretisation is reduced. BEM for example requires polygonisation of the boundary surfaces in general 3D cases, and boundary curves in general 2D cases. This method requires solution of the complicated regular, weakly singular, strongly singular, and hypersingular integrals over boundary segments, which is usually a cumbersome and non-trivial task [17].

Both, BEM [18,19] and MFS [15,20], are well suited for unfixed boundary (Stefan) problems [21] due to the fact that only the boundary discretisation needs to be moved, without any connection with the domain discretisation.

A comprehensive survey of the MFS and related methods for elliptic boundary value problems and inverse problems can be found in [22,23]. The MFS has certain advantages over BEM, that are mostly visible in the fact that only pointisation of the boundary is needed, so that integral evaluations are completely avoided. Because of this there is no principal difference in coding between the 2D and the 3D cases. The principal drawback of MFS is the presence of an artificial boundary that needs to be constructed in cases with singular fundamental solutions (such as for example the fundamental solution of the Laplace equation) in order to allow the solution to comply with the boundary conditions. The MFS with an artificial boundary has been previously used in the context of transport of pollutants in porous media [24] and in the context of free surface flow [25].

The determination of the distance between the real boundary and the fictitious boundary is based on experience, by balancing between the increased accuracy and the increased ill-conditioning with the larger distance. Quite recently, various efforts have been made to remove this drawback of the MFS, so that the source points can be placed on the real boundary directly. Young et al. [26] were the first to propose placing of the source points on the boundary in the MFS. They proposed novel ways to directly determine the diagonal coefficients for simple geometries or use the results from the BEM, based on the fact that the MFS and the indirect boundary integral formulation are similar in nature. In their approach, the information of the neighbouring points before and after each source point is needed in order to form the line segments for integrating the kernels to obtain the diagonal coefficients. This is essentially the same information of the element connectivity as in a BEM mesh. Šarler [27] proposed a similar modified MFS, where the diagonal terms are determined by the integration of the singular or hypersingular fundamental solution on line segments, formed by using neighbouring points, and the use of a constant solution to determine the diagonal coefficients from the derivatives of the related fundamental solution. This first attempt has been followed by the formulation [16], where in order to remove the singularities of the fundamental solutions, the concentrated point sources are replaced by the distributed sources over areas (for 2D problems) or volumes (for 3D problems) covering the source points. The distributed sources, associated with the derivatives of the fundamental solution, have, however, been calculated as in [27]. Liu called his non-singular MFS approach BDS. The main objective of this paper is to solve the moving boundary problem, associated with the conduit and the porous matrix by the BDS and to compare it with the classical MFS and analytical solutions.

2. Governing equations

Throughout the paper we consider the porous matrix to be homogeneous and isotropic, neglect capillary and evaporation

effects, and consider only 2D solutions. Flow is assumed to follow Darcy law [28–33], and hydraulic conductivity or permeability of the fractured rock is constant and isotropic. The liquid-saturated part of the matrix is represented by a connected 2D domain Ω with boundary Γ . The medium is described by its hydraulic conductivity \tilde{K} and porosity ϕ . The problem is tackled in Cartesian coordinates $\tilde{\mathbf{p}} = \tilde{x}\mathbf{i}_x + \tilde{y}\mathbf{i}_y$, where \tilde{x} and \tilde{y} represent the Cartesian coordinates and \mathbf{i}_x and \mathbf{i}_y the base vectors. The gravity is directed toward $-\mathbf{i}_y$.

The quasi-steady state fluid flow in Ω is described by Darcy law

$$\tilde{\mathbf{q}} = -\tilde{K}\tilde{\nabla}\tilde{h}, \quad (1)$$

where $\tilde{\mathbf{q}}$ is flux and \tilde{h} the hydraulic head. A length scale l_0 is selected. Dimensionless coordinates are defined as $x = \tilde{x}/l_0$ and $y = \tilde{y}/l_0$, $\mathbf{p} = \tilde{\mathbf{p}}/l_0$. Dimensionless flux $\mathbf{q} = \tilde{K}^{-1}\tilde{\mathbf{q}}$ with $h = \tilde{h}/l_0$ are introduced in order that $\nabla = l_0\tilde{\nabla}$. Eq. (1) can afterwards be rewritten in dimensionless form

$$\mathbf{q} = -\nabla h. \quad (2)$$

Incompressibility is assumed and thus the specific storage in comparison with the specific yield is neglected. Incompressibility implies

$$\nabla \cdot \mathbf{q} = 0 \quad (3)$$

in the whole domain Ω . Eqs. (2) and (3) give the Laplace equation for the dimensionless hydraulic head in Ω

$$\nabla^2 h = 0. \quad (4)$$

The boundary is divided into three parts with Dirichlet, Neumann and free surface boundary conditions; i.e. $\Gamma = \Gamma^D \cup \Gamma^N \cup \Gamma^{FS}$ (see Fig. 1). On Γ^D there is a Dirichlet type of boundary condition. The hydraulic head is specified with the forcing function h^D ,

$$h(\mathbf{p}) = h^D(\mathbf{p}), \quad \mathbf{p} \in \Gamma^D. \quad (5)$$

On Γ^N there is a Neumann type of boundary condition. The hydraulic head gradient is specified with the forcing function q^N

$$\frac{\partial h}{\partial \mathbf{n}_r^N}(\mathbf{p}) = q^N(\mathbf{p}), \quad \mathbf{p} \in \Gamma^N, \quad (6)$$

where \mathbf{n}_r^N is the outward normal to the boundary Γ^N and $q^N(\mathbf{p})$ is the normal component of flow. For the Laplace equation, the liquid surface Γ^{FS} represents a special case of Dirichlet boundary condition. The free surface boundary condition is defined through

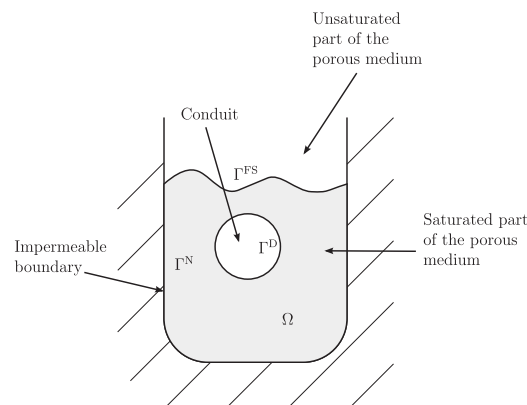


Fig. 1. Schematics of the problem domain and the boundary conditions.

the height

$$h(\mathbf{p}) = y(\mathbf{p}), \quad \mathbf{p} \in \Gamma^{\text{FS}}. \quad (7)$$

The liquid surface represents a moving boundary. The velocity of a point at the moving boundary is

$$\frac{\partial \mathbf{p}}{\partial t} = -\nabla h(\mathbf{p}), \quad \mathbf{p} \in \Gamma^{\text{FS}}, \quad (8)$$

where t is dimensionless time, $t = \tilde{t}\tilde{K}/(\phi l_0)$, and \tilde{t} is time. Eq. (8) can be projected onto the normal to the surface $\mathbf{n}_r^{\text{FS}} = n_x \mathbf{i}_x + n_y \mathbf{i}_y$

$$\mathbf{n}_r^{\text{FS}} \cdot \frac{\partial \mathbf{p}}{\partial t} = \mathbf{n}_r^{\text{FS}} \cdot (-\nabla h(\mathbf{p})). \quad (9)$$

The free surface is almost horizontal in all the calculated cases so n_x is much smaller than n_y and is neglected. The free surface is thus moved in every timestep according to equation

$$\frac{\partial y}{\partial t} = -\frac{\partial h}{\partial y}. \quad (10)$$

It is the purpose of the present work to calculate the hydraulic head (4) and the time evolution of the boundary Γ^{FS} as a function of the boundary conditions (5)–(10) and initial position of Γ^{FS} .

3. Solution procedure

3.1. Solution of the Laplace equation

3.1.1. Method of fundamental solutions

The MFS is based on the basic theory of partial differential equations (PDEs), stating that any linear combination of the solutions of a linear PDE is also a solution. The method belongs to the class of boundary meshless methods for solving various types of partial differential equations and has been increasingly applied in engineering since 1964 [34].

The solution is built as a linear combination of fundamental solutions of the Laplace equation $G_i(\mathbf{p})$. By definition, a fundamental solution, G_i solves the equation

$$\nabla^2 G_i = \delta(\mathbf{p}_i), \quad (11)$$

where

$$\nabla^2 = \frac{\partial^2}{\partial x^2} + \frac{\partial^2}{\partial y^2}$$

and $\delta(\mathbf{p})$ is Dirac delta function. The form of the fundamental solution is [16]

$$G_i(\mathbf{p}) = -\frac{1}{2\pi} \log(\|\mathbf{p} - \mathbf{p}_i\|),$$

$$\|\mathbf{p} - \mathbf{p}_i\| = \sqrt{(\mathbf{p} - \mathbf{p}_i) \cdot (\mathbf{p} - \mathbf{p}_i)}. \quad (12)$$

The solution is built as the sum

$$h(\mathbf{p}) \approx \sum_{i=1}^N G_i(\mathbf{p})c_i, \quad (13)$$

where N is the number of all fundamental solutions and c_i are the coefficients. Note that the positions of the singularities \mathbf{p}_i have to be outside $\Omega + \Gamma$ so that h solves the Laplace equation inside $\Omega + \Gamma$. The line that connects the singularities is called artificial boundary (Fig. 2). The coefficients are determined by collocating the boundary conditions. Each point with Dirichlet boundary condition gives an equation

$$\sum_{i=1}^N G_{ij}c_i = h_j,$$

$$G_{ij} = G_i(\mathbf{p}_j), \quad h_j = h^D(\mathbf{p}_j), \quad \mathbf{p}_j \in \Gamma^D. \quad (14)$$

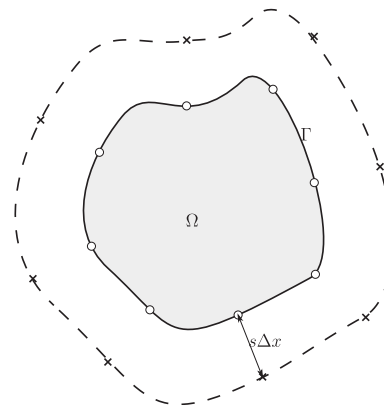


Fig. 2. Concept of MFS. Small white circles are collocation nodes with specified boundary condition, crosses are the fundamental solution singularities, and the dashed line is the artificial boundary $s\Delta x$ away from geometrical boundary.

In the case of Neumann boundary conditions, the row

$$\sum_{i=1}^N K_{ij}c_i = q_j,$$

$$K_{ij} = \frac{\partial G_i}{\partial \mathbf{n}}(\mathbf{p}_j) = -\frac{1}{2\pi} \frac{(\mathbf{p}_j - \mathbf{p}_i) \cdot \mathbf{n}}{\|\mathbf{p}_j - \mathbf{p}_i\|^2},$$

$$q_j = q^N(\mathbf{p}_j), \quad \mathbf{p}_j \in \Gamma^N \quad (15)$$

follows from every boundary point. Both sets of equations are solved together as one matrix equation. A square system of linear equations is assembled from the rows (14) and (15) for solution of N unknown coefficients c_i .

3.1.2. Boundary distributed source method

BDS method is conceptually similar to MFS, and the principal difference between both methods is in choice of the basis functions [16]. In MFS, the fundamental solutions are used as basis functions, while in BDS, the solutions for distributed area sources are used. The chosen shape of the source is a circle A of a radius r_0 with uniform source density of $1/(\pi r_0^2)$. The form of the solution is equal to the integral of the original fundamental solution G on A [16]

$$\hat{G}_i(\mathbf{p}) = \begin{cases} \frac{r_0^2}{2} \log\left(\frac{1}{\|\mathbf{p} - \mathbf{p}_i\|}\right) & \text{for } \|\mathbf{p} - \mathbf{p}_i\| > r_0, \\ \frac{r_0^2}{2} \log\left(\frac{1}{r_0}\right) + \frac{r_0^2 - \|\mathbf{p} - \mathbf{p}_i\|^2}{4} & \text{for } \|\mathbf{p} - \mathbf{p}_i\| \leq r_0. \end{cases} \quad (16)$$

As the basis functions have no singularities, they can be centred on the boundary points, thus no separate choice of the source points \mathbf{p}_i is needed (Fig. 3). The solution of the Laplace equation is approximated as

$$h(\mathbf{p}) \approx \sum_{i=1}^N \hat{G}_i(\mathbf{p})c_i, \quad (17)$$

where N is the number of all boundary points and c_i are the coefficients. The coefficients are determined from the boundary conditions. Each point with Dirichlet boundary condition gives an

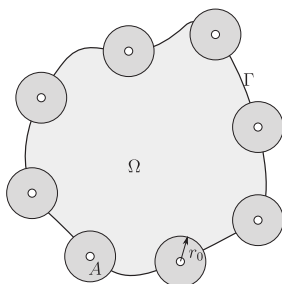


Fig. 3. Concept of BDS. Small white circles are collocation nodes with specified boundary condition, dark grey circles A are distributed sources with radius r_0 .

equation

$$\sum_{i=1}^N \hat{G}_{ij} c_i = h_j,$$

$$\hat{G}_{ij} = \hat{G}_i(\mathbf{p}_j), \quad h_j = h^D(\mathbf{p}_j), \quad \mathbf{p}_j \in \Gamma^D. \quad (18)$$

The equation that follows from each boundary point in the case of Neumann boundary conditions is

$$\sum_{i=1}^N \hat{K}_{ij} c_i = q_j, \quad q_j = q^N(\mathbf{p}_j), \quad \mathbf{p}_j \in \Gamma^N. \quad (19)$$

Typically \hat{K}_{ij} is taken to be the normal component of the gradient of G_i : $\hat{K}_{ij} = \partial \hat{G}_i(\mathbf{p}_j) / \partial \mathbf{n}(\mathbf{p}_j)$. By this definition, the diagonal terms of the matrix, corresponding to the collocation points with Neumann boundary conditions, would always equal zero. However, an indirect method is used instead [27]. First, Dirichlet boundary condition $h(\mathbf{p}_j) = 1$ is used for all the boundary points in Γ and coefficients c_i^c are obtained. As the normal component of gradient is presumably zero in the case of the solution for a constant value, the diagonal terms can be expressed as

$$\hat{K}_{ii} = -\frac{1}{c_i^c} \sum_{j=1}^N \hat{K}_{ij} c_j^c. \quad (20)$$

Both sets of equations are solved together as one matrix equation. A square system of linear equations is assembled from the rows (18) and (19) for solution of N unknown coefficients c_i .

3.2. Free parameters of the methods

In MFS, the free parameter of the method represents the distance of the artificial boundary from the geometrical boundary. In BDS, the free parameter of the method represents the radius of the desingularisation circle.

3.3. Symmetry

Consider a situation where the geometry and the fields exhibit reflection symmetry. Let us distribute the sources of the basis functions consistently with this symmetry. Respectively, for every basis function, there is another one centred on its mirror image. In the solution sum, both basis functions are multiplied by the same coefficient. The sum of such a symmetric couple of basis functions is effectively treated as a single basis function.

All the cases considered in the present paper exhibit the reflection symmetry. The coordinate system is always positioned so that the axis of symmetry lies at $x=0$. When a basis function is centred on (x_i, y_i) its mirror image is centred on $(-x_i, y_i)$. The

calculations are performed only for $x \geq 0$, on the $x < 0$ half-plane no boundary points have to be prescribed.

3.4. Treatment of moving boundary

To calculate the displacement of the moving boundary, the head gradient is needed according to Eq. (10). The equation for the head gradient has the same form as the equation given by the Neumann boundary condition. In the case of MFS, its y component is

$$\frac{\partial h}{\partial y}(\mathbf{p}_j) = \sum_{i=1}^N \frac{\partial \hat{G}_i}{\partial y}(\mathbf{p}_j) c_i, \quad (21)$$

and in the case of BDS

$$\frac{\partial h}{\partial y}(\mathbf{p}_j) = \sum_{i=1}^N F_{ij} c_i. \quad (22)$$

Here,

$$F_{ij} = \frac{\partial \hat{G}_i}{\partial y}(\mathbf{p}_j), \quad i \neq j \quad (23)$$

and

$$F_{ii} = -\frac{1}{c_i^c} \sum_{j=1}^N F_{ij} c_j^c. \quad (24)$$

The boundary points are moved together with the boundary, as follows from Eq. (10) and the backward Euler formula

$$y_j^{\text{new}} = y_j - \frac{\partial h}{\partial y}(\mathbf{p}_j) \Delta t. \quad (25)$$

y_j^{new} represents the coordinate of the boundary point in the next timestep. The derivative $\partial h / \partial y(\mathbf{p}_j)$ is calculated by Eq. (21) or Eq. (22). In MFS, the artificial boundary and the singularities are moved by the same amount, while in BDS the basis functions remain centred on the moved boundary points.

3.5. Overview of the solution procedure

The flowchart of the solution procedure is presented schematically in Fig. 4. The geometry and the boundary conditions are defined and discretised. They are represented by the coordinates of the boundary points and the boundary conditions for all the boundary points. Furthermore, the coordinates of the singularities of the basis functions in the case of MFS or the radii of the desingularisation circles in the case of BDS are chosen.

The Laplace equation (4) is solved next, using MFS or BDS. From the solution of the Laplace equation, the head derivative $\partial h / \partial y$ at the liquid surface is determined according to Eq. (21) in the case of MFS or Eq. (22) in the case of BDS. The displacement of the surface in a timestep Δt is calculated according to Eq. (25). The new shape of the liquid surface (and in the case of MFS of the artificial boundary) is determined. In particular, the new positions of the boundary points, the new boundary conditions at the boundary points and in the case of MFS the new positions of the singularities at the end of the timestep are calculated. They are used as discretised geometry and boundary conditions for the next timestep. At the same time, the total amount of liquid that enters the matrix is calculated from the displacement of the boundary points.

4. Numerical examples

To test the methods, two cases for which analytical results exist were selected. In Case 1, a steady state inflow into an

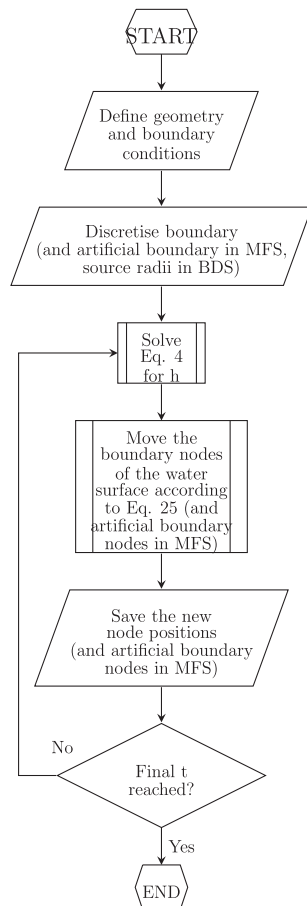


Fig. 4. Flowchart of the solution procedure.

underground tunnel is calculated. In Case 2, a simple one-dimensional problem of matrix-infilling due to a pressure change at lower boundary is calculated. The numerical results for both cases are compared with the analytical results. In Case 3, transient exchange between the conduit and the matrix in a 2D domain is calculated using MFS and BDS. Since this case is a main motivation for the study, several examples with different parameters are calculated.

The numerical procedures are written in the C++ language and compiled with the g++ 4.5.2 compiler. The matrix equations are solved using the LU method implemented in the Meschach++ library by Stephen Roberts. The OS used is Ubuntu 11.04 with Linux kernel 2.6.38-11-generic, 2.0 GiB of RAM and Intel® Core™ 2 Duo CPU E8400 with 3.00 GHz clock cycle. A calculation of a typical MFS example with $N=200$ and 1500 steps takes approximately 10 s of CPU time.

4.1. Case 1: steady inflow into a tunnel

Steady state inflow into an underground tunnel is investigated. The geometry of the problem and some parameters are presented in Fig. 5. R is the radius of the tunnel, H is the distance between its

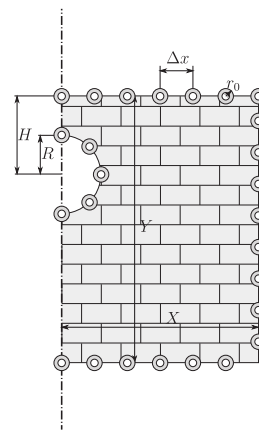


Fig. 5. Case 1: Scheme of the numerical approach for BDS. Empty circles are points with the specified boundary condition, dark grey circles are the distributed sources, and the dot-dashed line is the symmetry axis.

centre and the water level surface. The water surface is flat and horizontal. The density of the boundary points and, in the case of MFS, of the singularities of the basis functions, is constant along all the straight boundaries. Δx is the distance between the boundary points. The distance between the geometrical and the artificial boundary in the case of MFS is expressed as $s\Delta x$ (Fig. 2). X is the distance between the symmetry axis and the outer edge of the domain, and Y is the distance between the water level and the lower edge.

The first boundary point at the bottom is on the symmetry axis $x=0$, then a new point follows every Δx in the $+x$ direction until $x < X$. The boundary condition on all these points is no flow, Neumann type, $\partial h / \partial y = 0$. For every boundary point there is a singularity in MFS that is at the same x and $-s\Delta x$ away from it in y direction.

There is no boundary point at the outside lower corner, the points along $x < X$ start one Δx above the bottom, the next one is one Δx in the $+y$ direction until the water surface is reached. The boundary condition is again no flow, $\partial h / \partial x = 0$. For every boundary point there is a singularity in the MFS that is at the same y and $s\Delta x$ away from the boundary point in the $+x$ direction.

On the water surface, the points start at $x=X$ and follow until $x=0$ at the distance Δx . The boundary condition is of Dirichlet type, $h=y$. For every boundary point there is a singularity in the MFS that is at the same x and $s\Delta x$ away from the boundary point in the $+y$ direction.

The points on the conduit wall are distributed uniformly along a semicircle of radius R , the first and the last ones are at both cross-sections with $x=0$. The singularities in the MFS are distributed in the same way on a semicircle around the same centre, only with radius $R/2$. The boundary condition is of Dirichlet type, $h=y$.

The analytical solution for the case is obtained by standard methods and is given in classical textbooks [5,35] on groundwater hydrology. The inflow per unit length of tunnel is

$$q' = \frac{2\pi KH}{\log(2H/R)}, \quad (26)$$

where K is the hydraulic conductivity, R is the radius of the tunnel, and H is the depth of the centre of the tunnel below the steady water table [35]. Expressed with dimensionless variables,

the inflow is

$$q' = -2l_0k \frac{\partial V}{\partial t}, \tag{27}$$

where the numerical factor 2 comes from bilateral symmetry (there is another half of space in addition to the modelled half). Both equations together give

$$-\frac{\partial V}{\partial t} = \frac{\pi H/l_0}{\log(2H/R)}. \tag{28}$$

Both MFS and BDS are applied to test the agreement with the analytical solution. The left hand side of Eq. (28) is calculated numerically and is found to be equal to 5.888 using MFS and to 6.165 using BDS. The parameters of the calculation used are $X = 100$, $Y = 97$, $R = 1$, $H = 4$, $N = 181$, $\Delta x = 2$, in MFS $s = 5$, in BDS $r_0 = \Delta x/4$. There are 32 points in the conduit. The parameters on the right hand side in this geometry are $H/l_0 = 4$ and $R/l_0 = 1$ so the right hand side evaluates to 6.043. The agreement of our result with the textbook solution is thus very good.

4.2. Case 2: 1D time-dependent case

A 1D time-dependent case with a fixed head boundary condition on the lower end, a free surface boundary condition on the upper end, and gravity pointing downwards is investigated (Fig. 6). In 1D Darcy flow in a homogeneous medium, the gradient of h is independent of y . If the boundary condition at the lower boundary $y=0$ is $h=H$, its relation to water depth P is

$$\frac{dh}{dy} = \frac{H-P}{P}. \tag{29}$$

By Darcy's law,

$$\frac{dP}{dt} = \frac{dh}{dy}. \tag{30}$$

By eliminating the gradient of h from the equations, and integrating, we get

$$t = P_0 - P - H[\ln(H-P) - \ln(H-P_0)], \tag{31}$$

where $P_0 = P(t=0)$.

The case is solved numerically using BDS. The discretised geometry, presented in Fig. 7, is similar to Case 1, only without a conduit, and the node at $x=X$ on the water surface is left out.

The boundary conditions at the bottom boundary points are of Dirichlet type, $h=H$. For the outward boundary, the boundary

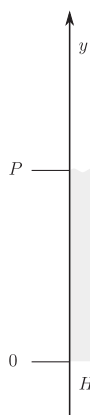


Fig. 6. Case 2: The geometry of the 1D time-dependent test case.

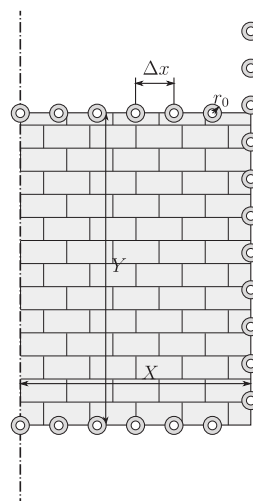


Fig. 7. Case 2: Scheme of the numerical approach for BDS. Empty circles are points with the specified boundary condition, dark grey circles are the distributed sources, and the dot-dashed line is the symmetry axis. Note that some of the nodes at $x=X$ are initially located above the water table.

condition is no flow, the same as in Case 1. The upper boundary is a free surface. The boundary condition for the Laplace equation is of Dirichlet type, $h=y$, where y is the vertical coordinate of the boundary point at a particular instant.

The parameters used are $X=101$, $Y=10$, $\Delta x = 1$, $\Delta t = 0.1$, $r_0 = \Delta x/4$, the calculation is run until $t=100$. The bottom boundary is located at $y=0$, the boundary condition is Dirichlet with $h=20$. The outward boundary extends from $y=0$ to $y=20$. That is, the boundary points are positioned at every Δx in the y direction until $y=20$, even if they are above the initial water table. The y coordinate of the central point is used as P in Eq. (31) with $P_0 = 10$ and $H=20$ and $t(P)$ is calculated. The difference between the numerically obtained t and $t(P)$ from Eq. (31) is shown in Fig. 8. The methods are compared in this way because Eq. (31) offers an explicit form for $t(P)$ and not for $P(t)$. The duration of the calculation is sufficient to approach equilibrium, the change of P during the calculation is 99.6% of the way toward $P=H$. It can be seen that the agreement is good.

4.3. Case 3: conduit–matrix exchange

The geometry of the problem and some parameters are depicted in Fig. 9. R is the radius of the conduit, H is the distance between the centre of the conduit and the water level surface at the beginning. Initially, the water surface is flat and horizontal. The density of the boundary points and, in the case of MFS, of the singularities of the basis functions, is constant along all the straight boundaries. Δx is the distance between the boundary points. The distance between the geometrical and the artificial boundary is fixed during time. The ratio between this distance and Δx is labelled s . X is the distance between the symmetry axis and the outer edge of the domain, and Y is the distance between the initial water level and the lower edge.

Discretisation is exactly the same as in Case 1. The boundary conditions at the bottom and at the outer edge are also the same as in Case 1. At the water surface, the free surface boundary condition is used. The boundary condition for the Laplace equation is of Dirichlet type, $h=y$, where y is the vertical coordinate of the boundary point at the particular instant. In MFS, the

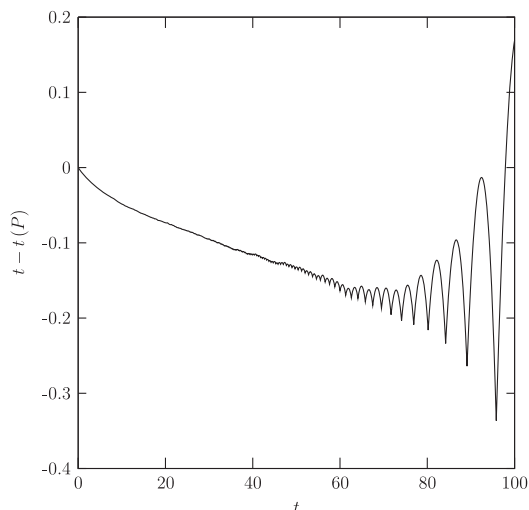


Fig. 8. Case 2: Difference between t of the BDS calculation and $t(P)$ calculated from the BDS result for P using Eq. (31). The difference stays below 1% of t in the whole calculation.

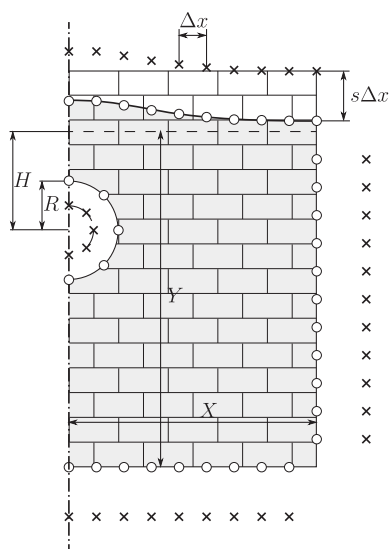


Fig. 9. Case 3: Scheme of the numerical approach for MFS. Circles are points with the specified boundary condition, crosses are poles of basis functions lying on the artificial boundary, and the dot-dashed line is the symmetry axis.

singularities above the free surface keep constant x and move in y direction to keep the distance from their boundary points equal to $s\Delta x$. The boundary condition at the conduit wall is of Dirichlet type, $h = H + \Delta h$.

An example of the MFS solution of the Laplace equation is presented in Fig. 10. The parameters of this example are $X = 100, Y = 97, R = 1, H = 4, \Delta h = 2, t = 150, N = 181, \Delta x = 2, s = 5, \Delta t = 0.1$. As already defined, t is dimensionless time, Δt is the dimensionless timestep, and N is the number of all basis

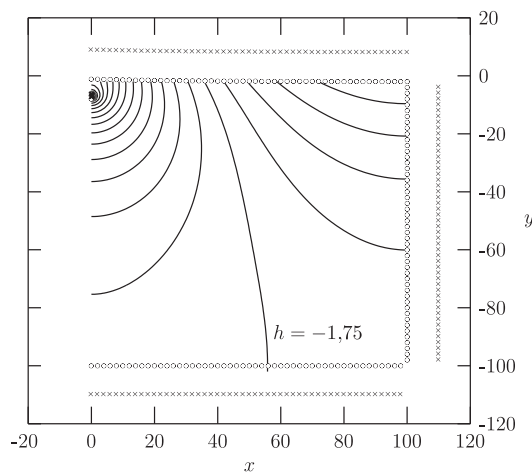


Fig. 10. Case 3: Potential h at $t=150$, calculated using MFS. The other parameters are $X = 100, Y = 97, R = 1, H = 4, \Delta h = 2, N = 181, \Delta x = 2, s = 5, \Delta t = 0.1$. The lines represent constant h and are spaced 0.05 apart. The boundary points are denoted by circles and the crosses mark the poles of the fundamental solutions.

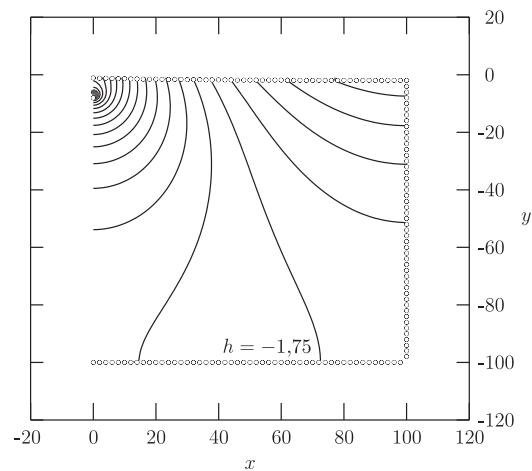


Fig. 11. Case 3: Potential h at $t=150$, calculated using BDS. The other parameters are $X = 100, Y = 97, R = 1, H = 4, \Delta h = 2, N = 181, \Delta x = 2, \Delta t = 0.1, r_0 = \Delta x/4$. The lines represent constant h and are spaced 0.05 apart. The boundary points are denoted by circles.

functions. Note that, due to the nature of the Laplace equation, there is no initial condition, its role is taken by the initial geometry and boundary conditions. The example is calculated with 32 boundary points in the conduit so that s in the conduit is approximately the same as along the straight edges. This example is taken as the MFS standard example. The resulting hydraulic head is quite uniform around the boundaries far from the conduit, while near the conduit it rises to the prescribed $h = -1$.

An example calculated using BDS with $r_0 = \Delta x/4$ and with all the parameters the same as for Fig. 10 is presented in Fig. 11. This is taken as the BDS standard example. As the gradient of h is low in some areas, comparison of equipotential lines is a sensitive method for checking the similarity of potentials calculated with

different methods. It can be seen that some equipotential lines are noticeably different even if the potentials are quite similar.

Fig. 12 represents temporal evolution of the water table. Note that the graph is cropped in the Y direction so that only the interesting part is seen. All the parameters except for t are the same as in the standard example (see Fig. 10).

The area between the original water table and the water table at time t was calculated and labelled V . It represents the volume of water that left the conduit under the assumptions of Darcy flow. The result for $V(t)$ for the standard example is presented in Fig. 13. Note that in the limit $t \rightarrow \infty$, the volume approaches $\Delta h X$, as expected.

4.3.1. Sensitivity analysis

The behaviour of the MFS and BDS in calculating Case 3 is investigated. MFS is checked first, as it is the more established of the two methods. BDS results are then compared to MFS results. A thorough sensitivity study of BDS is performed afterwards.

The correct result depends only on the physical parameters ($X, Y, R, H, \Delta h$) so the numerical result should not strongly depend on the chosen internal parameters of the MFS ($N, \Delta x, s, \Delta t$). In Fig. 14, the results for different values of s near $s=5$ are presented. It can be seen that the influence of s is small in the range considered.

The distribution and the number of boundary points is also varied. The result for the standard example, $X=100, Y=97, R=1, H=4, \Delta h=2, t=150, N=181, \Delta x=2, s=5, \Delta t=0.1$, is $V=123.253$. If the number of points in the conduit is reduced to 3 so that Δx in the conduit is comparable to Δx at the straight edges, the result is very similar, $V=123.013$. Here, $N=152$, while the other parameters remain the same. On the other hand, if the conduit is left with 32 points and Δx is enlarged to 4, then $N=107$ and $V=123.173$.

If the timestep is enlarged to $\Delta t=1$ and the other parameters are left the same as in the standard example, the result is $V=123.497$.

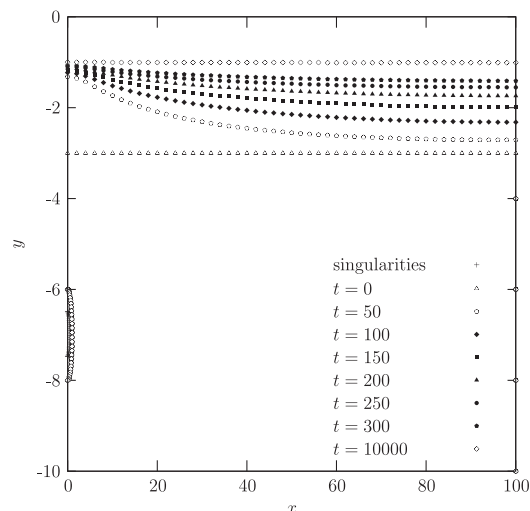


Fig. 12. Case 3: The shape of Ω at different t calculated using MFS. Ω is delimited by boundary points. The singularities are outside Ω and fall outside the graph except in the conduit along the left edge (the circular conduit is not circular in the figure due to different x and y scaling). The parameters are $X=100, Y=97, R=1, H=4, \Delta h=2, N=181, \Delta x=2, s=5, \Delta t=0.1$.

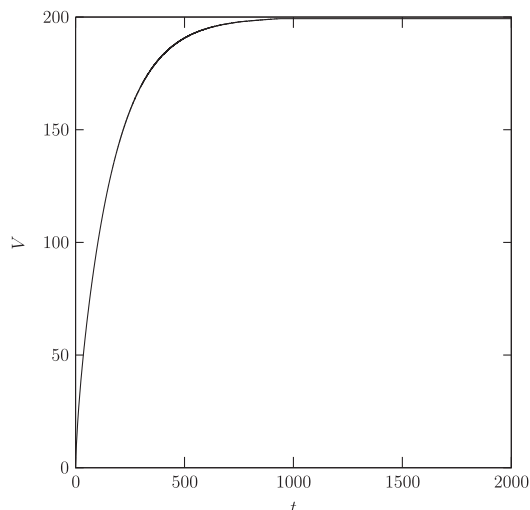


Fig. 13. Case 3: Volume as a function of time, calculated until equilibrium, using BDS. The parameters are $X=100, Y=97, R=1, H=4, \Delta h=2, N=181, \Delta x=2, \Delta t=0.1, r_0=\Delta x/4$.

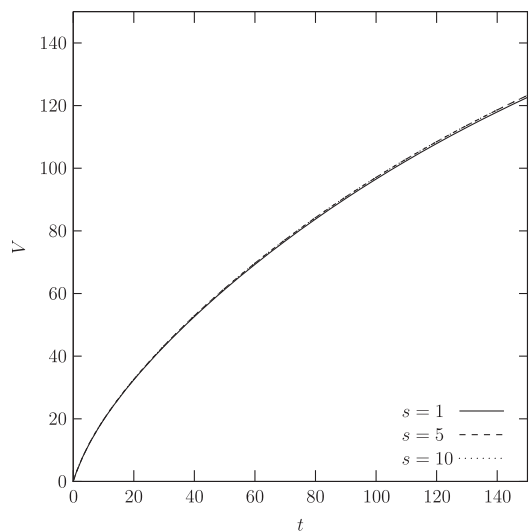


Fig. 14. Case 3: Volume as a function of time, calculated for different s in MFS. The other parameters are $X=100, Y=97, R=1, H=4, \Delta h=2, t=150, N=181, \Delta x=2, \Delta t=0.1$ as in the standard example.

In Fig. 15, the standard example is calculated by both MFS and BDS. In Fig. 16, the same is done for twice as high of a density of points along the straight edges. The agreement between MFS and BDS is better in the later case.

Sensitivity of BDS with respect to timestep Δt , source radius r_0 , and the distance between the boundary points Δx is analysed. The results for sensitivity regarding Δt are presented in Fig. 17. Calculated V at $t=150$ is more or less independent of the choice of Δt until above a critical value of Δt when it no longer converges to the correct value.

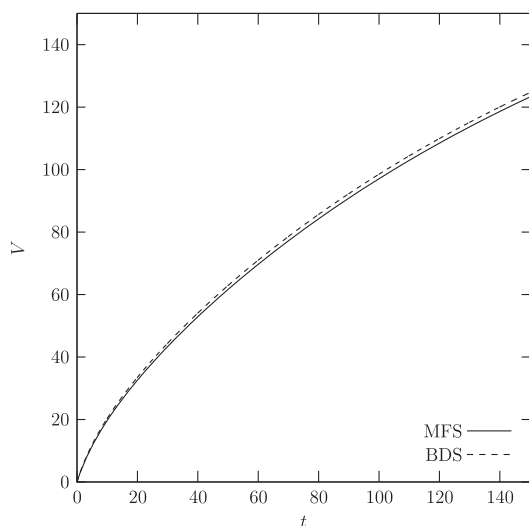


Fig. 15. Case 3: Volume as a function of time, comparison between MFS and BDS. The parameters are $X = 100, Y = 97, R = 1, H = 4, \Delta h = 2, t = 150, N = 181, \Delta x = 2, s = 5, r_0 = \Delta x/4, \Delta t = 0.1$.

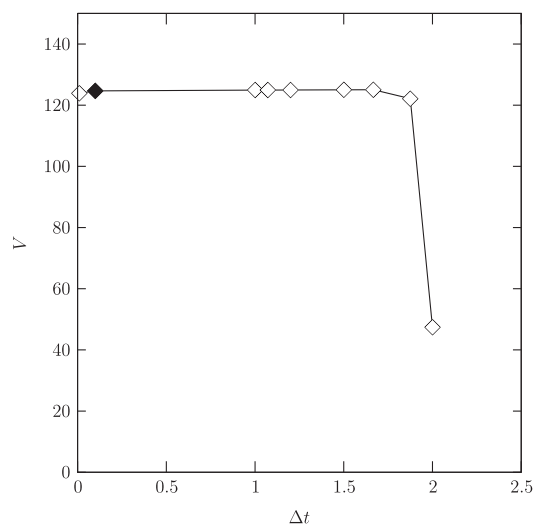


Fig. 17. Case 3: Influence of the timestep on the BDS method. The other parameters are $X = 100, Y = 97, R = 1, H = 4, \Delta h = 2, t = 150, N = 181, \Delta x = 2, r_0 = \Delta x/4$. It can be seen that the results are fairly consistent up to $\Delta t = 1.875$ while at $\Delta t = 2$ the result is obviously incorrect. The full diamond corresponds to the standard example.

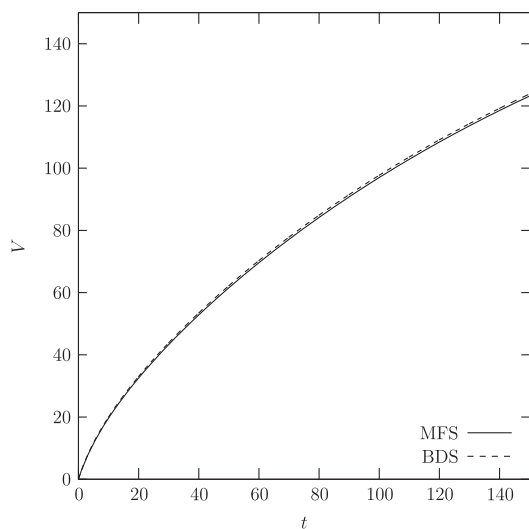


Fig. 16. Case 3: Volume as a function of time, comparison between MFS and BDS. The density of the boundary points is larger than in Fig. 15, the parameters are $X = 100, Y = 97, R = 1, H = 4, \Delta h = 2, t = 150, N = 329, \Delta x = 1, s = 5, r_0 = \Delta x/4, \Delta t = 0.1$.

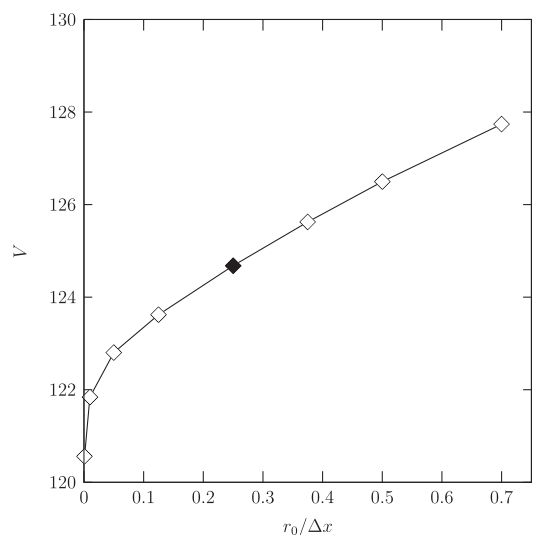


Fig. 18. Case 3: Influence of the source radius r_0 on the BDS method. The other parameters are $X = 100, Y = 97, R = 1, H = 4, \Delta h = 2, t = 150, N = 181, \Delta x = 2, \Delta t = 0.1$. When r_0 changes for a factor of 700, the change in the result is a few percent. The full diamond corresponds to the standard example.

The sensitivity to $r_0/\Delta x$ is presented in Fig. 18. The sensitivity to Δx is shown in Fig. 19. For the cases with $\Delta x \geq 2$, the number of boundary points in the conduit is 3 as the circular conduit shape cannot be resolved well enough with too few points. For smaller Δx , the number of nodes in the conduit is increased so that the distance between them is similar to Δx . In the conduit, there are 5 nodes for $\Delta x = 1$, 8 nodes for $\Delta x = 0.5$, and 14 nodes for $\Delta x = 0.25$. The analysis for $\Delta x > 8$, where the calculated V is

expected to be very different, was not performed. In these cases, the distance between the conduit and the liquid surface would fall below $1/3$ of the distance between the nodes, while the nodes in the conduit part would be less than $\Delta x/5$ apart.

We see that the results, when solving the Laplace equation by MFS, do not depend strongly on $s, \Delta x$ or Δt . The results obtained by BDS in place of MFS are also not significantly different. At the

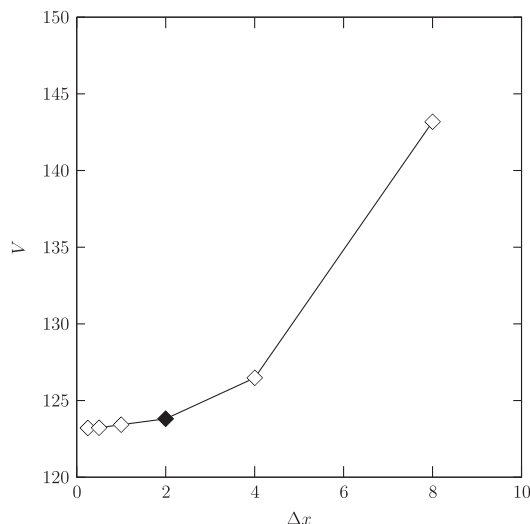


Fig. 19. Case 3: Influence of the boundary point spacing Δx on the BDS method. The other parameters are $X = 100$, $Y = 97$, $R = 1$, $H = 4$, $\Delta h = 2$, $t = 150$, $r_0 = \Delta x/4$, $\Delta t = 0.1$. The number of boundary points varies from $N = 41$ for $\Delta x = 8$ to $N = 1202$ for $\Delta x = 0.25$. The result is changing slowly as a function of Δx and is steady for $\Delta x \rightarrow 0$. The full diamond corresponds to Δx of the standard example.

same time, the BDS is not sensitive to Δt , r_0 or Δx in the range considered.

4.4. Discussion

The BDS [16] is applied in the present paper to solve moving/free boundary problems associated with the transport of water from the conduit to the porous matrix. The method essentially gives the same results as the classical MFS. It has the advantage that the artificial boundary is not present. This advantage is particularly welcome in the treated unfixed boundary problems, since the artificial boundary does not need to be recalculated along with the physical boundary, as in the classical MFS. In BDS, only the points on the unfixed physical boundary are moved.

MFS and BDS are used to calculate water exchange between a conduit and the surrounding matrix, which is a situation important in karst hydrogeology.

We consider a water filled conduit that is initially in equilibrium with the surrounding matrix. A step change in hydraulic head is applied and time-dependent exchange flow is calculated. The results obtained by MFS and BDS are compared to each other. Sensitivity analyses of the influence of the density of points, the distance between the real and the artificial boundary in MFS, the source radii in BDS, and the timestep are done. MFS is benchmarked against a textbook solution, and BDS against a time-dependent example with an analytical solution. The textbook solution is for steady state inflow into an underground tunnel. The only difference between our conduit and the tunnel is the boundary condition on the tunnel wall, where seepage face $h=y$ is used. The time-dependent analytical example is 1D, oriented along gravity with a fixed head boundary condition on the lower end and a free surface on the upper end. It is compared to a modelled 2D rectangle with a fixed head boundary condition at the lower and a free surface at the upper face, a no flow boundary

condition at the sideways face, and a symmetry axis just like the conduit–matrix exchange examples. The agreement with the benchmarks and between different runs is excellent in all cases.

5. Conclusion

Both the MFS and BDS are found to be efficient and reliable when applied to computation of moving boundary/free surface Darcy flow problems. Water exchange between a conduit and the surrounding matrix is dealt with successfully. The BDS method is applied to free and moving boundary problems for the first time and compared with MFS and analytical solutions for this type of problem. A new boundary meshless numerical method is applied to geohydrological problems and found to be suitable for the purpose.

It should be noted that in the BDS the governing equation is not satisfied in the parts of the domain overlapping with the circles [16]. The method can potentially be applied to multiply-connected-domain problems [36] while it is not certain if any modifications would be needed [16]. However, the problem tackled here is essentially simply-connected due to the consideration of the symmetry.

The BDS method presented in this paper is very general and it can be adapted or extended to handle many related problems, discussed in the present paper.

Acknowledgement

This work was funded by the Slovenian Research Agency (ARRS) in the framework of basic research project J2-4093: Development and application of advanced numerical methods in study of karst processes, and research programmes P2-0379 and P6-0119. The authors are grateful to Professor Matthew Covington for useful suggestions.

References

- [1] Nield D, Bejan A. Convection in porous media. 3rd ed. Berlin: Springer; 2006.
- [2] Ford DC, Williams PW. Karst hydrogeology and geomorphology. Chichester: John Wiley & Sons; 2007.
- [3] Hu BX. Examining a coupled continuum pipe-flow model for groundwater flow and solute transport in a karst aquifer. *Acta Carsologica* 2010;39(2): 347–59.
- [4] Leontiev A, Huacasi W. Mathematical programming approach for unconfined seepage flow problem. *Eng Anal Boundary Elem* 2001;25:49–56.
- [5] Raghavan R, Ozkan E. A method for computing unsteady flows in porous media. Pitman research notes in mathematics series, vol. 318. Harlow: Longman Scientific and Technical; 1992.
- [6] Aitchison J. Numerical treatment of a singularity in a free boundary problem. *Proc R Soc London Ser A* 1972;330:573–80.
- [7] Barenblatt GE, Zheltov IP, Kochina IN. Basic concepts in the theory of seepage of homogeneous liquids in fissured rocks. *J Appl Math Mech* 1960;24: 1286–303.
- [8] Lacy SJ, Prevost JH. Flow through porous media: a procedure for locating the free surface. *Int J Numer Anal Methods Geomech* 1987;11:585–601.
- [9] Istok J. Groundwater modeling by the finite element method. Water resources monograph. Washington, DC: American Geophysical Union; 1989.
- [10] Šarler B. Towards a mesh-free computation of transport phenomena. *Eng Anal Boundary Elem* 2002;26:731–8.
- [11] Fasshauer GF. Meshfree approximation methods with MATLAB. River Edge, NJ, USA: World Scientific Publishing; 2007.
- [12] Šarler B. From global to local radial basis function collocation method for transport phenomena. *Comput Methods Appl Sci* 2007;5:257–82.
- [13] Atluri S, Shen S. The meshless local Petrov–Galerkin (MLPG) method. Contemporary research on emerging sciences and technology. Duluth, GA, USA: Tech Science Press; 2002.
- [14] Liu GR. Mesh free methods: moving beyond the finite element method. Boca Raton: CRC Press; 2002.
- [15] Šarler B. Solution of a two-dimensional bubble shape in potential flow by the method of fundamental solutions. *Eng Anal Boundary Elem* 2006;30: 227–35.

- [16] Liu Y. A new boundary meshfree method with distributed sources. *Eng Anal Boundary Elem* 2010;34(11):914–9.
- [17] Chen J, Hsiao C, Lee Y. Study of free-surface seepage problem using hypersingular equations. *Commun Numer Methods Eng* 2007;23:755–69.
- [18] Queen D, Oxley M, Vosika D. The boundary element method applied to moving boundary problems. *Math Comput Modelling* 1990;14:145–50.
- [19] Ahmed SG, Meshrif SA. A new numerical algorithm for 2d moving boundary problems using a boundary element method. *Comput Math Appl* 2009;58:1302–8.
- [20] Chantasiriwan S, Johansson B, Lesnic D. The method of fundamental solutions for free surface Stefan problems. *Eng Anal Boundary Elem* 2009;33:529–38.
- [21] Šarler B. Stefan's work on solid-liquid phase changes. *Eng Anal Boundary Elem* 1995;16:83–92.
- [22] Fairweather G, Karageorghis A. The method of fundamental solutions for elliptic boundary value problems. *Adv Comput Math* 1998;9:69–95.
- [23] Karageorghis A, Lesnic D, Marin L. A survey of applications of the MFS to inverse problems. *Inverse Probl Sci Eng* 2011;19:309–36.
- [24] Guevara-Jordan J, Rojas S. A method of fundamental solutions for modeling of porous media advective fluid flow. *Appl Numer Math* 2003;47:449–65.
- [25] Chaiyo K, Rattanadecho P, Chantasiriwan S. The method of fundamental solutions for solving free boundary saturated seepage problem. *Int Commun Heat Mass Transfer* 2011;38:249–54.
- [26] Young DL, Chen KH, Lee CW. Novel meshless method for solving the potential problems with arbitrary domain. *J Comput Phys* 2005;209:290–321.
- [27] Šarler B. Solution of potential flow problems by the modified method of fundamental solutions: formulations with the single layer and the double layer fundamental solutions. *Eng Anal Boundary Elem* 2009;33:1374–82.
- [28] Darcy H. *Les Fontaines Publiques de la Ville de Dijon*. Paris: Victor Dalmont; 1856.
- [29] Kaviany M. *Principles of heat transfer in porous media*. New York: Springer-Verlag; 1995.
- [30] Lee C, Farmer I. *Fluid flow in discontinuous rocks*. London, New York: Chapman & Hall; 1993.
- [31] Bear J. *Dynamics of fluids in porous media*. Dover books on physics and chemistry. New York: Dover Publications; 1988.
- [32] Sahimi M. *Flow and transport in porous media and fractured rock*. Weinheim: VCH Verlagsgesellschaft; 1995.
- [33] Šarler B, Perko J, Gobin D, Goyeau B, Power H. Dual reciprocity boundary element method solution of natural convection in Darcy–Brinkman porous media. *Eng Anal Boundary Elem* 2004;28:23–41.
- [34] Kupradze VD, Aleksidze MA. The method of functional equations for the approximate solution of certain boundary value problems. *USSR Comput Math Math Phys* 1964;4:82–126.
- [35] Domenico P, Schwartz F. *Physical and chemical hydrogeology*. New York: Wiley; 1990.
- [36] Chen K, Kao J, Chen J, Young D, Lu M. Regularized meshless method for multiply-connected-domain laplace problems. *Eng Anal Boundary Elem* 2006;30(10):882–96.